

FILTER-BASED MODELING OF UNSTEADY TURBULENT CAVITATING FLOW
COMPUTATIONS

By

JIONGYANG WU

A DISSERTATION PRESENTED TO THE GRADUATE SCHOOL
OF THE UNIVERSITY OF FLORIDA IN PARTIAL FULFILLMENT
OF THE REQUIREMENTS FOR THE DEGREE OF
DOCTOR OF PHILOSOPHY

UNIVERSITY OF FLORIDA

2005

Copyright 2005

by

Jiongyang Wu

To my Parents; my wife, Weishu; and my son, Andy, for their love and support

ACKNOWLEDGMENTS

I would like to express my sincere thanks and appreciation to my advisor Professor Wei Shyy. His thorough guidance and support benefited me tremendously in exploring and pursuing my research interest. I thank him for his boundless patience and generous attitude, and his enduring enthusiasm in educating me both in research and personal development. I have benefited much from the collaboration with Professor Stein T. Johansen. I would like to thank Professor Renwei Mei for providing some helpful suggestions and serving on my committee. Additionally, I would like to thank Professors Louis N. Cattafesta, David W. Mikolaitis, and Jacob N. Chung for serving on my committee, and Dr. Siddharth Thakur for generously sharing his experience.

I have had the privilege to work with all the individuals of the Computational Thermo-Fluids group, to whom I also give my thanks.

I would like to deeply thank my parents. Their encouragement, support, trust, and love have given me power and strength through these years. My wife, Weishu Bu, has been with me and supported me all the time. My son, Andy Wu, is another source of my invaluable wealth. No words can possibly express my gratitude and love to them.

Finally, I would like to thank the NASA Constellation University Institute Program (CUIP) for financial support.

TABLE OF CONTENTS

	<u>page</u>
ACKNOWLEDGMENTS	iv
LIST OF TABLES	vii
LIST OF FIGURES	viii
LIST OF SYMBOLS	xi
ABSTRACT.....	xiv
CHAPTER	
1 INTRODUCTION.....	1
1.1 Background of Cavitation.....	1
1.1.1 Cavitation Types in Fluids.....	1
1.1.2 Cavitation Inception and Parameter	2
1.2 Research Motivations and Objectives	3
1.2.1 Challenges and Motivations	3
1.2.2 Research Objectives	8
2 NAVIER-STOKES EQUATIONS AND TURBULENCE MODELS	9
2.1 Governing Equations	9
2.2 Turbulence Model.....	11
2.3 Filter-Based RANS Model	12
2.3.1 Literature Review	14
2.3.2 Filter-Based Model Concept (FBM)	16
2.3.3 Modeling Implementation	17
2.4 Assessing FBM in Time-Dependent Single-Phase Flow.....	18
3 CAVITATION MODELS	32
3.1 Governing Equations	32
3.2 Literature Review of Cavitation Studies.....	33
3.2.1 Cavitation Compressibility Studies	35
3.2.2 Cavitation Studies on Fluid Machinery Components and Systems.....	38
3.3 Transport Equation-based Cavitation Model (TEM).....	41

4	NUMERICAL METHODS	45
4.1	Pressure-Based Algorithm	46
4.2	Pressure Implicit Splitting of Operators (PISO) Algorithm for Unsteady Computations	47
4.3	Speed-of-Sound (SoS) Numerical Modeling	50
5	ASSESSING TIME-DEPENDENT TURBULENT CAVITATION MODELS	53
5.1	Cavitating Flow through a Hollow-Jet Valve	53
5.1.1	Steady and Unsteady Turbulent Cavitating Flows	55
5.1.2	Impact of Speed-of-sound Modeling	60
5.2	Turbulent Cavitating Flow through a Convergent-Divergent Nozzle	65
5.3	Turbulent Cavitating Flow over a Clark-Y Hydrofoil	73
6	CONCLUSIONS AND FUTURE RESEACH	92
6.1	Conclusions of Present Research	92
6.2	Future Research Directions	94
	LIST OF REFERENCES	95
	BIOGRAPHICAL SKETCH	103

LIST OF TABLES

<u>Table</u>	<u>page</u>
2-1 Summary of the hybrid RANS/LES studies.....	15
2-2 Parameters used in the computation.....	19
2-3 Comparisons of different turbulence models	24
3-1 Overview of the compressible cavitation studies.....	37
3-2 Overview of cavitation on pumps, propellers, inducers and turbine blades	40
5-1 Time-averaged liquid volume fraction v/s pressure-density correlation at multiple points inside the cavity, original IDM with SoS-1, LSM	63
5-2 Time-averaged liquid volume fraction v/s pressure-density correlation at multiple points inside the cavity, original IDM with SoS-2, LSM	63
5-3 Comparisons of Strouhal number of original and modified IDM with SoS-2A	72
5-4 Time-averaged cavity leading and trailing positions of different turbulence models, modified IDM with SoS-2A, AoA=5 degrees	78
5-5 Time-averaged cavity leading and trailing positions of different turbulence models, modified IDM with SoS-2A, AoA=8 degrees.	78
5-6 Comparison of mean C_L and C_D , LSM, Cloud cavitation $\sigma = 0.80$, AoA=8 degrees.....	91

LIST OF FIGURES

<u>Figure</u>	<u>page</u>
1-1 Different types of cavitation visualization	3
1-2 Isothermal harmonic speed-of-sound in the two-phase mixture	6
2-1 Geometry configuration of square cylinder.....	19
2-2 Streamline snap-shot on fine grid with $\Delta=0.15D$	20
2-3 Pressure behaviors at the reference point on the fine grid	21
2-4 Time-averaged U-velocity along the horizontal centerline behind the cylinder	23
2-5 Snap-shots of velocity contour. Color raster plot of axial velocities	23
2-6 Streamline snap-shots of two turbulence models on fine grid	24
2-7 Time-averaged U-velocity along y at $x/D=0.0$	26
2-8 Time-averaged velocities along y at $x/D=1.0$	26
2-9 Time-averaged u-velocity along y direction	26
2-10 Mean kinetic energy on different grids	28
2-11 Comparisons of different filter sizes on time-averaged v-velocity along y at $x/D=1.0$	29
2-12 Comparisons of different filter sizes on kinetic energy	29
2-13 Time-averaged viscosity contours of different turbulence models on fine grid.....	30
3-1 Sketch of a cavity in homogeneous flow	42
3-2 Interface vector sketch in a CV.....	43
5-1 Valve geometry	54
5-2 Computational domains and boundary conditions	55

5-3	Density contour lines of the steady state solution, original IDM with SoS-1, LSM.....	56
5-4	Middle section density contours at different time instants, original IDM with SoS-1, LSM.....	57
5-5	Time evolutions at different locations, original IDM with SoS-1, LSM	58
5-6	Projected 2-D streamlines at middle plane and experimental observation	59
5-7	Middle section density contours of different SoS at different instant time, original IDM, LSM	61
5-8	Two different SoS in hollow-jet valve flow, original IDM, LSM	63
5-9	Pressure time evolutions of different SoS, original IDM, LSM.....	64
5-10	Time evolution and spectrum of pressure and density of two SoS definitions at a point at the cavitation vicinity, original IDM, LSM	64
5-11	Time-averaged eddy viscosity contours of different grids, original IDM with SoS-2, $\sigma = 1.98$	67
5-12	Time-averaged vapor volume fraction comparisons of different grids, original IDM with SoS-2, $\sigma = 1.98$	68
5-13	Time-averaged comparisons of different turbulence models on fine grid with $\Delta = 0.25L_{cav}$, original IDM with SoS-2, $\sigma = 1.98$	68
5-14	Instantaneous profiles on fine grid with $\Delta = 0.25L_{cav}$, original IDM with SoS-2, $\sigma = 1.98$	69
5-15	Pressure contours and streamlines comparison of two turbulence models on fine grid, original IDM with SoS-2, $\sigma = 1.98$	70
5-16	Pressure evolutions of original and modified IDM with SoS-2A at a reference point.....	72
5-17	Cavity shape and recirculation zone during cycling of original and modified IDM.....	72
5-18	Time-averaged volume fraction and velocity comparisons of original and modified IDM.....	73
5-19	Clark-Y geometry sketch and Grid blocks.....	76
5-20	Grid sensitivity of the time-averaged u- and v-velocity, LSM, AoA=5°	77

5-21	Time-averaged volume fraction contours and streamlines of different turbulence models, AoA=5°	78
5-22	Time-averaged volume fraction contours and streamlines of different turbulence models, AoA=8°	79
5-23	Time evolutions of cloud cavitation $\sigma = 0.55$, AoA=5°	80
5-24	Time evolutions of cloud cavitation $\sigma = 0.80$, AoA=8°	81
5-25	Cavity stage comparisons, cloud cavitation $\sigma = 0.80$, AoA=8°	83
5-26	Time-averaged u- and v-velocities of two turbulence models, AoA=5°	84
5-27	Time-averaged u- and v-velocities of two turbulence models, AoA=8°	86
5-28	Time-averaged lift and drag coefficients comparisons	88
5-29	Time-averaged viscosity contours, AoA=5°	90
5-30	Time-averaged u-velocity of different SoS treatments, cloud cavitation $\sigma = 0.80$, AoA=8°	91

LIST OF SYMBOLS

c	speed-of-sound
C	arbitrary O(1) constant
C_ρ	pressure coefficient
$C_{\varepsilon 1}, C_{\varepsilon 2}, C_\mu$	turbulence model constants
C_{dest}	empirical constant in the evaporation term
C_{prod}	empirical constant in the condensation term
k	turbulent kinetic energy
m^-	evaporation rate
m^+	condensation rate
P	pressure
q	source term
u_i	velocity components in Cartesian coordinates
u^+	non-dimensional velocity
U	magnitude of the horizontal component of velocity
t	time, mean flow time scale
T	temperature
x_i	Cartesian coordinates
y^+	non-dimensional normal distance from the wall
y_p	normal distance of the first grid point away from the wall

α	volume fraction
δ_{ij}	Kronecker delta function
ε	turbulent dissipation rate
μ	laminar viscosity
μ_t	turbulent viscosity
ξ, η, ζ	curvilinear coordinates
ϕ	generalized dependent variable
τ	Reynolds stress
τ_w	wall shear stress
ν_t	kinematic viscosity
ρ_m	mixture density
σ	cavitation parameter
$\sigma_k, \sigma_\varepsilon$	turbulence model constants

Subscripts, Superscripts

I	interface
L, l	liquid phase
V, v	vapor phase
m	mixture phase
n	normal direction
s	tangential direction
t	tangential direction
x	component in x coordinate direction

y	component in y coordinate direction
z	component in z coordinate direction
∞	free stream
*	predicted value

Abstract of Dissertation Presented to the Graduate School
of the University of Florida in Partial Fulfillment of the
Requirements for the Degree of Doctor of Philosophy

FILTER-BASED MODELING OF UNSTEADY TURBULENT CAVITATING FLOW
COMPUTATIONS

By

Jiongyang Wu

August 2005

Chair: Wei Shyy

Major Department: Mechanical and Aerospace Engineering

Cavitation plays an important role in the design and operation of fluid machinery and devices because it causes performance degradation, noise, vibration, and erosion. Cavitation involves complex phase-change dynamics, large density ratio between phases, and multiple time scales. Noticeable achievements have been made in employing homogeneous two-phase Navier-Stokes equations for cavitating computations in computational and modeling strategies. However, these issues pose challenges with respect to accuracy, stability, efficiency and robustness because of the complex unsteady interaction associated with cavitation dynamics and turbulence.

The present study focuses on developing and assessing computational modeling techniques to provide better insight into unsteady turbulent cavitation dynamics. The ensemble-averaged Navier-Stokes equations, along with a volume fraction transport equation for cavitation and turbulence closure, are employed. To ensure stability and convergence with good efficiency and accuracy, the pressure-based Pressure Implicit

Splitting of Operators (PISO) algorithm is adopted for time-dependent computations. The merits of recent transport equation-based cavitation models are first re-examined. To account for the liquid-vapor mixture compressibility, different numerical approximations of speed-of-sound are further investigated and generalized. To enhance the generality and capability of the recent interfacial dynamics-based cavitation model (IDM), we present an improved approximation for the interfacial velocity via phase transformation. In turbulence modeling, a filter-based model (FBM) derived from the $k - \varepsilon$ two-equation model, an easily deployable conditional averaging method aimed at improving unsteady simulations, is introduced.

The cavitation and turbulence models are assessed by unsteady simulations in various geometries including square cylinder, convergent-divergent nozzle, Clark-Y hydrofoil, and hollow-jet valve. The FBM reduces eddy viscosity and captures better unsteady features in single-phase flow, and yields stronger time-dependency in cavitating flows, than the original $k - \varepsilon$ model. Various cavitation models show comparable steady-state pressure distributions but exhibit substantial variations in unsteady computations. The influence of speed-of-sound treatments on the outcome of unsteady cavitating flows is documented. By assessing lift and drag coefficients, pressure and velocity distributions from inception to cloud cavitation regimes, the present approach can predict the major flow features with reasonable agreement to experimental data.

CHAPTER 1 INTRODUCTION

1.1 Background of Cavitation

In liquid flow, if the pressure drops below the vapor pressure, the liquid is unable to withstand the tensile stress and then adjusts its thermodynamic state by forming vapor-filled two-phase mixed cavities. This phenomenon is known as cavitation (Batchelor 1967). It can occur in a wide variety of fluid machinery components, such as nozzles, injectors, marine propellers and hydrofoils (Knapp et al. 1970). Cavitation is commonly associated with undesired effects, such as pressure fluctuation, noise, vibration and erosion, which can lead to performance reduction, and can damage the hydrodynamic surface. Apart from these negative effects, one known benefit of cavitation is that it can reduce friction drag (Lecoffre 1999, Wang et al. 2001). For example, in high-speed hydrofoil boats, supercavitating propellers or vehicles the gaseous cavity enveloping the external body surface can provide a shield isolated from the liquid, which helps to cut down the friction.

1.1.1 Cavitation Types in Fluids

Different kinds of cavitation can be observed depending on flow conditions, fluid properties and different geometries. Each kind of cavitation has characteristics that distinguish it from the others. Major types of cavitation are briefly described below:

- **Traveling cavitation:** Individual transient cavities or bubbles form in the liquid, expand or shrink, and then move downstream (Knapp et al. 1970). Typically, traveling cavitation is observed on hydrofoils at a small angle of attack. The number of nuclei present in the upcoming flow highly affects the geometries of the bubbles (Lecoffre 1999) (Figure 1-1A).

- Cloud cavitation: Cloud cavitation is periodically caused by vorticity shed into the flow field. It can associate with strong vibration, noise and erosion (Kawanami et al. 1997) (Figure 1-1B).
- Sheet cavitation: Sheet cavitation is a fixed, attached cavity or pocket cavitation in a quasi-steady sense (Knapp et al. 1970) (Figure 1-1C). The interface between the liquid and the vapor varies with flows.
- Supercavitation: In Supercavitation the cavity appears as the envelope of the whole solid body, and can be observed when underwater vehicles operate at very high speeds or in projectiles with a speed of 500 m/s to 1500 m/s (Kirschner 2001). A typical supercavitating hydrofoil is shown in Figure 1-1D.
- Vortex cavitation: Vortex cavities form in the cores of vortices in regions of high shear. They can occur on the tips of rotating blades, and can also appear in the separation zones of bluff bodies (Knapp et al. 1970) (Figure 1-1E).

1.1.2 Cavitation Inception and Parameter

The criterion for cavitation inception based on a static approach can be formulated as Eq. (1.1), with P as local pressure and P_v as vapor pressure

$$P < P_v \quad (1.1)$$

A parameter is needed to describe the flow condition relative to those for cavitating flows and to obtain a unique value for each set of dynamically similar cavitation conditions. In cavitation terminology σ denotes the parameter of similitude

$$\sigma = \frac{P_r - P_v}{\rho V_r^2 / 2} \quad (1.2)$$

In Eq. (1.2), P_r, V_r are the reference pressure and velocity, respectively. Usually, they take the infinity values. Unfortunately, σ is not a stringent parameter of similitude for cavitating flows. It is a necessary but not a sufficient condition. One reason is that nuclei in free stream flow can impact the two-phase flow structures (Lecoffre 1999).

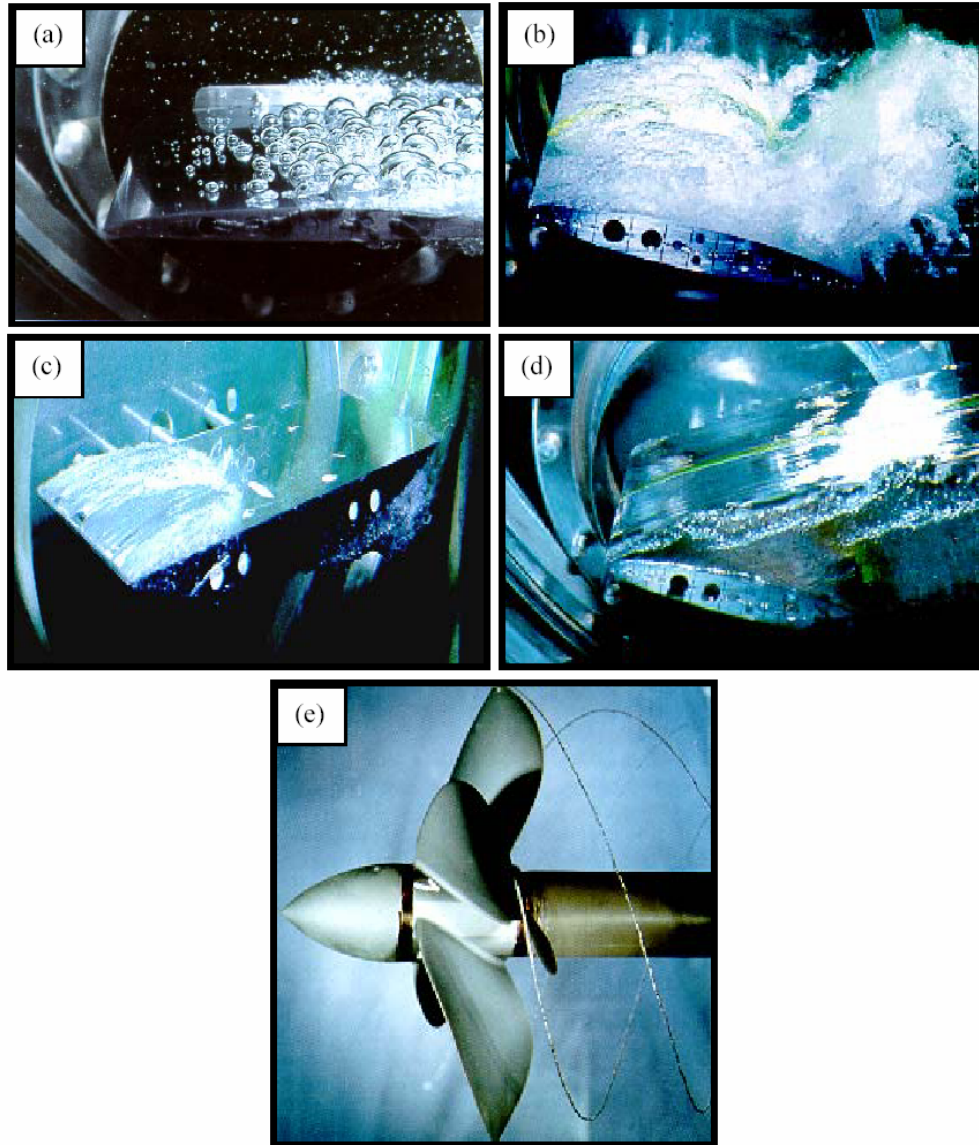


Figure 1-1. Different types of cavitation visualization (Franc et al. 1995). A) Traveling cavitation. B) Cloud cavitation. C) Sheet Cavitation. D) Supercavitation. E) Vortex cavitation

1.2 Research Motivations and Objectives

1.2.1 Challenges and Motivations

Cavitation occurs in various engineering systems, such as pumps, hydrofoils and underwater bodies. It is especially prone to occur when fluid machinery operates at off-design conditions. Cavitation may cause not only the degradation of the machine performance but flow instability, noise, vibration, and surface damage.

Phenomenologically, cavitation often involves complex interactions of turbulence and phase-change dynamics, large density variation between phases up to a ratio of 1000, multiple time scales, and pressure fluctuations. These physical mechanisms are not well understood because of the complex unsteady flow structures associated with cavitation dynamics and turbulence. There are significant computational issues regarding to accuracy, stability, efficiency and robustness of numerical algorithms for turbulent unsteady cavitating flows.

Therefore, turbulent cavitating flow computations need to address both turbulence and cavitation modeling issues. Noticeable efforts have been made in employing Navier-Stokes equations for simulations in this field. Among the various modeling approaches, the transport equation-based cavitation models (TEM) have received more interest, and both steady and unsteady flow computations have been reported (Singhal et al. 1997, Merkle et al. 1998, Kunz et al. 2000, Ahuja et al. 2001, Venkateswaran et al. 2002, Senocak and Shyy 2002a,b, 2003, 2004a,b). Senocak and Shyy (2002b, 2004a) developed an interfacial dynamics-based cavitation model (IDM) accounting for cavitation dynamics. Also, Senocak and Shyy (2002b, 2004a) and Wu et al. (2003b) assessed the merits of alternative TEM models. They showed that for steady-state computations, various cavitation models produce comparable pressure distributions. Despite the good agreement, noticeable differences have been observed in the predicted density field, especially in time-dependent computations. In IDM, an empirical factor is used to construct the interfacial velocity in time-dependent computations. Then the cavity interfacial velocity is linked to the local fluid velocity. Such an approach lacks generality because the interfacial velocity is supposed to be a function of the phase-change process.

A much closer investigation is needed to further understand differences in model performance, especially in unsteady cavitating flows.

The differences mentioned above also imply that the compressibility characteristics embodied in each cavitation model are different. This aspect can be significant in the unsteady flow computations because the speed-of-sound directly and substantially affects the cavity time-dependent features (Senocak and Shyy 2003, 2004b). Actually, the local speed-of-sound of the two-phase mixture can reduce by an order of magnitude from either value of pure liquid or vapor. It then leads to large enough Mach number variations around the cavity to make the compressibility effect substantial. The harmonic expression for speed-of-sound in an isothermal two-phase mixture (Venkateswaran et al. 2002, Ahuja et al. 2003) can be presented as

$$\frac{1}{C_m^2} = \rho_m \left(\frac{\alpha_g}{\rho_g C_g^2} + \frac{1 - \alpha_g}{\rho_l C_l^2} \right) \quad (1.3)$$

where ρ_m, ρ_g, ρ_l are mixture density, vapor density, liquid density, respectively, α_g is the vapor fraction, and C_m, C_g, C_l are speed-of-sound in mixture, in pure vapor, and in pure liquid, separately. The behavior of C_m is plotted in Figure 1-2 as a function of the vapor volume fraction. The speed-of-sound drops dramatically over a wide range of the mixture regime. Even though the bulk flow is of a very low Mach number flow, the local Mach number in the interface region may become large. Because of the lack of a dependable equation of state for the mixture sound propagation, Senocak and Shyy (2003) presented two different numerical treatments of speed-of-sound, namely SoS-1 and SoS-2, and found that they had an impact on the unsteady cavitating behavior in the convergent-divergent nozzles. They also suggested that SoS-2 was more likely to produce

the correct unsteady behaviors. This underscores that careful and accurate handling of the speed-of-sound is important. Currently, a robust compressible model for cavitating flows is still the subject of research.

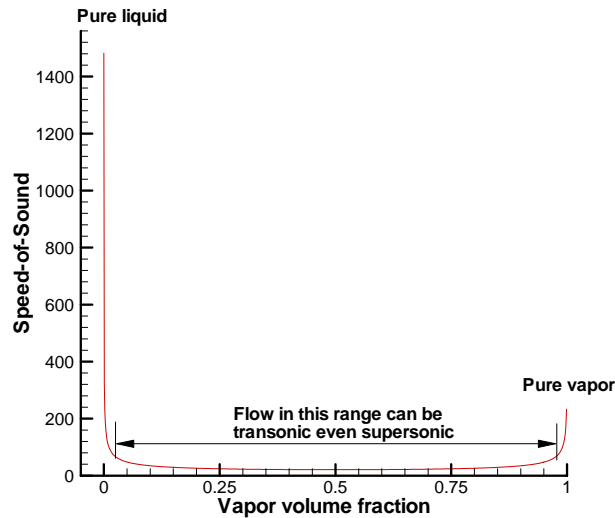


Figure 1-2. Isothermal harmonic speed-of-sound in the two-phase mixture

Besides cavitation modeling, the turbulence model can significantly influence the cavitating flow structures. Serious implications of turbulence modeling on cavitating flows were recently revealed by researchers (Senocak and Shyy 2002a, Kunz et al. 2003, Coutier-Delgosha et al. 2003, Wu et al. 2003b). They reported that high eddy viscosity of the original Launder-Spalding version of the $k - \varepsilon$ Reynolds-averaged Navier-Stokes (RANS) model (Launder and Spalding 1974) can dampen the vortex shedding motion and excessively attenuate the cavitation instabilities. Wu et al. (2003a) conducted the non-equilibrium modification, including stationary and non-stationary, in the cavitating flows over a hollow-jet valve, and observed no striking impact on the incipient cavitation. Consequently, simulation of phenomena such as periodic cavity inception and detachment requires improved modeling approaches. The Large Eddy Simulation (LES)

approach, originally proposed by Smagorinsky (1963) and refined by many researchers (Piomelli 1999, Moin 2002, Sagaut 2003) is an actively pursued route to simulate turbulent flows. However, it is fundamentally difficult to find a grid-independent LES solution unless one explicitly assigns a filter scale (Moin 2002), making the state-of-the-art immature for cavitating flow computations. On the other hand, attempts have also been made to employ the information obtained from Direct Numerical Simulations (DNS) to supplement lower order models (e.g. Sandham et al. 2001). To our knowledge, no efforts have been reported to employ LES or DNS for turbulent cavitating flows of practical interest. Recently, efforts have been made to combine the filter concept and the RANS model in single-phase (Mavridis et al. 1998, Batten and Goldberg 2002, Nichols and Nelson 2003, Nakayama 2002, Breuer et al. 2003) and, recently and even more preliminary, cavitating flow computations (Kunz et al. 2003).

Hence, it is useful to identify ways to improve the predictive capability of the updated cavitation models and the current RANS-based engineering turbulence closures, which can keep the advantages of RANS approaches and can be easily implemented in practical engineering applications with a clear physical concept. This can help better capture unsteady characters (e.g. the shedding hardly achieved in current turbulent cavitating flow simulations), and can provide better insight into the interactions between cavitation and turbulence models. This can also help establish a dependable, robust and accurate computational CFD tool to analyze and minimize the cavitation effects in the design stage of fluid machinery components or systems.

1.2.2 Research Objectives

Our goal is to develop and assess computational modeling techniques to provide better insight into unsteady turbulent cavitation dynamics, aimed at improving the handling of the above-mentioned issues in practical engineering problems.

Objective 1: Investigate alternative turbulence modeling strategies in the context of the Favre-averaged Navier-Stokes approach by doing the following:

- Develop a filter-based turbulence model (FBM) as the alternative to the original Launder-Spalding Model, both employing the $k - \varepsilon$ two-equation closure.
- Use the FBM in the cavitation simulations to provide insight into the dynamic interactions between turbulence and cavitation.

Objective 2: Enhance the cavitation model prediction capability based on the recent transport equation-based model (TEM) by doing the following:

- Further examine the merits of the recent achievements in the TEM, focusing on the interplay of the two-phase compressibility and turbulence by using correlation and spectral analysis with the direct evaluation by experimental measurements, and generalize the speed-of-sound numerical treatment.
- Adopt an improved approximation to construct the interfacial velocity by accounting for phase transformation based on the recently developed interfacial dynamics-based cavitation model (IDM).

CHAPTER 2
NAVIER-STOKES EQUATIONS AND TURBULENCE MODELS

2.1 Governing Equations

The Navier-Stokes equations in their conservative form governing a Newtonian fluid without body forces and heat transfer are presented below in the Cartesian coordinates

$$\frac{\partial \rho}{\partial t} + \frac{\partial(\rho u_j)}{\partial x_j} = 0 \quad (2.1)$$

$$\frac{\partial}{\partial t}(\rho u_i) + \frac{\partial}{\partial x_j}(\rho u_i u_j) = -\frac{\partial p}{\partial x_i} + \frac{\partial}{\partial x_j} \left[\mu \left(\frac{\partial u_i}{\partial x_j} + \frac{\partial u_j}{\partial x_i} - \frac{2}{3} \frac{\partial u_l}{\partial x_l} \delta_{ij} \right) \right] \quad (2.2)$$

The viscous stress tensor is given by

$$\tau_{ij} = \mu \left(\frac{\partial u_i}{\partial x_j} + \frac{\partial u_j}{\partial x_i} - \frac{2}{3} \frac{\partial u_l}{\partial x_l} \delta_{ij} \right) \quad (2.3)$$

In theory, direct numerical simulation (DNS) can be used to solve Equations (2.1)-(2.3) (Rogallo and Moin 1984). However, in practice the limited computing resources prevent us from pursuing such endeavors for high-Reynolds-number flows. Since we are most interested in predicting the mean properties of the turbulent flow, we can first conduct an averaging procedure to simplify the content of the equations. For time-dependent flow computations, ensemble averaging is an appropriate conceptual framework. Specifically, to avoid the additional terms involving the products of fluctuations between density and other variables in variable density flows in Reynolds

time averaging, Favre-averaging is preferred (Favre 1965) in the following form. Further details can be obtained from many references (e.g. Shyy et al. 1997, Wilcox 1998)

$$\tilde{\phi} = \frac{\overline{\rho\phi}}{\rho}; \quad \phi = \tilde{\phi} + \phi''; \quad \overline{\rho\phi''} = 0 \quad (2.4)$$

Then the Favre-averaged N-S equations become

$$\frac{\partial \bar{\rho}}{\partial t} + \nabla \cdot (\bar{\rho} \tilde{u}_j) = 0 \quad (2.5)$$

$$\frac{\partial \bar{\rho}}{\partial t} + \nabla \cdot (\bar{\rho} \tilde{u}_i \tilde{u}_j) = -\nabla \bar{P} + \nabla \cdot (\bar{\tau}_{ij} - \overline{\rho u_i'' u_j''}) \quad (2.6)$$

$$\bar{\tau}_{ij} = \mu \left(\frac{\partial \tilde{u}_i}{\partial x_j} + \frac{\partial \tilde{u}_j}{\partial x_i} - \frac{2}{3} \frac{\partial \tilde{u}_k}{\partial x_k} \delta_{ij} \right) + \mu \left(\frac{\partial \bar{u}_i''}{\partial x_j} + \frac{\partial \bar{u}_j''}{\partial x_i} - \frac{2}{3} \frac{\partial \bar{u}_k''}{\partial x_k} \delta_{ij} \right) \quad (2.7)$$

Note that the viscosity fluctuation is neglected. The nonlinear terms ($-\overline{\rho u_i'' u_j''}$), namely the Reynolds stresses, need additional modeling. The Boussinesq's eddy-viscosity hypothesis for turbulence closure leads to the following form

$$\bar{\tau}_{ij}^R = -\overline{\rho u_i'' u_j''} = \mu_t \left(\frac{\partial \tilde{u}_i}{\partial x_j} + \frac{\partial \tilde{u}_j}{\partial x_i} \right) - \frac{2}{3} \delta_{ij} \left(\mu_t \frac{\partial \tilde{u}_k}{\partial x_k} + \bar{\rho} k \right) \quad (2.8)$$

Finally, the Favre-averaged N-S equations reach the following form

$$\frac{\partial \bar{\rho}}{\partial t} + \nabla \cdot (\bar{\rho} \tilde{u}_j) = 0 \quad (2.9)$$

$$\frac{\partial \bar{\rho}}{\partial t} + \nabla \cdot (\bar{\rho} \tilde{u}_i \tilde{u}_j) = -\nabla \bar{P} + \nabla \cdot (\bar{\tau}_{ij} + \tau_{ij}^R) \quad (2.10)$$

$$\bar{\tau}_{ij} + \tau_{ij}^R = (\mu + \mu_t) \left(\frac{\partial \tilde{u}_i}{\partial x_j} + \frac{\partial \tilde{u}_j}{\partial x_i} - \frac{2}{3} \frac{\partial \tilde{u}_k}{\partial x_k} \delta_{ij} \right) \quad (2.11)$$

Compared with the original N-S equations, Favre-averaged N-S equations have the same apparent structure. The above equations can be cast in generalized curvilinear

coordinates. The procedure for the transformation of these governing equations is well established (Shyy 1994, Thakur et al. 2002).

2.2 Turbulence Model

There are several types of turbulence models. Commonly the classification can be presented as: (a) Algebraic (zero-equation) models (Baldwin and Lomax 1978); (b) One-equation models (Bradshaw et al. 1967); (c) Two-equation model, such as $k - \varepsilon$ two-equation (Launder and Spalding 1974), $k - \omega$ two-equation (Saffman 1970); (d) Second-moment closure models (Launder et al. 1975). Among the above models, the $k - \varepsilon$ turbulence model (Launder and Spalding 1974) has been popular because it is computationally tractable with deficiencies reasonably well documented (Shyy et al. 1997, Wilcox 1998). In this model, two partial differential equations accounting for the transport of turbulent kinetic energy k and for dissipation rate ε are solved. The following transport equations follow the concept of Launder and Spalding (1974) and are commonly adopted as

$$\bar{\rho}k = \frac{1}{2} \overline{\rho u_i'' u_j''}; \quad \bar{\rho}\varepsilon = \tau_{ij} \frac{\partial u_i''}{\partial x_j} \quad (2.12)$$

$$\frac{\partial(\bar{\rho}k)}{\partial t} + \frac{\partial(\bar{\rho}\tilde{u}_j k)}{\partial x_j} = P_t - \bar{\rho}\varepsilon + \frac{\partial}{\partial x_j} \left[\left(\mu + \frac{\mu_t}{\sigma_k} \right) \frac{\partial k}{\partial x_j} \right] \quad (2.13)$$

$$\frac{\partial(\bar{\rho}\varepsilon)}{\partial t} + \frac{\partial(\bar{\rho}\tilde{u}_j \varepsilon)}{\partial x_j} = C_{\varepsilon 1} \frac{\varepsilon}{k} P_t - C_{\varepsilon 2} \bar{\rho} \frac{\varepsilon^2}{k} + \frac{\partial}{\partial x_j} \left[\left(\mu + \frac{\mu_t}{\sigma_\varepsilon} \right) \frac{\partial \varepsilon}{\partial x_j} \right] \quad (2.14)$$

where σ_k and σ_ε are the turbulence model constants, $C_{\varepsilon 1}$ and $C_{\varepsilon 2}$ are the turbulence model parameters that regulate the production and destruction of dissipation of turbulence kinetic energy, respectively. The turbulent production term P_t and the turbulent viscosity are defined as

$$P_t = \tau_{ij}^R \frac{\partial \tilde{u}_i}{\partial x_j} ; \quad \mu_t = \frac{\rho C_\mu k^2}{\varepsilon} \quad (2.15)$$

Wall functions are used to address the effect of wall boundaries along with the $k - \varepsilon$ turbulence model. The empirical coefficients originally proposed by Launder and Spalding (1974), assuming local equilibrium between production and dissipation of turbulent kinetic energy, as given below

$$C_{\varepsilon 1} = 1.44, \quad C_{\varepsilon 2} = 1.92, \quad \sigma_\varepsilon = 1.3, \quad \sigma_k = 1.0 \quad (2.16)$$

In the following, we call it the Launder-Spalding model (LSM).

2.3 Filter-Based RANS Model

Turbulence plays a very important role in flow phenomena, especially since the Reynolds numbers are high in practical engineering problems. The Reynolds-averaged Navier-Stokes (RANS) and, for variable density flows, the corresponding Favre-averaged Navier-Stokes (FANS) models, such as the $k-\varepsilon$ two-equation closure, have been very popular in providing good prediction for a wide variety of flows with presently available computational resources. However, RANS models describe flows in a statistical sense typically leading to time-averaged pressure and velocity fields. Generally these approaches are not able to distinguish between quasi-periodic large-scale and turbulent chaotic small-scale features of the flow field. The representation may lose the unsteady characteristics when the flow field is governed by both phenomena, even with the help of the non-equilibrium modifications on the set of empirical constants (Wu et al. 2003a). It is clear that the statistical turbulence models have difficulties with the complex phenomena, such as flows past bluff bodies which involve separation and reattachment, unsteady vortex shedding and bimodal behaviors, high turbulence, large-scale turbulent

structures as well as curved shear layers (Frank and Rodi 1993, Rodi 1997, Shyy et al. 1997).

On the other hand, Large Eddy Simulation (LES) operates with unsteady fields of physical values. Spatial filtering is applied instead of averaging in time or ensemble, and turbulent stresses are divided into resolved and modeled parts, such as subgrid-scale models (SGS) with Smagorinsky's hypothesis (Breuer et al. 2003). Only the large energy-containing eddies are numerically resolved, accomplished by filtering out the high frequency component of the flow fields and using the low-pass-filtered form of the N-S equations to solve for the large-scale component (Kosovic 1997).

In recent years, attempts have been made to remedy the gap between RANS and LES, called the Hybrid RANS/LES methods (Nakayma and Vengadesan 2001, Breuer et al. 2003, Nelson and Nichols 2003). Various strategies have been investigated as summarized below

- Ad-hoc models (Kato and Launder 1993, Bosch and Rodi 1996,1998): using a rotation parameter to replace the original production term.
- Filter RANS/LES model (Koutmos and Mavirdis 1997): combining elements from both LES and standard eddy-viscosity approaches, by comparing the characteristic length with the mesh size—spatial filter to reconstruct the viscosity.
- Multiple Time-scale (MTS) Method (Hanjalic et al. 1980, Nichols and Nelson 2003): dividing the turbulent energy spectrum as two parts and breaking the standard k - ε equations into two sets of equations.
- Detached Eddy Simulation (DES) (Spalart 1997, Roy et al. 2003): keeping the whole boundary layer (attached eddies) to a RANS model and only the separated regions (detached eddies) to LES.

2.3.1 Literature Review

Firstly, we will review the recent studies related to the hybrid RANS/LES studies according to the above categories with a summary in Table 2-1.

Bosch and Rodi (1996) applied the ad-hoc model, which used a rotation term to reduce the turbulent production, to simulate the vortex shedding past a square cylinder near a wall. Compared with the standard turbulence model, this modification produced better unsteady behavior and obtained good agreement with the experimental data. Following their previous study, Bosch and Rodi (1998) adopted a 2-D ensemble-averaged unsteady Navier-Stokes equation, with the ad-hoc model to compute the vortex shedding past a square cylinder. The numerical results agreed well with experimental measurement and other similar numerical results. They also carried out other versions of turbulence models in the same configurations for comparisons. They concluded the present modification was better.

Rodi (1997) simulated turbulent flows over two basic bluff bodies, 2-D square cylinder and 3-D surface-mounted-cube, using different Reynolds numbers and a variety of LES and RANS methods. The various calculation results generally agreed with detailed experimental data. Assessment was given based on performance, cost and the potential of the various methods based on the comparison with the measurement.

Koutmos and Mavridis (1997) combined LES and the standard k - ϵ models to formulate the eddy-viscosity by comparing a mesh size Δ with the characteristic length in the flow field. Then the turbulent viscosity was constructed in two different ways. The calculation of unsteady separated flows of square cylinder wake and backward-facing

step re-circulating flows under low- ($Re=5000$) and high-Reynolds number ($Re=37000$) conditions agreed well with the experimental measurements.

Nagano et al. (1997) developed a low Reynolds number multiple time-scale turbulence model (MTS) which separated the turbulent energy spectrum into two parts, namely, production and transfer according to the wave-number. Then the eddy-viscosity was approximated by solving both wall and homogeneous shear flows. The test results compared well with the DNS and experimental data. They concluded for homogeneous shear flow the difference between the new model and the standard $k-\varepsilon$ model from the estimation of the characteristic time-scales, not from the discrepancy in the eddy approximation.

Nichols and Nelson (2003) employed different turbulence models, including RANS, MTS and DES to simulate several unsteady flows. Based on the comparison with experimental data, they made the assessment of different models, and suggested that the MTS hybrid RANS/LES model needed more investigations in term of grid and time-step sensitivities.

Roy et al. (2003) examined Detached Eddy Simulation (DES) and RANS turbulence modeling in incompressible flow over a square cylinder. They found that the 2-D and 3-D simulations using DES are almost identical, and the results also compared well with experimental data, while the steady-state RANS significantly over-predicted the recirculating vortex behind the cylinder.

Table 2-1. Summary of the hybrid RANS/LES studies

Author and year	Methods	Conclusions
Bosch and Rodi 1996, 1998	Ensemble-averaged N-S with ad-hoc modification in turbulence closure	Capture better unsteady shedding than RANS and agreed well with experimental data

Table 2-1. Continued

Rodi 1997	RANS with LES as turbulence closure	Generally agreed with experiment measurements and found 2-D could not resolve the 3-D effect
Koutmos and Mavridis 1997	Ensemble-averaged N-S with a spatial filtering form LES	Resolved good unsteady features in square cylinder and backward facing step under low- and high-Reynolds numbers
Nagano et al. 1997	A low-Reynolds number MTS turbulence model in homogeneous shear flow	Agreed with the DNS and experiment data
Nichols and Nelson 2003	RANS, Hybrid RANS/LES, DES	Hybrid models is better than RANS with comparable accuracy with LES
Roy et al. 2003	N-S equation with a DES turbulence closure	Compared well with experimental data

2.3.2 Filter-Based Model Concept (FBM)

In the RANS models developed for steady state flows, the turbulent length scales predicted by the model extend over a large part of the flow domain. By imposing a filter on the flow, the turbulent scales smaller than the filter will not be resolved. When the filter size is smaller than the length scales returned by the RANS models, this will allow the development of flow structures that are not dissipated by the modeled effective viscosity. The sub-filter flow may be characterized by transport equations for turbulent energy, dissipation, and Reynolds stresses. In the present example, we choose to apply the LSM (Launder and Spalding 1974) as the corresponding RANS model. The filtering operation will be controlled by the size of the imposed filter Δ and the size of the RANS length scale l_{RANS} . More detailed can be obtained from Johansen et al. (2004). The brief concept is given below. We start from the RANS length scale

$$1/l_{RANS} = C_3 \frac{\varepsilon}{k^{3/2}} \quad (2.17)$$

We may now construct filtered eddy viscosity in the following general form

$$v_t = C_\mu \sqrt{\frac{2}{3}} k \cdot l_{eff} = C_\mu \sqrt{\frac{2}{3}} k \cdot l_{RANS} f\left(C_3 \frac{\Delta \cdot \varepsilon}{k^{3/2}}\right) = v_t^{RANS} f\left(C_3 \frac{\Delta \cdot \varepsilon}{k^{3/2}}\right) \quad (2.18)$$

where l_{eff} is the turbulent length scale survived during the filtering operation. The scaling function f must impose the filter, and have limiting properties such as

$$f\left(C_3 \frac{\Delta \cdot \varepsilon}{k^{3/2}}\right) = 1 - \exp\left(-C_3 \frac{\Delta \cdot \varepsilon}{k^{3/2}}\right) \quad (2.19)$$

Here k and ε are the non-resolved turbulent energy and dissipation rate separately, corresponding to unresolved turbulent length scales l_{eff}

$$l_{eff} = \frac{k^{3/2}}{C_3 \cdot \varepsilon} \left(1 - \exp\left(-C_3 \frac{\Delta \cdot \varepsilon}{k^{3/2}}\right)\right) \quad (2.20)$$

The proposed model becomes identical to the RANS model in the extremely coarse filter. In the case of a fine filter, the turbulent length scale is controlled only by the imposed filter, and the LES type of model is obtained under this condition. The model is expected to have the following properties

- If filter size Δ is identical to cell size and grid Reynolds numbers are sufficiently small (Kolmogorov scales) the DNS model is recovered.
- If filter size becomes large, the RANS model is recovered.
- The statistical understanding of the advancement of the averaged flow during one time-step implies that the time step itself should be a part of the model.
- The filter should be almost independent to the grid in a specific computation, though it may vary with different geometries (different characteristic lengths).

2.3.3 Modeling Implementation

The $k - \varepsilon$ two-equation is adopted in similar formula as Eq.(2.13)-(2.14). In Eq.(2.15), the turbulent viscosity modeled with a filter by the scaling function of Eq.(2.19) leads to the following

$$\nu_t = 0.09 \cdot \text{Min}\left[1, c_3 \frac{\Delta \cdot \varepsilon}{k^{3/2}}\right] \cdot \frac{k^2}{\varepsilon} \quad (2.21)$$

with $C_3 \sim 1$, here we choose $C_3 = 1.0$. This choice helped to assure that in near wall nodes the scaling function $f = \text{Min}\left[1, c_3 \frac{\Delta \cdot \varepsilon}{k^{3/2}}\right]$ will always return $f = 1.0$. Then the use of standard wall functions is fully justified as the standard $k - \varepsilon$ model.

In the limit of a very large filter size Δ , the viscosity becomes $\nu_t = 0.09 \cdot k^2 / \varepsilon$ and the standard $k - \varepsilon$ model is recovered. In the limit of a filter much smaller than the turbulent scale $k^{3/2} / \varepsilon$, the viscosity model becomes

$$\nu_t = 0.09 \cdot C_3 \Delta k^{1/2} \quad (2.22)$$

Then the FBM is identical to the one-equation LES models of Schumann (1975) and Yoshizawa (1993).

2.4 Assessing FBM in Time-Dependent Single-Phase Flow

For the filter-based model (FBM), we first carry out the studies on the single-phase simulations of vortex shedding past a square cylinder, and compare with experimental measurements (Lyn and Rodi 1994, Lyn et al. 1995).

The parameters for the computations are given in Table 2-2. The square cylinder, with a height D , is located at the center of a water channel. Figure 2-1 shows the geometry of the experimental set-up of Lyn and Rodi (1994) and Lyn et al. (1995), which is selected to guide the investigation, and the non-dimensionalized coordinates. It consists of a 2D square cylinder inside a channel. To reduce numerical errors in the vicinity of the cylinder, we adopt uniform grid spacing within the $4D \times 3D$ domain surrounding the cylinder. Outside this block, the grid is slightly expanded toward the edges of the

computational domain. All variables are non-dimensionalized by the free stream velocity and the cylinder height. The fluid properties are held unchanged and the Mach number is zero. At the inlet, the mean velocity U_{in} is uniform and follows the horizontal direction. The inlet turbulent intensity is 2%. Based on the definition of the turbulent viscosity formula adopted in the LSM and by assigning the turbulent Reynolds number to be 200, we determine the inlet dissipation rate. The flow variables are extrapolated at the outlet. The wall function (Shyy et al. 1997) is employed for the solid boundary treatment.

Table 2-2. Parameters used in the computation

U_{in} (m/s)	ρ (kg/m ³)	μ (kg/m.s)	Re	D (m)	k (m ² /s ²)	ε (m ² /s ³)
0.535	1000	1.002×10^{-3}	21357	0.04	1.7174×10^{-4}	2.5×10^{-6}

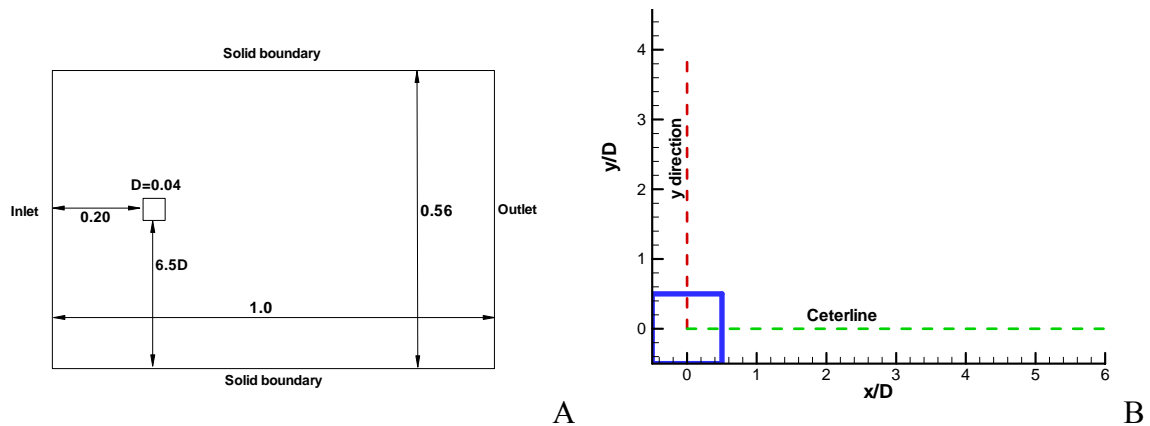


Figure 2-1. Geometry configuration of square cylinder. A) Computational domain. B) Non-dimensional coordinates

To investigate the effect of grid resolution on numerical accuracy, we used three levels of grids including fine, intermediate and coarse grids, which have 25, 20 and 10 nodes on each side of the cylinder respectively. For comparison, the Launder-Spalding model (LSM) is also carried out on coarse and fine grids. To investigate the sensitivity, we use four different filter sizes: 0.15D, 0.3D, 0.6D and 0.9D on coarse grid (10 intervals), and 0.15D, 0.25D, 0.6D and 0.9D on fine grid (25 intervals). Unless explicitly mentioned, $\Delta = 0.15D$ is used as the reference filter size.

If $(\Delta \cdot \varepsilon) / k^{3/2}$ exceeds 1.0, the filter scaling function $f = \text{Min}[1.0, (\Delta \cdot \varepsilon) / k^{3/2}]$ will take a value of 1.0. This treatment enables one to apply the wall function of LSM for the solid wall treatment, which is confirmed by the outcome presented in Figure 2-2.

A pressure reference point was located at position $x/D=0.0$ and $y/D=0.50$, which is the midpoint of the cylinder upper wall. For the fine grid we show predicted pressure development at the wall reference point in Figure 2-3A. We see a modulated and inexact periodic signal that qualitatively agrees with the experiments (Lyn and Rodi, 1994). The FBM produces pressure oscillations corresponding to amplitudes of pressure coefficient of approximately 2.5, while pressure coefficient amplitude predicted by the LSM varies from approximately 0.1 to less than 0.05. We also found that the LSM tends to be more time independent on the finer grid and the oscillations die out eventually. The FFT of the C_p by filter-based model (Figure 2-3A) shows multiple frequencies with a dominant one at around 2.15 (Figure 2-3B).

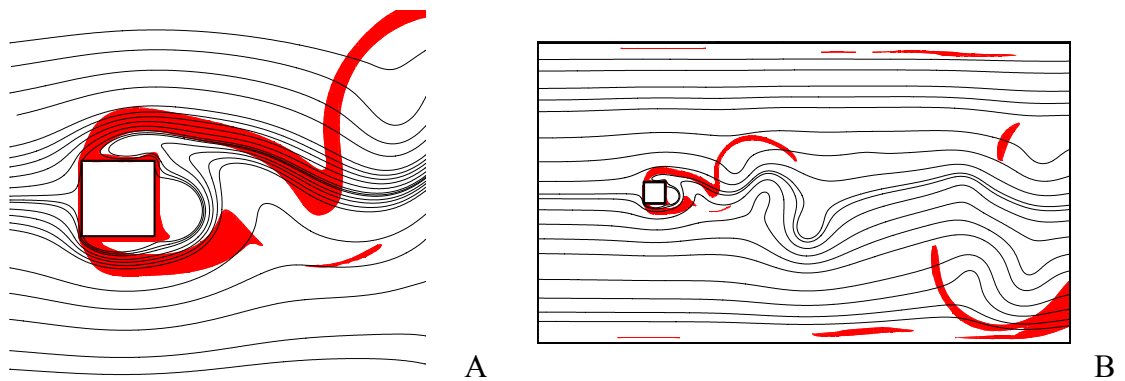


Figure 2-2. Streamline snap-shot on fine grid with $\Delta = 0.15D$. Red shadow indicates $f = \text{Min}(1.0, \frac{C_3 \cdot \Delta \cdot \varepsilon}{k^{3/2}}) = 1.0$ for recovering the LSM. At other regions the filter function is employed. A) Zoom in. B) Full view

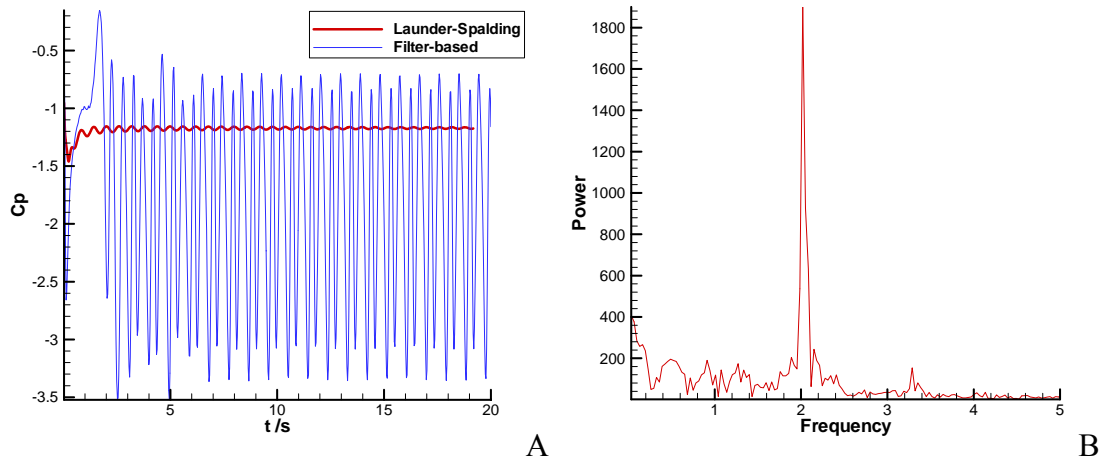


Figure 2-3. Pressure behaviors at the reference point on the fine grid. A) Pressure coefficients C_p time evolutions, LSM and FBM. B) C_p FFT, FBM

Figure 2-4 shows the time-averaged horizontal velocities along the centerline behind the cylinder. The LSM predicts too long wake lengths l_r behind the cylinder at about $3.0D$ for both grids (coarse and fine grids), which are almost identical to the numerical results by Rodi (1997). Further results of the FBM, using a constant filter size of $\Delta = 0.15D$ are shown in the same figure. For the intermediate and fine grids, the FBM results quantitatively agree with the experimental data of Lyn et al. (1995) including the asymmetric behavior. Even for the coarse grid, the size of the separation zone is well reproduced. However, the reverse velocity in the wake as well as the velocity defect in the remaining part of the wake is slightly under-predicted. In the case of the coarse grid the resolution of the shear layer at the cylinder wall is sub-critical and this affects both the onset of each shedding cycle as well as the magnitude of the vorticity in the wake. Flow structures of the solutions at a given time instant on coarse and fine grids, and with LSM and FBM are highlighted in Figure 2-5. For the FBM, as the grid resolution is refined, the vortex structure becomes more dispersed and less confined in the wake region. In contrast, for the LSM, the impact of the turbulent viscosity is dominant, and

the fine grid solution exhibits less fluctuation in time. The streamlines at one time instant for both models are presented in Figure 2-6. The LSM only catches two separated pockets at the cylinder upper and lower shoulders, and two wakes behind the cylinder. The shedding motion is almost gone. The FBM is able to capture the sharp separation in the shear layer, which agrees well with the experimental observation from Lyn and Rodi (1994) and Lyn et al. (1995).

From Table 2-3 we see that the predicted Strouhal numbers are about 20% higher than the $St=0.135$ from experiment by Lyn and Rodi (1994). By comparing the present solutions on different grids using the FBM with the same filter size, the variations of the Strouhal number are less than 4%. Hence, the only significant result is the Strouhal number being approximately 20% larger. This over-prediction may be due to the 2D effect, compared with the 3D measurement in the experiment. The large-scale structures of the flow have a three-dimensional nature and we do not expect to reproduce all features of this flow correctly in two dimensions. This will be more pressing as the filter size and grid is reduced and we depart more and more from the LSM. This seems to be consistent with the results from Yu and Kareem (1997) who needed to use a larger Smagorinsky coefficient to reproduce the Strouhal number in 2D compared to their full 3D simulations. Another interesting finding is that the LSM required much smaller time steps, compared with the FBM in order to get stable and convergent solutions using the PISO algorithm. From Table 2-3 it is seen that the time steps have to be reduced substantially in order to employ the LSM. Hence, the time consumption with the FBM is around half smaller in the present study.

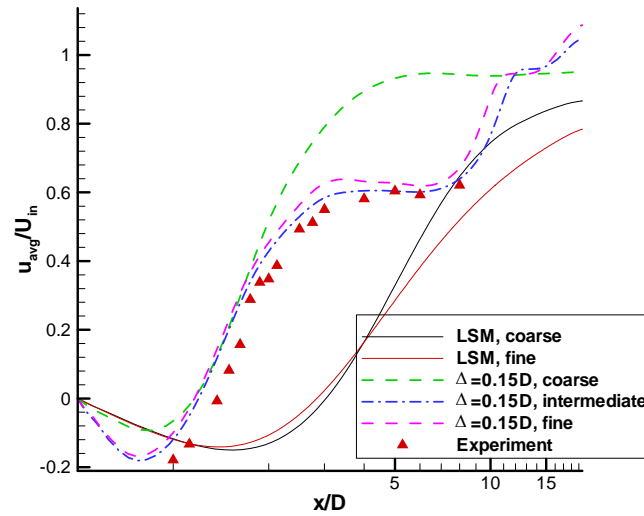


Figure 2-4. Time-averaged U-velocity along the horizontal centerline behind the cylinder. Experimental data are from Lyn and Rodi (1994) and Lyn et al. (1995)

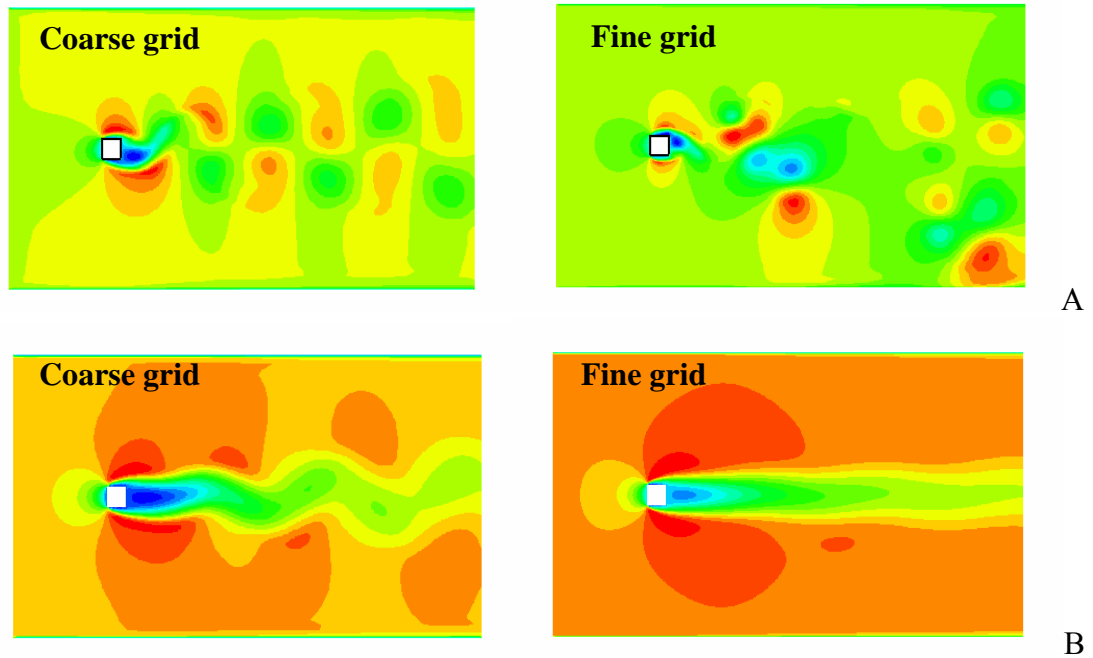


Figure 2-5. Snap-shots of velocity contour. Color raster plot of axial velocities (red is largest, blue lowest). A) FBM: coarse grid, velocity range is $-0.31 \sim 1.53$. B) FBM: fine grid, velocity range is $-0.66 \sim 1.88$. C) LSM: coarse grid, velocity range is -0.09 to 1.25 . D) LSM: fine grid, velocity range is -0.31 to 1.20

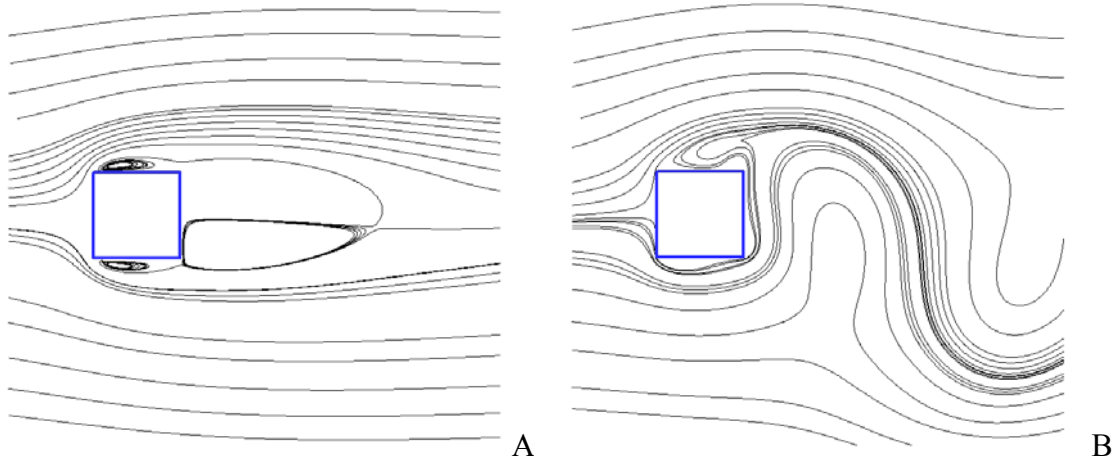


Figure 2-6. Streamline snap-shots of two turbulence models on fine grid. A) LSM. B) FBM

Table 2-3. Comparisons of different turbulence models. l_R/D is the relative position of the reattachment, measured from the cylinder center (coarse: 10 intervals, intermediate: 20 intervals, fine: 25 intervals on each cylinder face)

Model	Grid ($n_x \times n_y$)	Filter Size	Time Step $dt/(D/U_{in})$	l_R/D	St
FBM	Coarse (162×92)	0.15 D	0.0134	1.22	0.155
		0.30 D	0.0134	1.40	0.151
		0.60 D	0.0134	2.12	0.143
		0.90 D	0.0134	2.73	0.137
	Intermediate (290×190)	0.15 D	0.0134	1.25	0.163
	Fine (300×195)	0.15 D	0.0669	1.23	0.161
		0.25D	0.0669	1.25	0.148
		0.60D	0.0669	1.98	0.140
0.90D		0.0669	2.64	0.134	
LSM	Coarse (162×92)		0.00268	3.03	0.124
	Fine (300×195)		0.000803	2.80	0.125
Exp. Lyn et al. (1995)				1.38	0.135

The predicted velocity profiles are given in Figure 2-7 to Figure 2-10. One thing to be noted is that the experiments of Lyn and Rodi (1994) and Lyn et al. (1995) were recorded on a single side, assuming that the ensemble and time averaged flow was symmetrical across the axial symmetry line. As a result, data were recorded only at one side of the symmetry line. Hence, we have mirrored the data to enable the visual

comparison with the current numerical results. By close inspection of the experimental data, we find that the transversal time averaged velocity on the symmetry line is non-vanishing. This indicates that the data are not completely symmetrical.

Along the vertical centerline (Figure 2-7), we see that the LSM is unable to correctly reproduce the separation in the shear layer. The shoulders on the velocity profiles are not captured, presumably due to the high effective viscosity in the incoming flow. The FBM solution on the coarse grid is similar to the fine grid solution, but only as a result of poor resolution of the shear layer. The profiles for the FBM match the experimental data of Lyn and Rodi (1994). The time-averaged transversal velocity in the wake, one cylinder diameter behind the center of the cylinder, is shown in Figure 2-8B, where the LSM fails to capture the correct transversal velocity. For both intermediate and fine grids, the FBM again gives very good results. The time-averaged axial velocity is shown in Figure 2-8A. Here we see that the FBM solutions become more asymmetrical by grid refinement. The asymmetry in the time-averaged solutions is clearly seen from Figure 2-8 to Figure 2-9, and has been confirmed independently by calculations using a code that employs a staggered grid arrangement. The development of asymmetrical time averaged solutions seemed to be caused by the initial bias of the solution, which is path-dependent. Asymmetries in the time-averaged fields were noted by Sohankar et al. (1999). They reported that the asymmetries became more distinct as the Reynolds number increased. This is consistent with our findings. As suggested by Sohankar et al. (1999), the reason could be the two-dimensional geometry that is forced on the flow. In two dimensions wall attachment may be reinforced due to the imposed two-dimensionality. This can only be resolved by comparing full 3D computations.

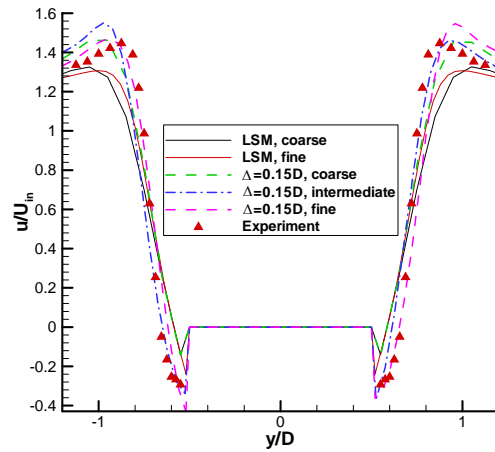


Figure 2-7. Time-averaged U-velocity along y at $x/D=0.0$. Experimental data are from Lyn and Rodi (1994) and Lyn et al. (1995)

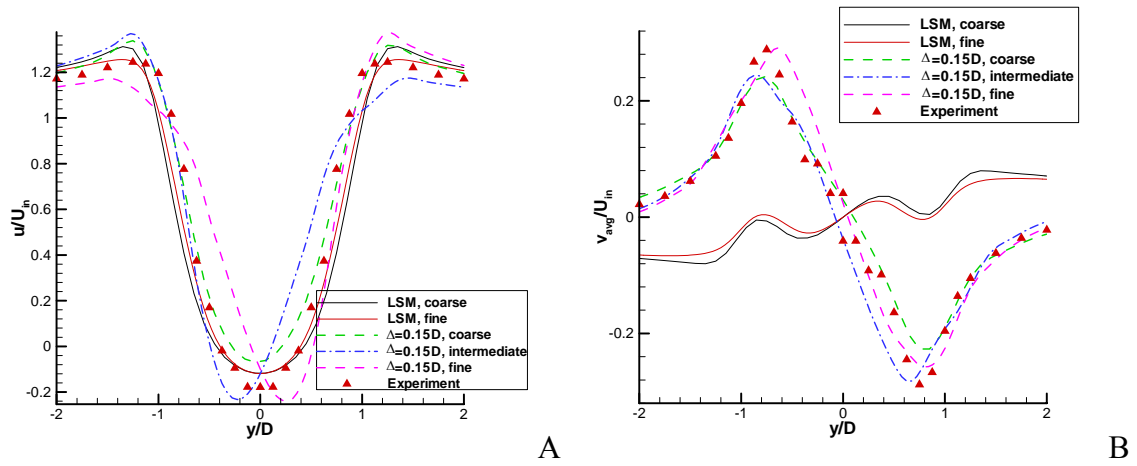


Figure 2-8. Time-averaged velocities along y at $x/D=1.0$. Experimental data are from Lyn and Rodi (1994) and Lyn et al. (1995). A) U-velocity. B) V-velocity

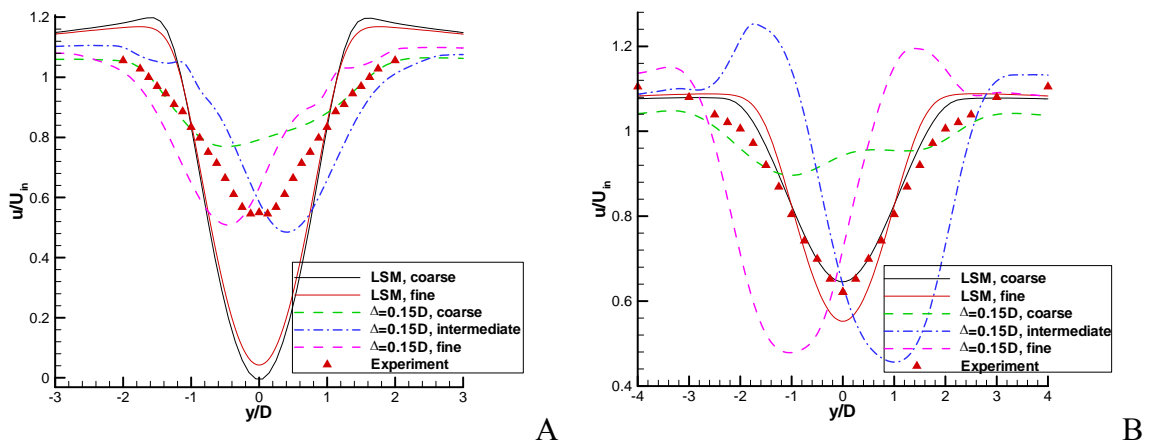


Figure 2-9. Time-averaged u -velocity along y direction. Experimental data are from Lyn and Rodi (1994) and Lyn et al. (1995). A) At $x/D=3.0$. B) At $x/D=8.0$

The predicted kinetic energies along the horizontal centerline are compared with experiments in Figure 2-10. We find that the LSM significantly under-predicts the total kinetic energy, including the periodic and turbulent parts, mainly due to poor resolution of the large scale structures in the wake. The FBM results agree well with the experiment, even in the coarse grid, in terms of the magnitude and the peak position (Figure 2-10A). The turbulent kinetic energy (the stochastic part only) is under-predicted for both LSM and FBM, as shown in Figure 2-10B. Compared with the total and turbulent kinetic energy, the turbulent part dominates for the LSM, while the periodic part is dominant for the FBM. Since the FBM over-predicts the turbulent kinetic energy, it slightly over-predicts the periodic kinetic energy at the peak.

Next, we investigate the effect of the filter size. As mentioned above, we present the results on the coarse grid with four filter sizes 0.15D, 0.3D, 0.6D and 0.9D, and fine grid with four filter size 0.15D, 0.25D, 0.6D and 0.9D. Figure 2-11 shows the transversal v-velocity of both coarse and fine grids with different filter sizes. The profiles exhibit a clear trend toward the LSM when the filter size increases. Table 2-3 further demonstrates that the computed Strouhal number and the reattachment length l_r also move toward the LSM as the filter size increase on the coarse grid. Also, the kinetic energy shows a similar trend with the various filter sizes on both coarse and fine grid (Figure 2-12). Overall, the solution with $\Delta = 0.15D$ agrees better with the experiment.

By inspection of the results it appears that the present filter-based calculations give quite regular solutions. In many calculations of the shedding from a square cylinder, perturbations of the flow are induced by "numerical noise" that may be caused by a large number of different phenomena. Examples of such phenomena are unbounded convective

fluxes, reduced numerical order caused by expanded or unstructured grids, and too large time step sizes. In the filter-based model randomness can be added to the solution by applying a random force field, similar to what is used in Renormalization-Group analyses (Smith and Woodruff, 1998). Without inducing randomness to the flow by inlet conditions or by random forcing we expect that the present model will produce regular oscillating solutions similar to URANS (unsteady RANS) calculations by Iaccarino et al. (2003).

The viscosity contours of LSM and FBM are shown in Figure 2-13. The LSM predicts a very high viscosity in the upstream of the cylinder, and the distribution is almost symmetric. The FBM significantly reduces the viscosity around 2-orders of magnitude. As discussed above, the high effective viscosity in the coming flow can damp out the unsteadiness behind the cylinder.

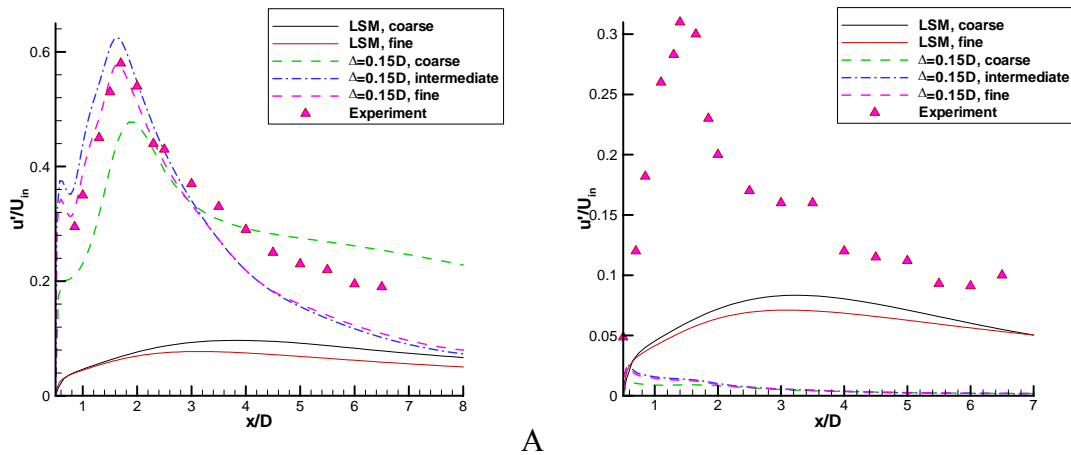


Figure 2-10. Mean kinetic energy on different grids. Experimental data are from Lyn and Rodi (1994) and Lyn et al. (1995). A) Total kinetic energy (mean + turbulent). B) Turbulent kinetic energy (stochastic)

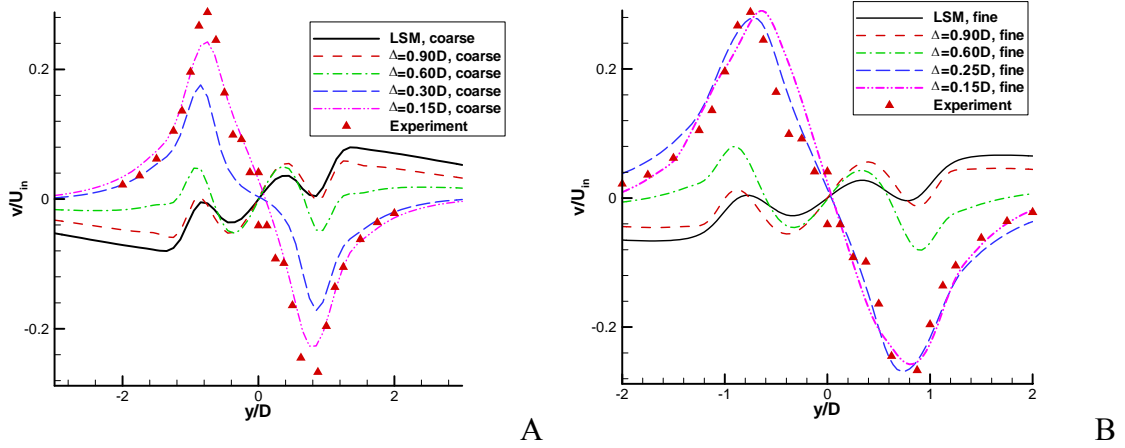


Figure 2-11. Comparisons of different filter sizes on time-averaged v -velocity along y at $x/D=1.0$. Experimental data are from Lyn and Rodi (1994) and Lyn et al. (1995). A) Coarse grid. B) Fine grid

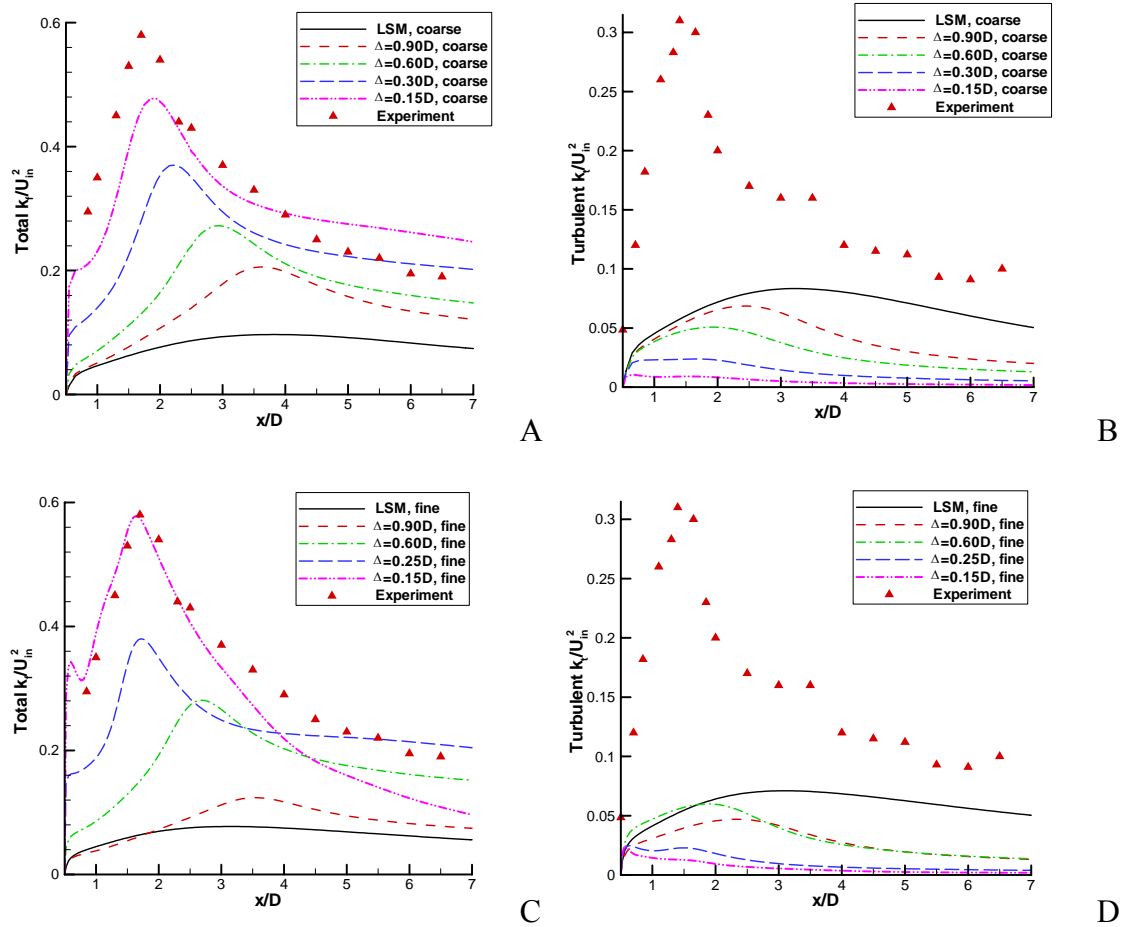


Figure 2-12. Comparisons of different filter sizes on kinetic energy. Experimental data are from Lyn and Rodi (1994) and Lyn et al. (1995). A) Coarse grid: total kinetic energy (periodic + turbulent). B) Coarse grid: turbulent kinetic energy (stochastic). C) Fine grid: total kinetic energy (periodic + turbulent). D) Fine grid: turbulent kinetic energy (stochastic)

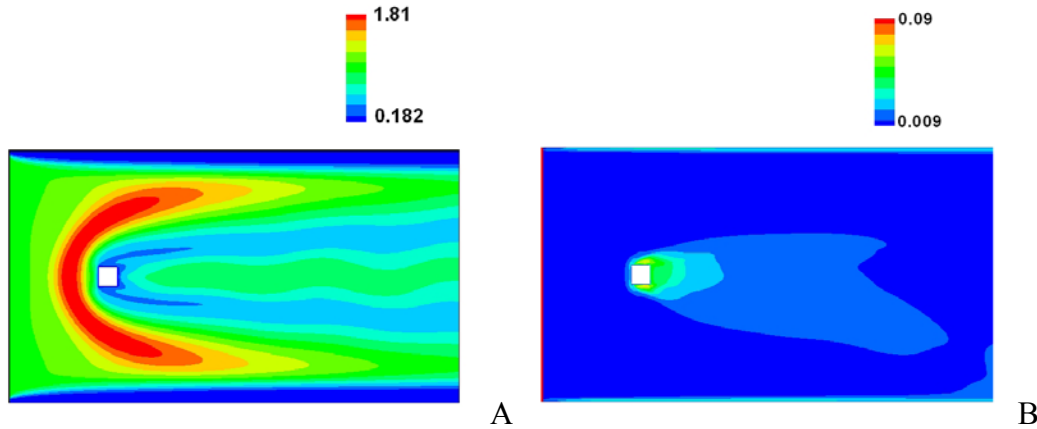


Figure 2-13. Time-averaged viscosity contours of different turbulence models on fine grid. A) LSM. B) FBM

In summary, a filtered-Navier-Stokes model, originated from the LSM, is applied to vortex shedding from a square cylinder. The introduction of the filter led to an effective viscosity that depends on both turbulent quantities and the filter size itself. The method is capable of working with standard wall-functions, allowing much coarser grids in the boundary layer compared to common LES methods. Presently the use of wall functions is justified as y^+ values for near wall nodes are greater than 20 using the fine grid (25-node). Based on the discussions above, we have the following conclusions

- Both coarse and fine grids reproduce the time averaged experimental results quantitatively. However, by refining the grid we see improved results for the velocity profiles. For the investigated filter size of $\Delta = 0.15D$, the solutions on both intermediate and fine grids are in agreement with experimental data, demonstrating that the model can produce better resolutions based on the LSM by allowing the numerical scheme to simulate the fluid physics at the scales where numerical resolutions are satisfactory.
- The increase of filter size shows that the filter-based model smoothly approaches the LSM.
- The filter-based model is shown to produce improvement over the LSM for all grids investigated.
- The Strouhal number of FBM is generally over-predicted. Further investigation is needed to investigate whether it can be resolved by full 3D simulations.

Generally, the model is expected to yield better results if full 3D solutions are performed, since the large scale 3D coherent flow structures can be resolved.

CHAPTER 3 CAVITATION MODELS

In this chapter, the single set of the governing equations for the flow field, including the continuity and momentum equations which were introduced in Chapter 2 along with a transport equation for the cavitation, is presented first. Then, the cavitation models utilized for the present study are provided, along with a review of selected recent studies. The above equations coupled with turbulence models, including Launder-Spalding model (LSM) and Filter-based model (FBM), presented in the previous chapter will complete the whole system of equations for the turbulent cavitating flow computations.

3.1 Governing Equations

The Favre-averaged Navier-Stokes equations, in their conservative form, are employed for incompressible flows. The cavitation is governed by a volume fraction transport equation. The equations are presented below in the Cartesian coordinates

$$\frac{\partial \rho_m}{\partial t} + \frac{\partial (\rho_m u_j)}{\partial x_j} = 0 \quad (3.1)$$

$$\frac{\partial (\rho_m u_i)}{\partial t} + \frac{\partial (\rho_m u_i u_j)}{\partial x_j} = -\frac{\partial p}{\partial x_i} + \frac{\partial}{\partial x_j} [(\mu + \mu_t) \left(\frac{\partial u_i}{\partial x_j} + \frac{\partial u_j}{\partial x_i} - \frac{2}{3} \frac{\partial u_k}{\partial x_k} \delta_{ij} \right)] \quad (3.2)$$

$$\frac{\partial \alpha_l}{\partial t} + \frac{\partial (\alpha_l u_j)}{\partial x_j} = (\dot{m}^+ + \dot{m}^-) \quad (3.3)$$

where ρ_m is the mixture density, u_i is the velocity component in Cartesian coordinates, t is the time, p is the pressure, α_l is volume fraction of liquid, \dot{m}^+ is the condensation rate

and \dot{m}^- is the evaporation rate, μ_t is the turbulent viscosity, and μ is the laminar viscosity of the mixture defined as

$$\mu = \mu_l \alpha_l + \mu_v (1 - \alpha_l) \quad (3.4)$$

with μ_l is the laminar viscosity of the liquid and μ_v is the viscosity of the vapor.

The mixture density and turbulent viscosity are respectively defined as below

$$\rho_m = \rho_l \alpha_l + \rho_v (1 - \alpha_l) \quad (3.5)$$

$$\mu_t = \frac{\rho_m C_\mu k^2}{\varepsilon} \quad (3.6)$$

where ρ_l is the density of the liquid and ρ_v is the density of the vapor, C_μ is the turbulence model constant and its value is 0.09 generally, k is the turbulence kinetic energy and ε is the turbulence dissipation rate. The relevant details of the different turbulence closures have been reviewed in detail in Section 2.2-2.4.

3.2 Literature Review of Cavitation Studies

Cavitation can produce negative effects in fluid machinery components and systems. Details of the existence, extent and effects of cavitation can help to minimize cavitation effects and optimize the designs. Experiments have been conducted in the past few decades for different types of fluid machinery devices and components. Ruggeri and Moor (1969) investigated methods that predicted the performance of pumps under cavitating condition. Typically, the strategy to predict the Net Positive Suction Head (NPSH) was developed. Stutz and Reboud (1997, 2000) studied the two-phase flow structure of unsteady sheet cavitation in a convergent-divergent nozzle. Wang (1999) used high-speed camera and Laser Light Sheet (LLS) to observe the cavitation in a hollow-jet valve under different openings. Wang et al (2001) studied broad cavitation

regimes of turbulent cavitating flows, covering from inception to supercavitation, over a Clark-Y hydrofoil under two different angle-of-attacks.

Besides experimentation, using CFD simulation to analyze cavitation phenomena has become convenient and popular with the development of computer hardware and software. A number of cavitation models have been developed. These studies can be put into two categories, namely interface tracking methods and homogeneous equilibrium flow models. A review of the representative studies is presented by Wang et al. (2001). Taking the advantage of homogeneous equilibrium flow theory, the mixture concept is introduced. And a unique set of mass and momentum equations along with turbulence and cavitation models is solved in the whole flow field. Within the homogeneous equilibrium flow theory, two approaches can model the cavitation dynamics. The first one is the arbitrary barotropic equation model, which suggests that the relationship between density and pressure is $\rho = f(p)$, and the second one is the transport equation-based model (TEM). Barotropic equations were proposed by Delannoy and Kueny (1990). They assumed that density was a continuous function of pressure where both pure phases were incompressible, and the phase change could be fitted by a sine curve. They could not correctly produce the unsteady behaviors in the venturi simulation. Arbitrary barotropic equation models (density is only a function of pressure) do not have the potential to capture baroclinic vorticity production because the baroclinic term of the vorticity transport equation yields zero by definition (Senocak 2002, Senocak and Shyy 2004a). In addition to agreement with the experimental study of Gopalan and Katz (2000), the above two references have demonstrated computationally that the baroclinic vorticity generation is important in the closure region. In TEM, a transport equation for

either mass or volume fraction, with appropriate source terms to regulate the mass transfer between vapor and liquid phases, is adopted. The apparent advantage of this model comes from the convective character of the equation, which allows modeling of the impact of inertial forces on cavities like elongation, detachment and drift of cavity bubbles, especially in complex 3-D interface situations (Wang et al. 2001). Different modeling concepts embodying qualitatively similar source terms with alternate numerical techniques have been proposed by various researchers (Singhal et al. 1997, Merkle et al. 1998, Kunz et al. 2000, Ahuja et al. 2001, Senocak and Shyy 2003, 2004a,b). Numerically, Singhal et al. (1997, 2002) and Senocak and Shyy (2002a,b, 2003, 2004a,b) utilized pressure-based algorithms, while Merkle et al. (1998) and Kunz et al. (2000) employed the artificial compressibility method. In addition, Vaidyanathan et al. (2003) performed a sensitivity analysis on a transport equation-based cavitation model to optimize the coefficients of its source terms. More recently, attempts have been carried out on numerical simulation of cavitating flows in turbomachines, such as pumps and inducers. Medvitz et al. (2002) utilized the pre-conditioned two-phase N-S equations to analyze the performance of cavitating flow in a centrifugal pump. Hosangadi et al. (2004) simulated the cavitating flow in the full geometry of a 3-blade Simplex inducer. Couties-Delgosha et al. (2005) presented a 3D model for cavitating flow through a 4-blade inducer adopting only one blade-to-blade passage. However, a complete robust and accurate CFD framework in this field is still a longstanding work.

3.2.1 Cavitation Compressibility Studies

Since the flow fields are rich in complexity at the cavity interface region, as pointed out in chapter 1, compressibility effect is one of the major issues in cavitation studies.

Nishiyama (1977) developed a linearized subsonic theory for supercavitating hydrofoils to clarify the compressibility correction of Mach number effect in pure water. The 2-D & 3-D steady characteristics of super-cavitating hydrofoils in subsonic flow were compared to those in incompressible flow. The essential differences, including the compressibility effect between vapor and liquid and the co-relation between cavitation and Mach number, were shown in detail.

Saurel and Cocchi (1999) focused on cavitation in the wake of a high-velocity underwater projectile. They presented a physical model based on the Euler equations in terms of two-phase mixture properties. The mathematical closure was achieved by providing state equations for the possible thermodynamic states: compressible liquid, two-phase mixture and pure vapor. The model was then solved using a hybrid computational scheme to accurately maintain the property profiles across the discontinuities. The results demonstrated a reasonable agreement compared with the known analytical solutions.

Saurel and Lemetayer (2001) proposed a compressible multiphase unconditionally hyperbolic model to deal with a wide range of application: interfaces between compressible materials, shock wave in condensed multiphase mixtures, homogeneous two-phase flows and cavitation in liquids. The model did not require a mixture equation of state and was able to provide thermodynamic variables for each phase. The results and validations with analytical solutions were provided.

Kunz et al. (2000), followed by Venkateswaran et al. (2002), developed a preconditioned time-marching algorithm for the computation of multiphase mixture flows based on carrying out perturbation expansions of the underlying time-dependent system.

The method was efficient and accurate in both incompressible and compressible flow regimes. However, it was not a fully compressible formulation for the flow fields. It could not be accurate if the bulk flows were supersonic, which indicated that compressibility should be considered even in pure liquid phase.

Senocak and Shyy (2004a,b) used the pressure-based method to simulate the cavitating flows through convergent-divergent nozzles. They presented two different treatments of speed-of-sound (SoS), including SoS-1 and SoS-2, to build up the relationship between the pressure and density for steady and unsteady cavitating flows. The comparison with the experimental data and other simulation results displayed that SoS-2 was more likely better in predicting the unsteady characteristics.

Table 3-1. Overview of the compressible cavitation studies

Author and year	Methods (Analytic/Numerical)	Conclusions (Analytic/Numerical)
Nishiyama 1977	Proposed linearized theory	linearized relationships between velocity, pressure and sound speed
Saurel and Cocchi 1999	A physical model based on the Euler equations, with state equations	Reasonable agreed with analytic solutions and could reliably deal with strong shock wave and complex EOS
Saurel and Lemetayer 2001	An unconditional hyperbolic model, with accurate treatment for non-conservative form to ensure mass conservation	Compared with analytic solutions And clouded it could deal with a wide range of application, such as shock wave, homogeneous two-phase flow and cavitation.
Kunz et al. 2000, Venkateswaran et al. 2002	A preconditioned time-marching CFD method for isothermal multiphase mixture flows, associated artificial compressibility	Agreed with experiment data under good precondition, and suggested the compressible treatment could improve the dynamics description than incompressible computations
Senocak and Shyy 2004a,b	Two numerical models for of speed-of-sound in steady and unsteady cavitating flows	Agreed well with experimental data and other numerical simulations, and demonstrated the capability in unsteady computation.

3.2.2 Cavitation Studies on Fluid Machinery Components and Systems

Ruggeri and Moor (1969) investigated similarity methods to predict the performance of pumps under cavitating condition for different temperatures, fluids and operating conditions. Typically, the strategy to predict the NPSH was developed based on two sets of available test data for each pump at the concerned range of operating conditions. Pumps performance under various flow conditions such as discharge coefficient, impellor frequency as assessed for different fluids, such as water, LH2 and butane.

Wang (1999) studied the cavitating phenomena in a hollow-jet valve under different openings and cavitation conditions, using high speed camera and LLS. Furthermore, he also studied the induced vibration mechanism, cavitation damage characteristics and ventilation effect in the valve.

Athavale and Singhal (2001) presented a homogeneous two-phase approach with a transport equation for vapor, and the reduced Rayleigh-Plesset equations for bubble dynamics based on local pressure and velocity. Compared with the experimental measurements, they obtained reasonable predictions of cavitating flows in two typical rocket turbo-pump elements: inducer and centrifugal impeller.

Lee et al. (2001a,b) analyzed the cavitation of the pump inducer sequentially. They found that the forward-swept blade demonstrated more resistance to vortex cavitation than the conventional one. They also observed that the cavity length of surface cavitation at various conditions was closely related with the cavitating number and event duration, but inconsistent with the mode predicted by linear cascade analysis in the cross-flow plane at far off-design points.

Medvitz et al. (2002) used the homogeneous two-phase RANS equations to analyze the performance of 7-blade centrifugal pumps under cavitating conditions. By using the quasi-3D analysis, the numerical results were found to be qualitatively comparable with the experimental measurements across a wide range of flow coefficients and cavitation numbers, including off-design flow, blade cavitation and breakdown.

Duttweiler and Brennen (2002) experimentally investigated a previously unrecognized instability on a cavitating propeller in a water tunnel. The cavitation on blades and in the tip vortices was explored through visual observation. The cyclic behavior of the attached blade cavities had strong similarities to that of partial cavity oscillation on single hydrofoils. Furthermore, the reduced frequency of the instability was consistent with the partial cavity instability on a single hydrofoil.

Friedrichs and Kosyna (2002) described an experimental investigation of two similar centrifugal pump impellers at low specific speed. The high-speed-film displayed rotating cavitation over a wide range of part loaded operating points, and illustrated the development of this instability mechanism, which was mainly driven by an iteration of the cavity closure region and the subsequent blades.

Hosangadi et al. (2004) numerically simulated the performance characteristics of an inducer using an N-S methodology coupled with a two-equation turbulence model. The simulations were performed at a fixed flow rate with different Net suction Specific Speeds (NSS). The numerical results showed the head loss was related to the extent of cavitation blockage. The breakdown NSS and the head loss prediction agreed well with experimental data. The insights provided a sequence of traveling and alternate cavitation phenomena in blade passages.

Coutier-Delgosha et al. (2005) presented a 3D model for a cavitating flow in 2-D venturi and in a 4-blade inducer with the comparison to experimental data and visuals. They assumed symmetry in the inducer and only considered one blade-to-blade channel in the inducer. The quasi-static results showed a consistent agreement with the experiment, but did not catch the performance breakdown.

Table 3-2. Overview of cavitation on pumps, propellers, inducers and turbine blades

Author and year	Problem study (Experimental) Methods (Numerical)	Findings(Experimental) Conclusions(Numerical)
Ruggeri and Moore 1969	Similarity to predict the pumps performance under cavitation conditions	Provide strategies to predict the pump NPSH
Wang 1999	High-speed camera and LLS in a hollow-jet valve	Cavitation, induced vibration, damage characteristics and the ventilated cavitation effect
Athavale and Singhal 2001	A homogeneous two-phase approach, with Rayleigh-Plesset equations.	Plausibly agreed the experiment, with robustness and stability in numerical convergence behaviors
Lee et al. 2001a,b	Tested the inducer performance, inlet pressure signals and event characteristics	Forward-swept blade was more resistive to vortex cavitation than the conventional one
Medvitz et al. 2002	Homogeneous two-phase RANS model	Obtained qualitative performance trends with experimental data in off-design flow, blade cavitation and breakdown
Duttweiler and Brennen 2002	Surge instability on a cavitation propeller in water tunnel	Cyclic oscillation of the attached blade cavities
Friedrichs and Kosyna 2002	High-speed camera in a centrifugal pump impeller cavitation	Rotating cavitation was mainly driven by an interaction of cavity and the leading edge of the following blades.
Hosangadi et al. 2004	N-S equations with an compressible multiphase model	Well agreed with the experimental data in terms of the head loss and breakdown NSS, and pointed out the performance loss was strongly correlated with cavitation blockage.
Coutier-Delgosha et al. 2005	3-d code FINETURBOTM, with a time-marching algorithm and low-speed preconditioner for low Mach number flows	Obtained good agreement in 2-D venturi computation, And qualitatively agreed with the experimental measurements of efficiency and cavity visuals in 3-D inducer.

3.3 Transport Equation-based Cavitation Model (TEM)

Cavitation process is governed by thermodynamics and kinetics of the phase change dynamics in the system. These issues are modeled with the aid of a transport equation with source terms regulating the evaporation and condensation of the phases. In the present study, two different cavitation models, with similar source terms for Eq.(3.3), are presented:

Heuristic model (HM). The liquid volume fraction is chosen as the dependent variable in the transport equation (Kunz et al. 2000). The evaporation term \dot{m}^- is a function of pressure whereas the condensation term \dot{m}^+ is a function of the volume fraction

$$\begin{aligned}\dot{m}^- &= \frac{C_{dest} \rho_v \alpha_l \mathbf{Min}(0, p - p_v)}{\rho_l (\rho_l U_\infty^2 / 2) t_\infty} \\ \dot{m}^+ &= \frac{C_{prod} \rho_v \alpha_l^2 (1 - \alpha_l)}{\rho_l t_\infty}\end{aligned}\quad (3.7)$$

where $C_{dest} = 9.0 \times 10^5$ and $C_{prod} = 3.0 \times 10^4$ are empirical constant values, t_∞ is the ratio of the characteristic length scale to the reference velocity scale (L/U_∞).

Interfacial dynamics-based cavitation model (IDM). The interfacial dynamics-based cavitation model (IDM) was developed by Senocak and Shyy (2004a,b). A hypothetical interface is assumed to lie in the liquid-vapor mixture region (Figure 3-1). By applying the mass and normal momentum conservation equations at the interface, and normalizing with a characteristic time scale $t_\infty = L/U$, the evaporation \dot{m}^- and condensation \dot{m}^+ are given by

$$\begin{aligned}\dot{m}^- &= \frac{\rho_l \alpha_l \mathbf{Min}(0, p - p_v)}{\rho_v (V_{v,n} - V_{I,n})^2 (\rho_l - \rho_v) t_\infty} \\ \dot{m}^+ &= \frac{(1 - \alpha_l) \mathbf{Max}(0, p - p_v)}{(V_{v,n} - V_{I,n})^2 (\rho_l - \rho_v) t_\infty}\end{aligned}\quad (3.8)$$

with vapor phase normal velocity, the interface normal, and the interfacial velocity

$$\begin{aligned}V_{v,n} &= \vec{u} \cdot \vec{n}, \quad \vec{n} = \frac{\nabla \alpha_l}{|\nabla \alpha_l|} \\ V_{I,n} &= \frac{1 - f \frac{\rho_l}{\rho_v}}{1 - \frac{\rho_l}{\rho_v}} V_{v,n}, \quad f = -0.9\end{aligned}\quad (3.9)$$

where f is found by computational satisfaction and a value of -0.9 is used. For steady state, we have $V_{I,n} = 0.0$. This approach will be called original IDM.

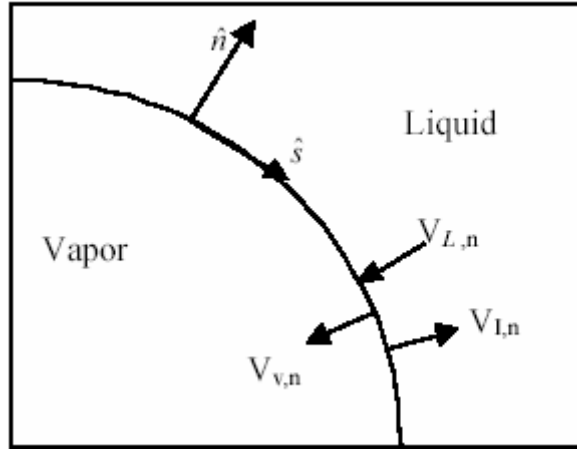


Figure 3-1. Sketch of a cavity in homogeneous flow

Regarding the above original IDM, the cavity interfacial velocity was linked to the local fluid velocity in the time-dependent computations. Such an approach lacks generality because the interfacial velocity is supposed to be a function of the phase change process. Fundamentally, the interfacial velocity can possibly be estimated more accurately based on the moving boundary computational techniques (Shyy et al. 2004).

Here, we estimate the interfacial velocity via an approximate procedure by accounting for the phase transformation process in each computational cell. By integrating Eq. (3.8) through the control volume, we have $\dot{m}^+ \cdot \Delta V$ and $\dot{m}^- \cdot \Delta V$. The net interface velocity (the interface velocity relative to the local flow field) becomes

$$V_{I,n}^{net} A = \Delta \dot{m}$$

$$V_{I,n}^{net} = \frac{\Delta \dot{m}}{A} = \frac{abs(\dot{m}^+ \Delta V) - abs(\dot{m}^- \Delta V)}{A} \quad (3.10)$$

where A is the interface area between vapor and liquid phases.

Practically, the control volume face area, $Area_{CV}$, is projected to the interface normal direction, which can be obtained by taking the gradient of the volume fraction, denoted as S , as shown in Figure 3-2 for the 2-D situation

$$\vec{n} = \frac{\nabla \alpha_L}{|\nabla \alpha_L|} = n_x \vec{i} + n_y \vec{j}$$

$$S = \frac{Area_{CV}}{\left| n_x / \sqrt{n_x^2 + n_y^2} \right|} \quad (3.11)$$

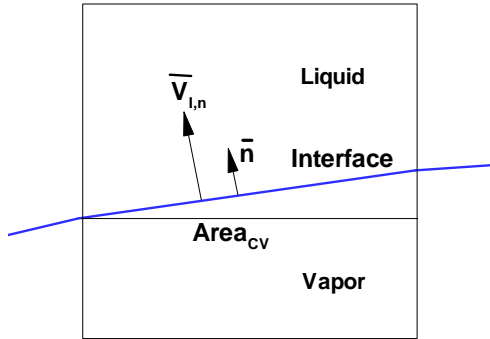


Figure 3-2. Interface vector sketch in a CV

Substituting S into Eq. (3.10) leads to

$$V_{I,n}^{net} = \frac{\Delta \dot{m}}{S} = \frac{abs(\dot{m}^+ \Delta V) - abs(\dot{m}^- \Delta V)}{S} \quad (3.12)$$

The interface velocity includes two parts: flow field local velocity $V_{I,n}^{Local} = V_{v,n}$ and net velocity $V_{I,n}^{net}$. Then we can have the following derivation

$$(V_{v,n} - V_{I,n})^2 = [V_{v,n} - (V_{I,n}^{net} + V_{I,n}^{Local})]^2 = (V_{I,n}^{net})^2 \quad (3.13)$$

Finally, the source terms assume the format, which we call modified IDM

$$\begin{aligned} \dot{m}^- &= \frac{\rho_L \alpha_L \text{Min}(0, p - p_V)}{\rho_V (V_{I,n}^{net})^2 (\rho_L - \rho_V) t_\infty} \\ \dot{m}^+ &= \frac{(1 - \alpha_L) \text{Max}(0, p - p_V)}{(V_{I,n}^{net})^2 (\rho_L - \rho_V) t_\infty} \end{aligned} \quad (3.14)$$

Recalled that for steady-state condition, we have the relationships of

$V_{I,n} = V_{I,n}^{net} + V_{I,n}^{Local} = 0$ and $V_{I,n}^{net} = -V_{I,n}^{Local} = -V_{v,n}$. In this case, the modified approach is

identical to the original IDM.

CHAPTER 4 NUMERICAL METHODS

The governing equations, presented in the previous chapters, are discretized using a finite volume approach in the present study. In this approach, the flow domain is divided into control volume cells and the governing equations are integrated over each control volume. The main advantage of the finite volume method is that the conservation laws are satisfied locally for each control volume. A non-staggered grid system is defined at the center of the cell. The decoupling of velocity-pressure can be handled by the momentum interpolation method, originally proposed by Rhie and Chow (1983). While, the original momentum interpolation had some problems, such as under-relaxation factor-dependent, time step size-dependent, and even checkerboard pressure field, which can be solved using linear interpolation of the two neighbor nodes in the cell-face velocity evaluation. A detailed review can be obtained in Yu et al. (2002).

In cavitating flow computation, the conventional computational algorithm of single-phase incompressible flow meets severe convergence and stability problems. The situation is improved by using either density-based method or pressure-based method. Both have been successful to compute turbulent cavitating flows in different configurations with comparable accuracy (Wang et al. 2001, Senocak and Shyy 2004a). However, generally the density-based method needs pre-conditioning or artificial density for flows which are largely incompressible (Merkle et al. 1998, Kunz et al. 2000, Ahuja et al. 2001). Hence we choose the pressure-based method (Shyy 1994, Senocak and Shyy 2002a). To take the advantage of non-iteration in the time-dependent computations, we

use the Pressure-Implicit Splitting Operator (PISO) algorithm other than the Semi-Implicit Method for Pressure-Linked (SIMPLE) method (Patankar 1980). The original PISO method was introduced by Issa (1985) and was modified later to be suitable for large density variation (Thakur and Wright 2002, Thakur et al. 2004). Senocak and Shyy (2002a) further extend it to cavitating flows by addressing the large density jump between phases.

4.1 Pressure-Based Algorithm

The pressure-based algorithm for steady-state computation follows the SIMPLE algorithm (Patankar 1980). The momentum equations can be discretized as

$$A_p^{\bar{u}} \bar{u}_p = \sum A_{nb}^{\bar{u}} \bar{u}_{nb} - V_p (\nabla_d P)_p + b_p^{\bar{u}} \quad (4.1)$$

where $A_p^{\bar{u}}, A_{nb}^{\bar{u}}$ are the coefficients of the cell center and neighboring nodes from convection and diffusion terms, and $V_p, b_p^{\bar{u}}$ are the cell volume and source term separately. ∇_d is the discrete form of the gradient operator. When there is no source term, the above equation turns into

$$\bar{u}_p = H(\bar{u}_{nb}) - D_p (\nabla_d P)_p \quad (4.2)$$

with

$$D_p = \begin{bmatrix} V_p / A_p^u & 0 & 0 \\ 0 & V_p / A_p^v & 0 \\ 0 & 0 & V_p / A_p^w \end{bmatrix}$$

The pressure-correction equation in the pressure-based method has been revised to achieve successful solutions for highly compressible flows (Shyy 1994, Senocak and Shyy 2002a). Generally, the mixture density at the phases interface region has high

variations. Here we will illustrate some key computational issues by focusing on the flux terms in the continuity equation, which can be decomposed as

$$\rho \bar{u} = (\rho^* + \rho')(\bar{u}^* + \bar{u}') = \rho^* \bar{u}^* + \rho^* \bar{u}' + \rho' \bar{u}^* + \rho' \bar{u}' \quad (4.3)$$

where the starred variables represent the predicted values and primed variables represent the correction terms. And it leads to

$$\rho'_p = C_\rho P' \quad (4.4)$$

$$-\nabla_d \cdot (\rho^* \mathbf{D} \nabla_d P') + \nabla_d \cdot (C_\rho \bar{u}^* P') = -\nabla_d \cdot (\rho^* \bar{u}^*) + \nabla_d \cdot (C_\rho P'_p \mathbf{D} \nabla_d P') \quad (4.5)$$

The relative importance of the first and second terms in Eq. (4.3) depends on the local Mach number (Shyy 1994). For low Mach number flows, only the first term prevails; for high Mach number flows, the second term dominates. The fourth term is a nonlinear second-order term and can be either neglected or included in the source term for stability in early iterations. In the present algorithm, the following relation between density and pressure correction is taken

$$\rho'_p = C(1 - \alpha_l)_p P'_p \quad (4.6)$$

where C is an arbitrary constant and it does not affect the final converged solution. The further details of the model can be obtained from Senocak and Shyy (2002a, 2004a) and Senocak (2002).

4.2 Pressure Implicit Splitting of Operators (PISO) Algorithm for Unsteady Computations

In the SIMPLE-type of the pressure-based methods (Patankar 1980, Shyy 1994), the equations are solved successively by employing iterations. In cavitating flow computations, the typical relaxation factors used in the iterative solution process are smaller than the ones used in single-phase flows, and hence smaller time steps are needed

to study the cavitation dynamics. Issa (1985) developed the PISO method for the solution of unsteady flows. The splitting of pressure and velocity makes the solution procedure sequential in time domain and enables the accuracy at each time step. It also eliminates the need for severe under-relaxation as in SIMPLE type algorithm. Bressloff (2001) extended the PISO method for high-speed flows by adopting the pressure-density coupling procedure in all-speed SIMPLE type of methods. Oliveira and Issa (2001) followed the previous PISO work to combine the temperature equation to simulate buoyancy-driven flows. Thakur and Wright (2002) and Thakur et al. (2004) developed approaches using curvilinear coordinates with suitability to all speeds. Senocak and Shyy (2002a) further extended this PISO algorithm to enhance the coupling of cavitation and turbulence models and to handle the large density ratio associated with cavitation.

The PISO algorithm contains predictor and correction steps. In the predictor step the discretized momentum equations are solved implicitly using the old time pressure to obtain an intermediate velocity field. A backward Euler scheme is used for the discretization of the time derivative term

$$\bar{u}_p^* = \mathbf{H}[\bar{u}^*]_p - D_p (\nabla_d P^{n-1})_p + \frac{(\rho \bar{u})^{n-1}}{\delta t} \quad (4.7)$$

The intermediate velocity field does not satisfy continuity and needs to be corrected using the continuity equation as a constraint. In the first corrector step, a new velocity field, \bar{u}^{**} and pressure field P^* are expected. The discretized momentum equation at this step is written as

$$\bar{u}_p^{**} = \mathbf{H}[\bar{u}^*]_p - D_p (\nabla_d P^*)_p + \frac{(\rho \bar{u})_p^{n-1}}{\delta t} \quad (4.8)$$

Subtracting Eq. (4.7) from Eq. (4.8), we have

$$\vec{u}_p^{**} = \vec{u}^* - D_p (\nabla_d P')_p \quad (4.9)$$

If the density field depends on the pressure field, such as in high Mach number flows or in cavitating flows, the density is corrected using the pressure-based method

$$\rho_p^* = \rho_p^{n-1} + \rho'_p, \quad \rho'_p = C_\rho P' \quad (4.10)$$

The discretized continuity equation written for the new velocity field and density field becomes

$$\frac{\rho_p^* - \rho_p^{n-1}}{\delta t} V_p + \Delta[\rho^* u^{**} \cdot \vec{n} S_{cf}]_p = 0 \quad (4.11)$$

Combining Eq. (4.9), (4.10) and (4.11), a first pressure-correction step equation is obtain below

$$\frac{C_\rho P'_p}{\delta t} + \Delta[\rho^{n-1} D(\nabla_d P') \cdot \vec{n} S_{cf}]_p + \Delta[C_\rho P' U^*]_p = -\Delta[\rho^{n-1} U^*]_p \quad (4.12)$$

To satisfy the mass conservation, the second corrector step is conducted to seek a new velocity field, \vec{u}^{***} and pressure field P^{**}

$$\vec{u}_p^{***} = \mathbf{H}[\vec{u}^{**}]_p - D_p (\nabla_d P^{**})_p + \frac{(\rho \vec{u})_p^{n-1}}{\delta t} \quad (4.13)$$

Subtracting Eq. (4.9) from Eq. (4.13) leads to the correction term

$$\vec{u}_p^{***} = \vec{u}_p^{**} + \mathbf{H}[\vec{u}^{**} - \vec{u}_p^*]_p - D_p (\nabla_d P'')_p \quad (4.14)$$

The corrected density field leads to

$$\rho_p^{**} = \rho_p^* + \rho''_p = \rho_p^{n-1} + \rho'_p + \rho''_p \quad (4.15)$$

The second pressure-correction step can be derived from Eq.(4.14), Eq. (4.15) and the mass continuity equation to reach the below format

$$\begin{aligned} \frac{C_p P''}{\delta t} + \Delta[\rho^* D(\nabla_d P'') \cdot \bar{n} S_{cf}]_p + \Delta[C_p P'' U^{**}]_p = -\Delta[\rho^* U^{**}]_p \\ - \Delta[\rho^* H(\bar{u}^{**} - \bar{u}^*) \cdot \bar{n} S_{cf}]_p \end{aligned} \quad (4.16)$$

Then, by solving the above predictor and correction steps coupled with the cavitation model, which was formulated in Chapter 3, and turbulence closures given in Chapter 2, the solution procedure for turbulent cavitating flow computations is accomplished.

4.3 Speed-of-Sound (SoS) Numerical Modeling

As mentioned in chapter 1, the harmonic speed-of-sound in the two-phase mixture is significantly attenuated. Therefore the multiphase flow fields are characterized by widely different flow regimes, such as incompressible in pure liquid phase, low Mach compressible in the pure vapor phase, and transonic or supersonic in the mixture. Consequently, an accurate evaluation of speed-of-sound is necessary and important.

From Eq. (4.6) and the definition of speed-of-sound, the relation between C_p and the speed-of-sound is

$$C_p = \left(\frac{\partial \rho}{\partial P}\right)_s = \frac{1}{c^2} \quad (4.17)$$

In high-speed flows, the exact form of the speed-of-sound can be computed easily from the equation of state. However, in cavitating flows, computation of the speed-of-sound is difficult. Each transport equation-based cavitation model defines a different speed-of-sound as a result of a more complex functional relationship. In the literature, there have been theoretical studies on defining the speed-of-sound in multiphase flows (Wallis 1969). One-dimensional assumption and certain limitations are typical in these studies. These definitions do not necessarily represent the actual speed-of-sound imposed

by the cavitation models of interest in this study. They can only be an approximation. On the other hand, the fundamental definition of speed-of-sound as given in Eq. (4.17) could be useful, and the path to compute the partial derivative is known. From these arguments, it is clear that the computation of the speed-of-sound in cavitating flows is an open question.

Due to the lack of a dependable equation of state for multiphase mixtures modeling sound propagation, Senocak (2002) and Senocak and Shyy (2003) present two numerical forms of speed-of-sound, called SoS-1 and SoS-2, and showed that the SoS-2 was more likely to produce the correct unsteady behavior in unsteady simulations. In the present study, these two different definitions for the speed-of-sound are further investigated in the pressure-density coupling scheme. The SoS-1 is the previous pressure-density coupling scheme with an order of 1 constant coefficient C as

$$\text{SoS-1:} \quad C_\rho = \left(\frac{\partial \rho}{\partial P}\right)_s = \frac{1}{c^2} \approx C(1 - \alpha_l) \quad (4.18)$$

The SoS-2 is based on an approximation made to the fundamental definition of speed-of-sound. It is assumed that the path to compute the partial derivative $\frac{\partial \rho}{\partial P}$ is the mean flow direction (ξ) other than the isentropic direction (s), because the details of thermodynamic properties are not known and the entropy can not be directly computed. This definition is referred to as SoS-2 in the rest of the study and given below

$$\text{SoS-2:} \quad C_\rho = \left(\frac{\partial \rho}{\partial P}\right)_s = \frac{1}{c^2} \approx \left(\frac{\Delta \rho}{\Delta P}\right)_\xi = \frac{|\rho_{i+1} - \rho_{i-1}|}{|P_{i+1} - P_{i-1}|} \quad (4.19)$$

The partial derivative is computed based on central differencing of the neighboring nodes. The absolute value function is introduced to make sure a positive value is computed.

Since the above approximation in SoS-2 is based on the mean flow direction, to generalize it, an averaged form is adopted. It will be referred as SoS-2A, taking the format as

$$\begin{aligned} \text{SoS-2A: } C_\rho = & \text{coff}u \cdot \frac{|\rho_{i+1,j,k} - \rho_{i-1,j,k}|}{|p_{i+1,j,k} - p_{i-1,j,k}|} + \text{coff}v \cdot \frac{|\rho_{i,j+1,k} - \rho_{i,j-1,k}|}{|p_{i,j+1,k} - p_{i,j-1,k}|} \\ & + \text{coff}w \cdot \frac{|\rho_{i,j,k+1} - \rho_{i,j,k-1}|}{|p_{i,j,k+1} - p_{i,j,k-1}|} \end{aligned} \quad (4.20)$$

with the velocity weight coefficients

$$\begin{aligned} \text{coff}u &= \frac{|u_{i,j,k}|}{|u_{i,j,k}| + |v_{i,j,k}| + |w_{i,j,k}|}, \text{coff}v = \frac{|v_{i,j,k}|}{|u_{i,j,k}| + |v_{i,j,k}| + |w_{i,j,k}|} \\ \text{coff}w &= \frac{|w_{i,j,k}|}{|u_{i,j,k}| + |v_{i,j,k}| + |w_{i,j,k}|} \end{aligned}$$

CHAPTER 5
ASSESSING TIME-DEPENDENT TURBULENT CAVITATION MODELS

5.1 Cavitating Flow through a Hollow-Jet Valve

There are serious implications on the safe and sound operation in flow-control valve cavitation phenomena. A limited number of experimental studies have been published on this topic, such as those by Oba et al. (1985) and Tani et al. (1991a,b). In addition, Wang (1999) used high-speed cameras and Laser Light Sheet (LLS) to observe the cavitation behavior in a hollow-jet valve under various cavitation conditions and for different valve openings. However, to the best of our knowledge, to date, no comprehensive numerical study has been done in this respect. Furthermore, complex geometries and inaccessible regions of occurrence restrain experimental investigations in cavitation. Hence, we investigate the capability of transport equation-based cavitation models to predict incipient level cavitation.

As documented in Wang (1999), Figure 5-1 shows the geometry and the main configurations of the valve. A key component is the needle, used to control the flow rate by moving to different location in the x-direction. A cylindrical seal supports the needle. There are six struts supporting the cylinder in the pipe center, which are called splitters. The gear is used to control the needle position moving through the x-axis.

Figure 5-2 illustrates the computational domain in selected planes according to the geometry. A multi-block structured curvilinear grid is adopted to facilitate the computation. Figure 5-2A shows the configuration on the X-Y plane, and Figure 5-2B from the Y-Z plan. Figure 5-2C shows the plane's location, and Figure 5-2D shows the

boundary conditions in the computations. In the present study, the splitter thickness is neglected and its shape is considered to be rectangular. The Reynolds number is 5×10^5 and the cavitation number is 0.9, with the density ratio between the liquid phase and vapor phase ρ_l/ρ_v being 1000 in the water, and the valve opening is 33%.

Two investigations are conducted here using the original interfacial dynamics-based cavitation model (IDM) (Section 3.3), using the Launder-Spalding model (LSM) (Section 2.2) as turbulence closure. We study steady and unsteady computations. In steady-state, we adopt SoS-2. In time-dependent simulations, we further examine the two different SoS impact, including SoS-1 and SoS-2 (Section 4.3), which have been firstly investigated by Senocak and Shyy (2004b) in cavitating flows. For the time-dependent computation, the steady single-phase turbulent flow, without considering cavitation, is computed and then the solution is adopted as the initial condition for the unsteady cavitating turbulent flow. The results and discussion are presented in the following.

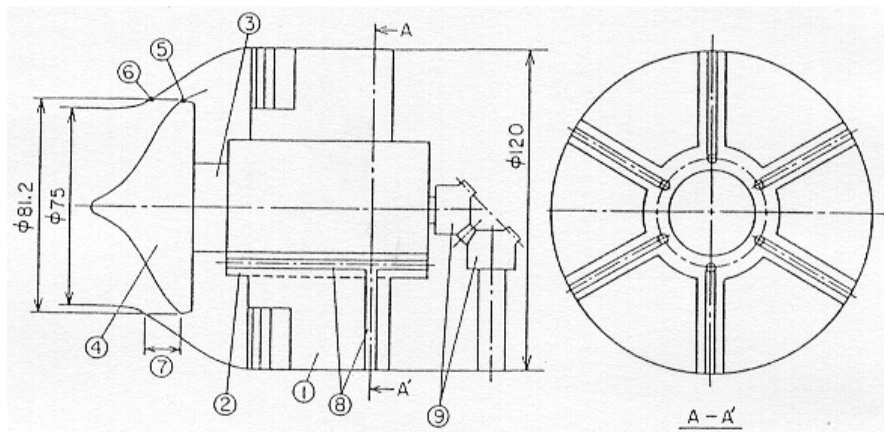


Figure 5-1. Valve geometry. (1) Splitter. (2) Cylinder. (3) Plunger. (4) Needle. (5) Needle seal overlay. (6) Seal seat inlay. (7) Stroke. (8) Ventilation duct. (9) Gear

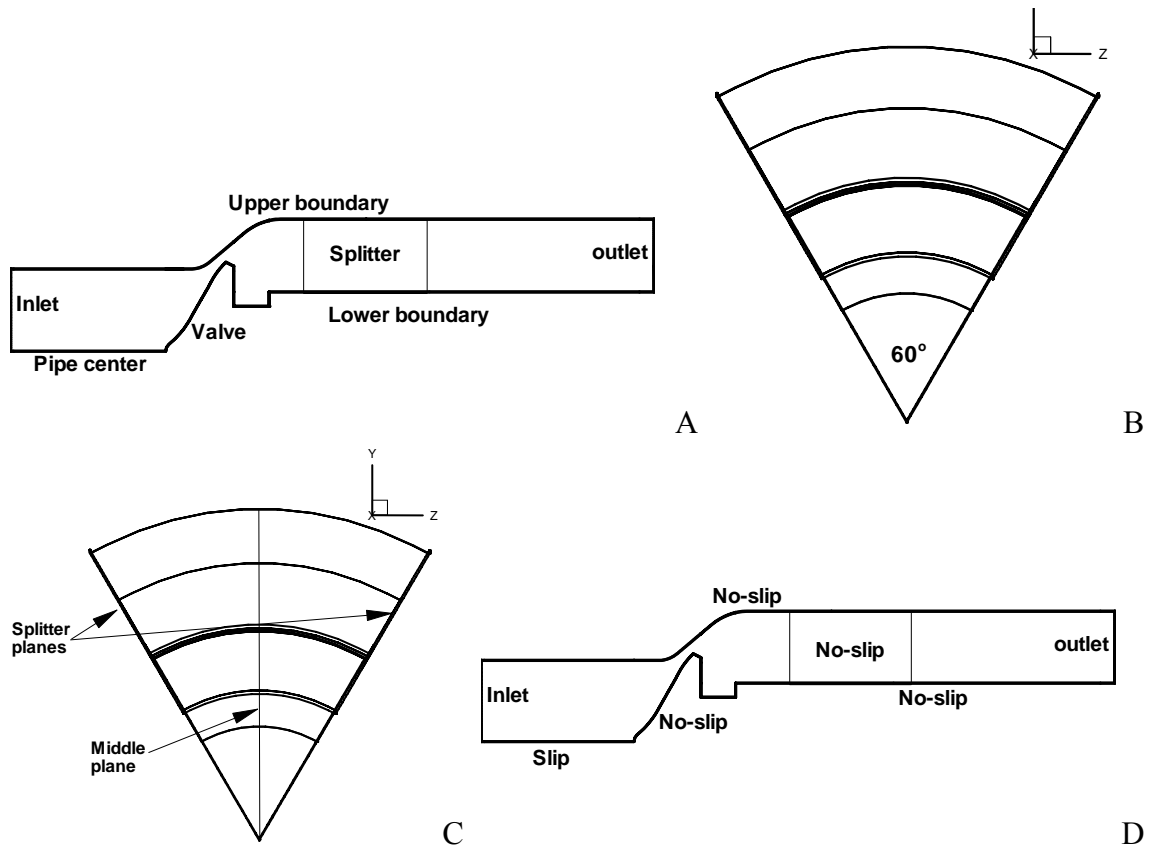


Figure 5-2. Computational domains and boundary conditions. A) Computational domain in X-Y plane. B) Computational domain in Y-Z plane. C) Planes location. D) Boundary conditions

5.1.1 Steady and Unsteady Turbulent Cavitating Flows

Figure 5-3 shows the density distributions for the steady situation. The cavity is located at the valve tip. The comparison shows that the cavities on the splitter plane and the middle plane are slightly different in size. Figure 5-4 shows how the cavity shape and location vary with time.

For time-dependent computations, the cavity fluctuates quasi-periodically. At non-dimensional time $t^* = t/t_\infty = 0.4$, the cavity is the biggest with smallest density, see Figure 5-4A. As time passes, the cavity size reduces to the smallest in Figure 5-4(B, C) at time $t^* = 0.6$ and $t^* = 0.8$, respectively. After one cycle it reaches the maximum again (Figure 5-4D at time $t^* = 1.2$ s). Both steady and unsteady results exhibit the cavity at the needle tip

(Figure 5-3 and Figure 5-4). The steady case corresponds to a single instantaneous result in the time-dependent solution (Figure 5-3B and Figure 5-4C). The time-dependent results are qualitatively consistent with the experiment in size and shape (Figure 5-4). Unfortunately, there is insufficient experimental information to ascertain the time-dependent characteristics in detail.

The experiment observed that the cavities incept, grow, then detach from the needle tip and transport to the downstream periodically, which is clearly shown in Figure 5-4E. However, as already discussed in Senocak (2002), with the current combination of turbulence and cavitation models, the detachment of the cavity is not captured, possibly due to the representation of the turbulence via a scalar eddy viscosity. Henceforth, the issue is under further investigation in following by means of adopting different turbulence models.

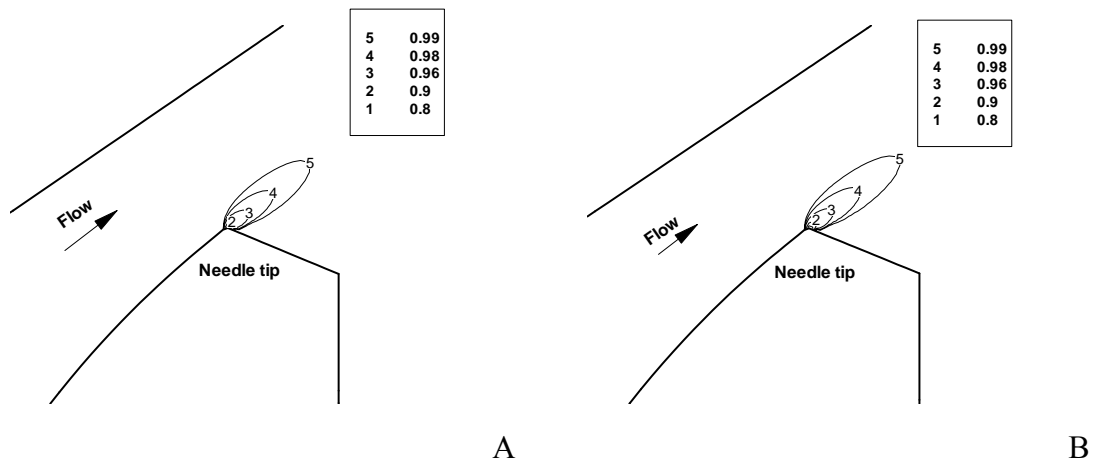


Figure 5-3. Density contour lines of the steady state solution (The mixture of vapor and liquid inside the outer line forms the cavity), original IDM with SoS-1, LSM. A) At splitter plane. B) At middle plane

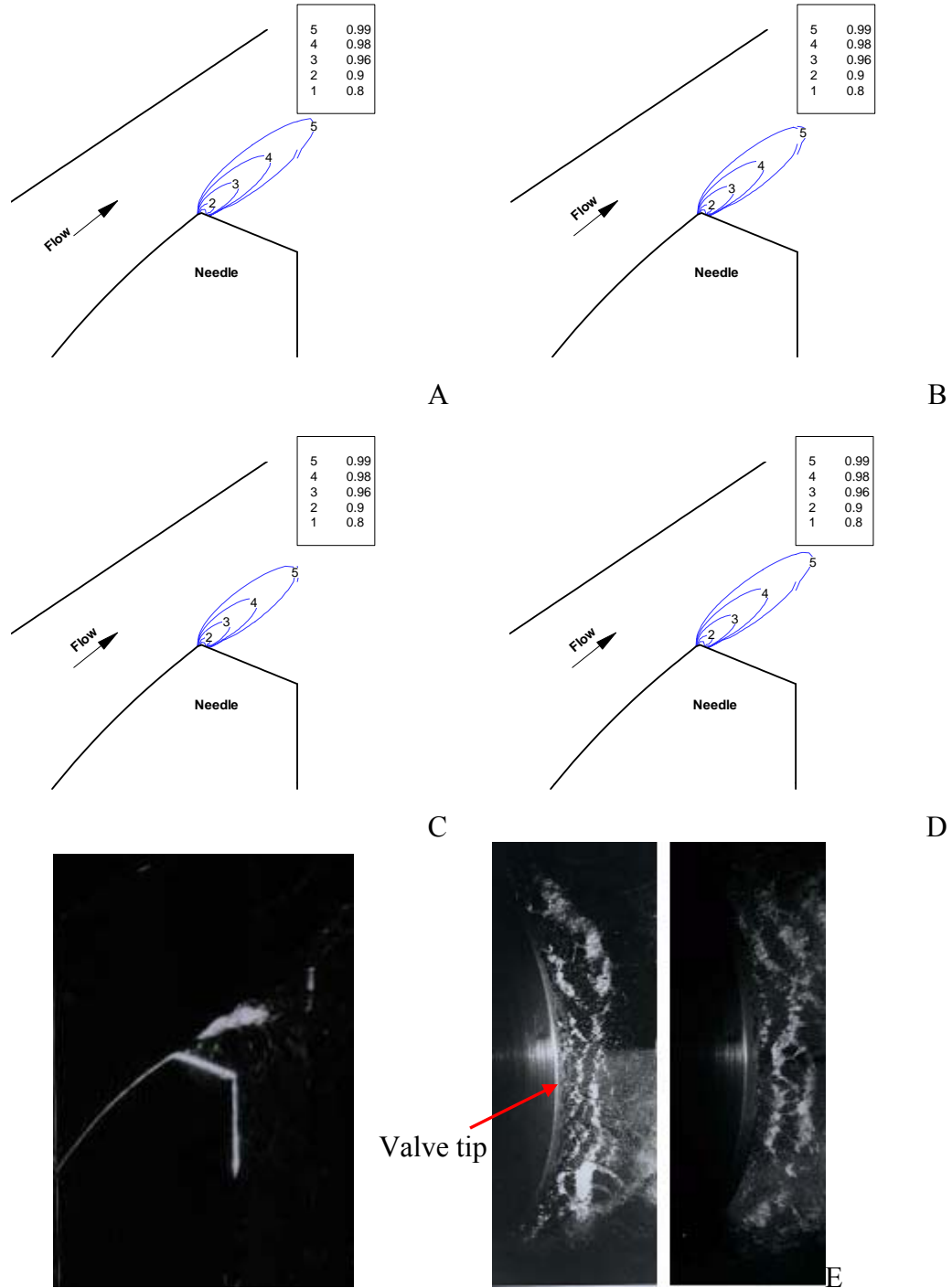


Figure 5-4. Middle section density contours at different time instants (The mixture of vapor and liquid inside the outer line forms the cavity), original IDM with SoS-2, LSM. A) Time $t^*=0.4$. B) Time $t^*=0.6$. C) Time $t^*=0.8$. D) Time $t^*=1.2$. E) Experimental observations from Wang (1999): cavity at needle tip and cavitation aspects around the needle

To further demonstrate the cavity-induced quasi-periodic characteristics of the flow field, Figure 5-5 highlights the time evolutions at selected locations. Figure 5-5A shows the locations of the points selected. The pressure is at the middle points, and the density is near the bottom boundary, just one point away from it. From Figure 5-5B, at the places away from the cavity, A, B and D, the density is constant since only the liquid phase exists there, and is quasi-periodic inside the cavity at Point C. On the other hand pressure oscillates in the whole domain except on the inlet plane, where the flow condition is fixed (Figure 5-5C).

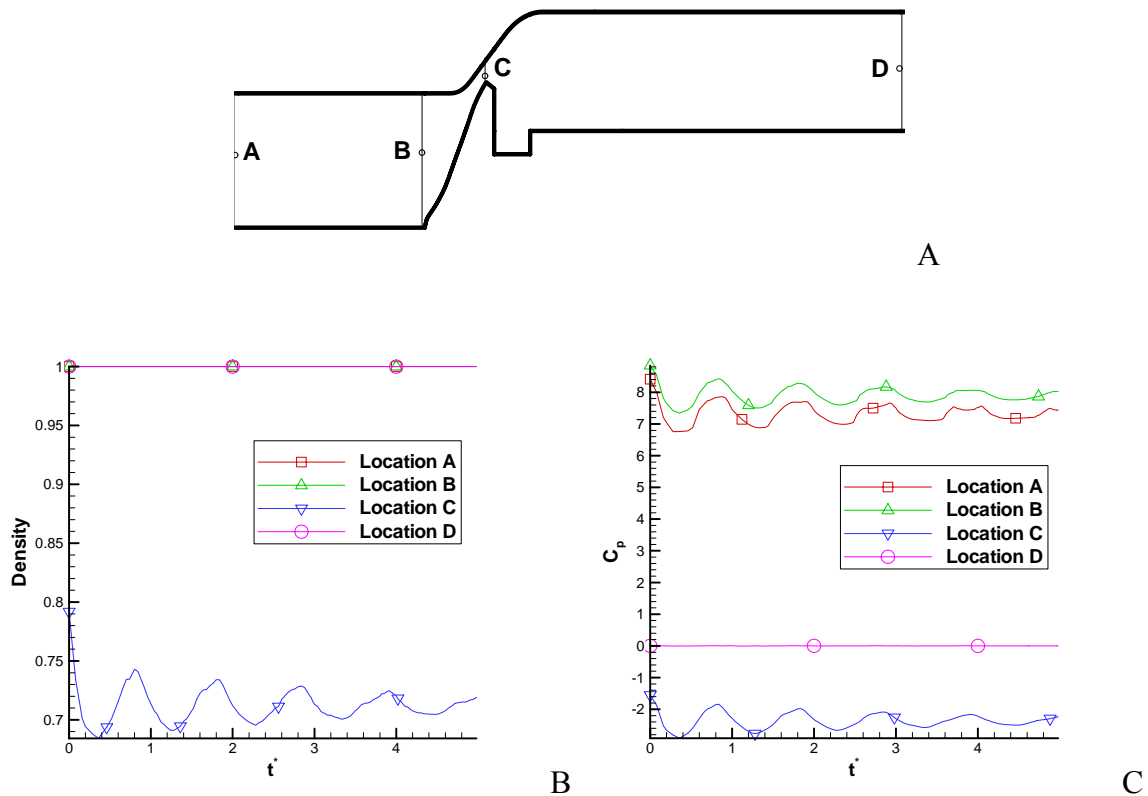


Figure 5-5. Time evolutions at different locations, original IDM with SoS-2, LSM. A) Samples locations. B) Density. C) Pressure

Figure 5-6 presents the flow structure on the middle plane. For the steady case, the flow fields of both single phase (without invoking the cavitation model in the course of computation) (Figure 5-6A) and cavitating flows are almost identical (Figure 5-6B). It

indicates that in the present case, the detailed cavitation dynamics does not exhibit substantial influence on the overall flow pattern. For the time-dependent case, at different time instants, $t^*=0.4$ and $t^*=0.8$ (Figure 5-6C), the flow field around the needle remains largely the same. The comparison between the steady and unsteady case indicates that there is not very much difference in the flow pattern. As expected, there are two recirculating zones: one behind the needle and the other one downstream around the splitter region, which is located at about $x=3.4\sim 4.2$. Compared with the experimental observation in Figure 5-6D (the cavitating flow structures behind the needle, and in the splitter region), the present results are in general agreement.

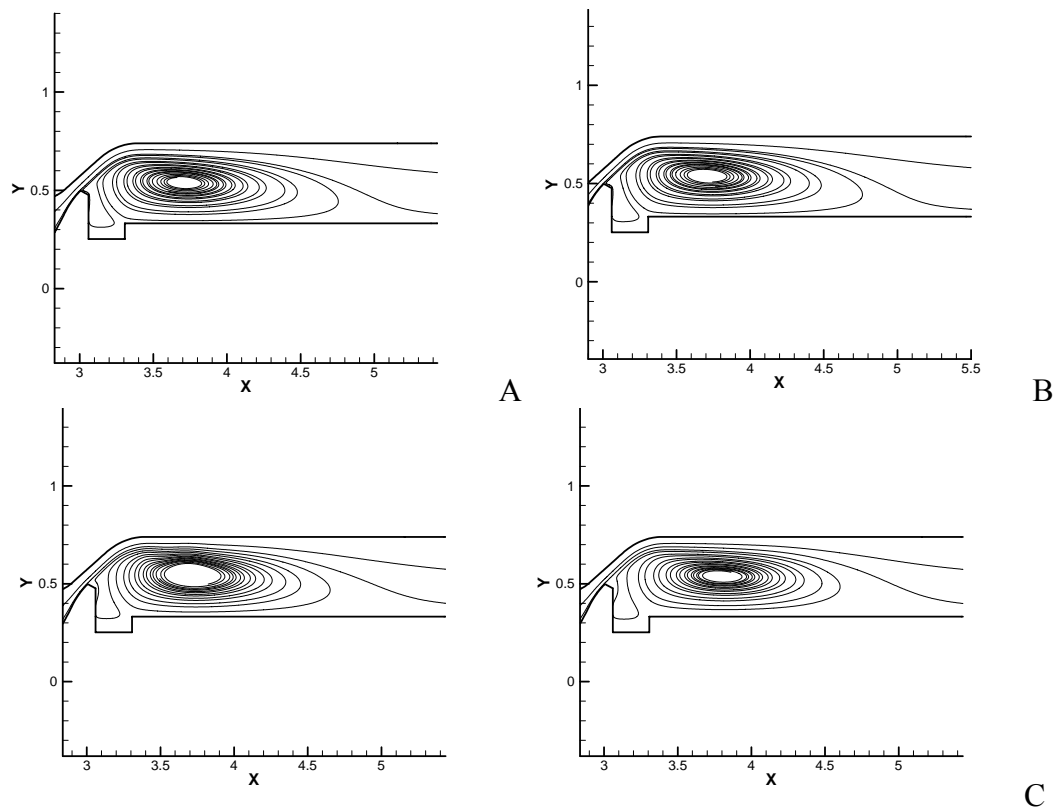


Figure 5-6. Projected 2-D streamlines at middle plane and experimental observation. A) Steady single-phase flow, LSM. B) cavitating flow, original IDM with SoS-2, LSM (Right). B) Unsteady cavitating flow at time $t^*=0.4$ (Left) and $t^*=0.8$ (Right). D) Flow pattern from Wang (1999), behind valve about $x=3.0\sim 3.4$ (Left) and at splitter region about $x=3.4\sim 4.2$ (Right)

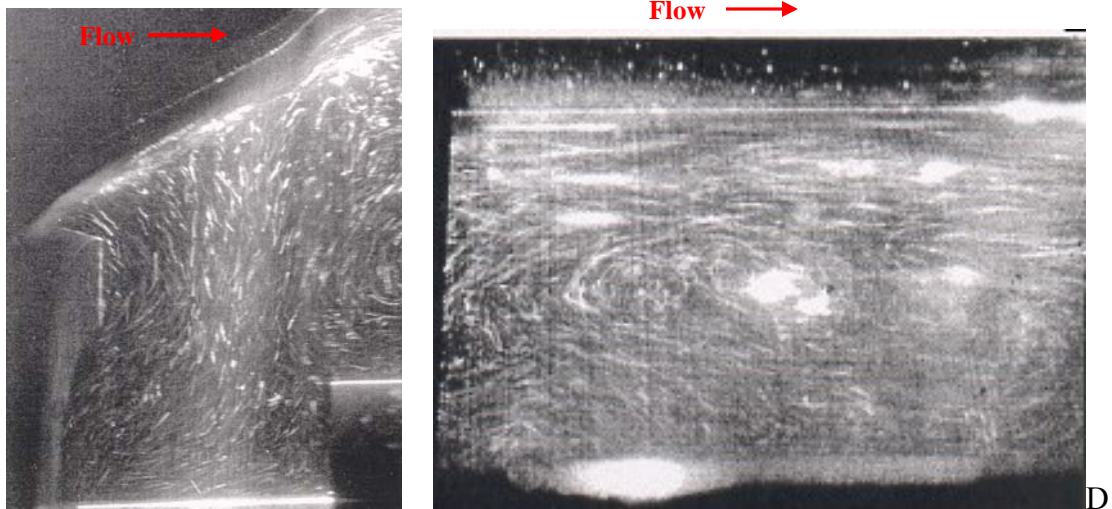


Figure 5-6. Continued

5.1.2 Impact of Speed-of-sound Modeling

We further examine the behavior of the different handlings of speed-of-sound (Chapter 4), that is, SoS-1 and SoS-2.

Figure 5-7 shows the variation in cavity shapes and location for LSM at maximum and minimum fraction instants. Compare the half period between maximum and minimum instant, the cavity oscillation for SoS-1 is distinguished by a significantly higher frequency and moderately higher amplitude than for SoS-2 (Figure 5-7A, B). These observations, as also discussed later, are a precursor to the significant impact produced by the speed-of-sound definition on the flow time scales. The qualitative shape and location of the cavity for both SoS-1 and SoS-2, however, are similar to the experimental observations (Figure 5-6D). Senocak and Shyy (2003,2004b) pointed out that SoS-2 performed better than SoS-1 in simulating the oscillatory behavior of the cavitating flow in the convergent-divergent nozzles, because SoS-2 successfully produced a quasi-steady solution at high cavitation number and a periodic solution at low cavitation number. In Figure 5-8, SoS-2 and SoS-1 behave similarly in this computed

case, and they both are nearly constant when away from the pure phase. These qualitatively agree with the theoretical analysis (Figure 1-2). Also, this helps to explain why the cavity shapes of the two different SoS models are qualitatively close. One thing needs to be pointed out here that the volume fraction is very close to the pure liquid phase. Hence the linear approximation SoS-1 can have similar behavior as SoS-2.

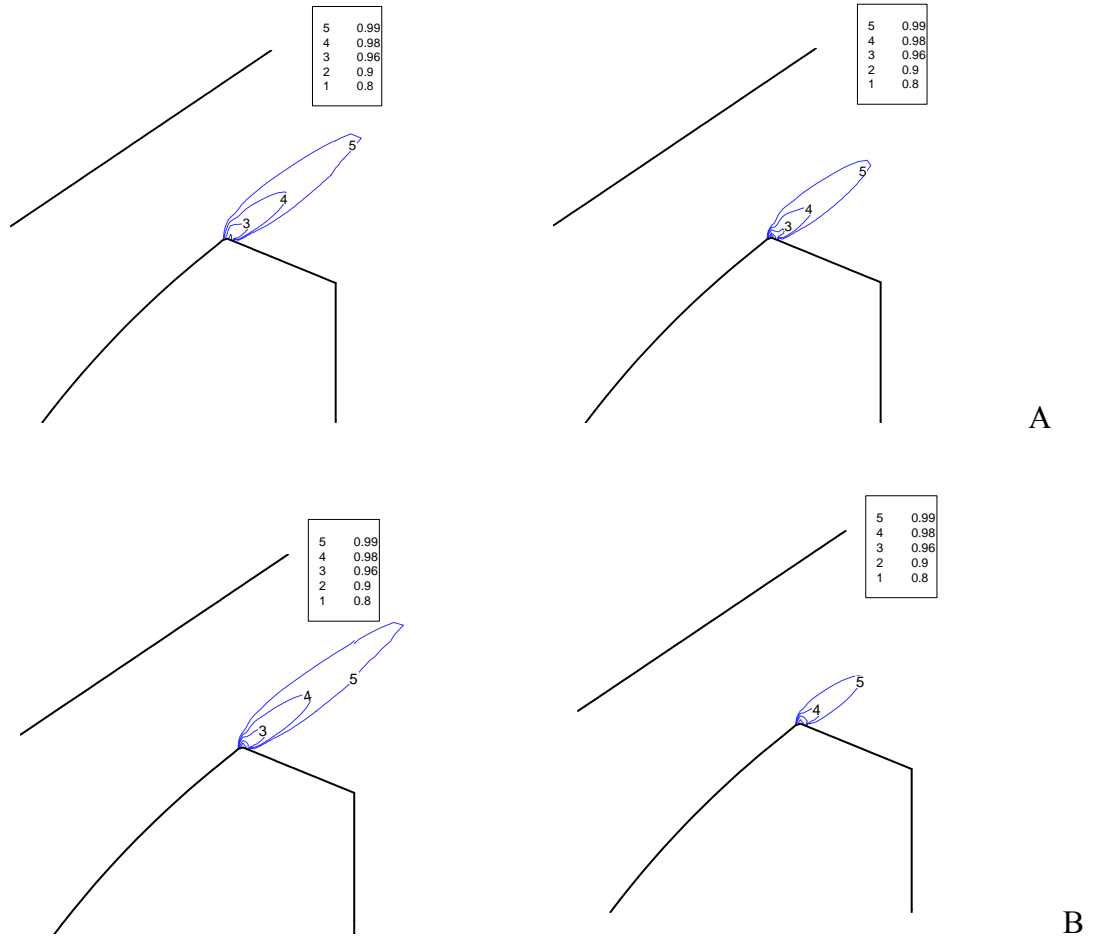


Figure 5-7. Middle section density contours of different SoS at different instants (the mixture of vapor and liquid inside the outer line forms the cavity), original IDM, LSM. A) SoS-2, maximum fraction at $t^*=0.32$ (Left) and minimum fraction at $t^*=0.77$ (Right). B) SoS-1, maximum fraction at $t^*=5.92$ (Left) and minimum fraction at $t^*=5.86$ (Right)

Lack of substantial experimental data prevents us from making more direct comparisons at this stage. Various experimental studies have shown that, besides oscillating, the cavities incept, grow, detach from the needle tip and get periodically

transported downstream (Figure 5-4E). The periodic detachment and inception of cavities is, however, difficult to capture through currently known turbulence and SoS models (Wang et al. 2001, Senocak and Shyy 2003, Coutier-Delgosha et al. 2003, Wu et al. 2003 a). Consequently, fundamental understanding on the above modeling aspects, which is discussed in the following sections, is imperative to encounter the above limitation. The following discussions serve to probe the sensitivity of the various modeling concepts, guided by our qualitative, but incomplete, insight into the fluid physics.

The implications of speed-of-sound (SoS) definition are quantified by a correlation study (Table 5-1 and Table 5-2) and spectral analysis (Figure 5-10) on a series of pressure-density time history at various nodes in cavitation vicinity. The Pearson's correlation (r) between pressure and density is calculated as

$$r = \frac{\sum_i^N [(X_i - \bar{X})(Y_i - \bar{Y})]}{\sqrt{\sum_i^N (X_i - \bar{X})^2} \sqrt{\sum_i^N (Y_i - \bar{Y})^2}}; \quad X = P, \quad Y = \rho \quad (5.1)$$

Table 5-1 and Table 5-2 indicate that within similar variation limits of liquid volume fraction, SoS-1 has a broader range of pressure-density correlation coefficients than SoS-2. Furthermore, SoS-2 consistently exhibits much stronger pressure-density coefficients than SoS-1. The distinct effects produced by the speed-of-sound definition are further corroborated by the dramatic time scale differences observed from the time history and FFT plots of pressure and density (Figure 5-9 and Figure 5-10A, B, C). SoS-1 plots clearly indicate dominance of a single high-frequency compressibility effect unlike SoS-2, which are characterized by a wider bandwidth for pressure and density, and a lower dominant frequency. It is worth noting here that although the plots in Figure 5-9(B,

C) are plotted against a smaller time range, we have used a convincingly long time history for our analysis.

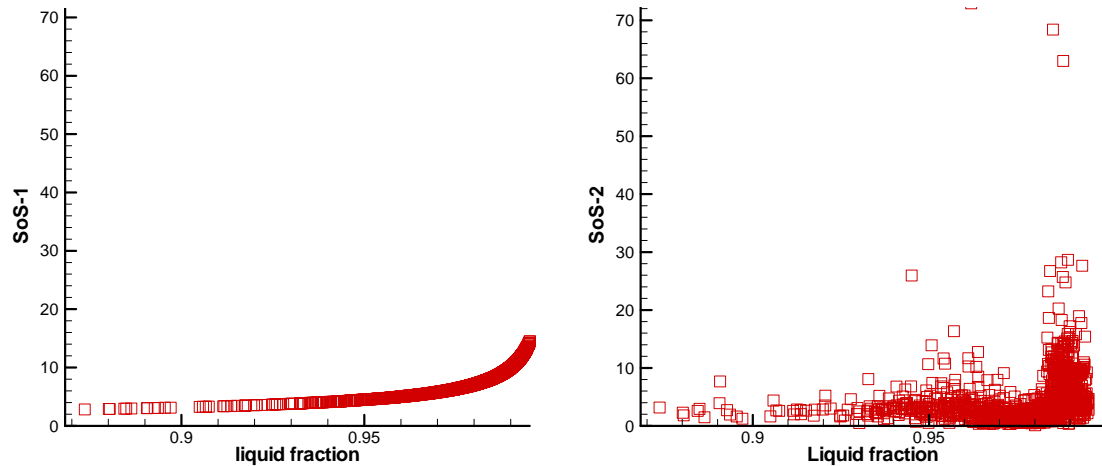


Figure 5-8. Two different SoS in hollow-jet valve flow, original IDM, LSM

Table 5-1. Time-averaged liquid volume fraction v/s pressure-density correlation at multiple points inside the cavity, original IDM with SoS-1, LSM

Time averaged liquid volume fraction (α_i)	Pearson's correlation (r) between pressure and density (SoS-1)
0.862	-0.674
0.882	-0.09
0.936	0.093
0.970	-0.045
0.978	-0.077
0.983	-0.096
0.986	-0.103
0.988	-0.12
Mean(r) = -0.13; SD(r) = 0.9	

Table 5-2. Time-averaged liquid volume fraction v/s pressure-density correlation at multiple points inside the cavity, original IDM with SoS-2, LSM

Time averaged liquid volume fraction (α_i)	Pearson's correlation (r) between pressure and density (SoS-2)
0.858	-0.733
0.868	-0.106
0.934	-0.106
0.968	-0.46
0.977	-0.47
0.982	-0.412
0.985	-0.412
0.987	-0.412
Mean(r) = -0.42; SD(r) = 0.1	

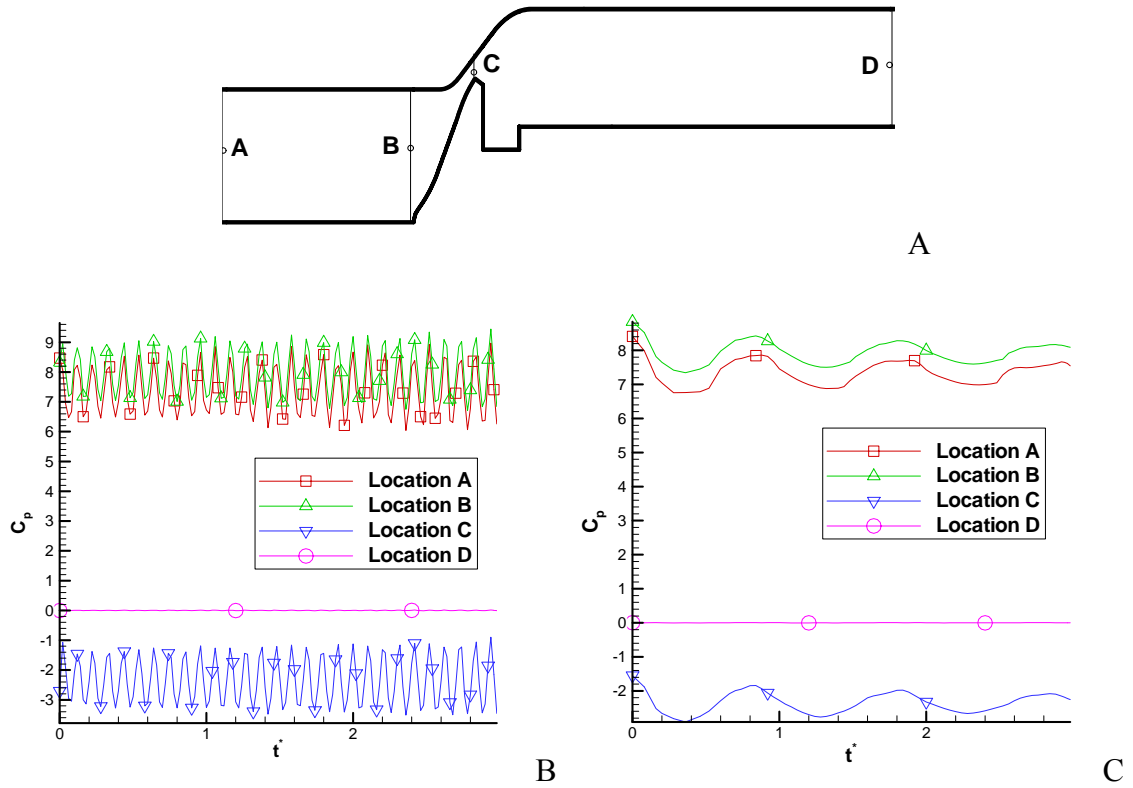


Figure 5-9. Pressure time evolutions of different SoS, original IDM, LSM. A) Samples locations. B) SoS-1. C) SoS-2

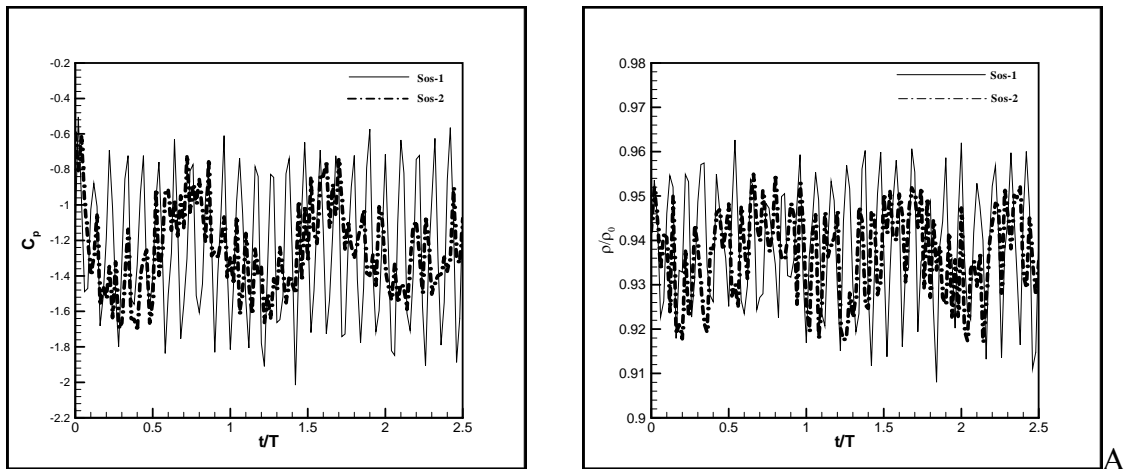


Figure 5-10. Time evolution and spectrum of pressure and density of two SoS definitions at a point at the cavitation vicinity, original IDM, LSM. A) Pressure (Left) and density (Right) time history. B) Spectral analysis on pressure (Left) and density (Right, SoS-1). C) Spectral analysis on pressure (Left) and density (Right), SoS-2

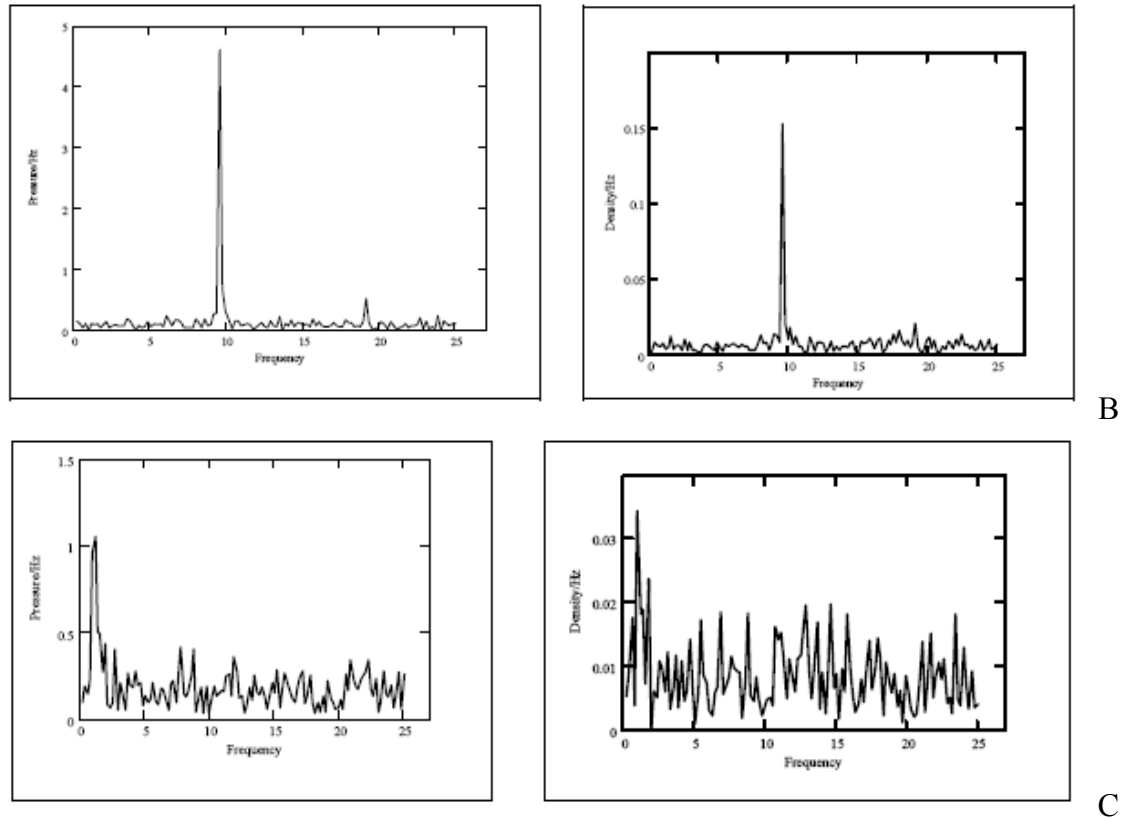


Figure 5-10. Continued

5.2 Turbulent Cavitating Flow through a Convergent-Divergent Nozzle

To study the performance of the filter-based model (FBM, Section 2.3), and the modified IDM (Section 3.3) in time-dependent computations, the turbulent cavitating flow through a convergent-divergent nozzle is investigated.

Stutz and Reboud (1997, 2000) have studied the unsteady cavitation formed in a convergent-divergent nozzle that has a convergent part angle of 18° and a divergent part angle of 8° . The experimental Reynolds number is $Re = 10^6 \square 3 \times 10^6$ based on the reference velocity and cavity length. Cavitation formed in this nozzle is described as “unsteady and vapor cloud shedding”. Senocak and Shyy (2003, 2004b) conducted the numerical simulations using IDM coupled with the LSM. They found that under cavitation number $\sigma = 1.98$, the cavity length L_{cav} matched the experiments (Stutz and

Reboud 1997, 2000), which did not specify the cavitation number. Therefore, to be consistent, we use $\sigma = 1.98$ in the present study.

First, we apply the original IDM with SoS-2 for the simulations to assess the FBM performance.

To test the grid and filter size dependency, two grids are adopted including a coarse grid with $\Delta = 0.5L_{cav}$ and a fine grid with $\Delta = 0.25L_{cav}$. The time-averaged eddy viscosity contours of two grids are given in Figure 5-11. The FBM gives effective viscosities for both grids about half an order of magnitude lower than that produced by the LSM. The differences of the time-averaged eddy viscosity are noticeable between the two grids. The largest viscosity on the fine grid is lower and its location shifts to the upstream, compared with Figure 5-11(A, B) left and right columns correspondingly. However, the time-averaged vapor volume fraction does not show significant difference (Figure 5-12A, B). The time-averaged u-velocity profiles have the similar trend.

Hereafter, all the results are based on the fine grid with $\Delta = 0.25L_{cav}$. Figure 5-13 shows the time-averaged velocity and vapor volume fraction profiles within the cavity at four different sections, using two different turbulence models. The boundaries of the cavitating region, from experiments, LSM and FBM, are also included. Although the numerical results of the cavitating boundaries are about 5% higher than that from the experiments, the computations capture the main cavity body and the overall trends are agreeable (Figure 5-13B). The velocity profiles qualitatively agree with the experimental data, especially in the core of the reverse flow (Figure 5-13A). Comparing the LSM and FBM, both the time-averaged velocity and volume fraction show marginal difference. However, the instantaneous velocity and volume fraction profiles display significant

differences (Figure 5-14). The current results show an auto-oscillating cavity. Here only the maximal- and minimal-volume fraction time instants are presented. The maximal-volume fraction of the FBM is bigger than that of the LSM. On the contrary, the minimal-volume fraction is much smaller by comparing Figure 5-14A and Figure 5-14B. The reverse velocity profiles show the same trend. The increase in fluctuations is due to the FBM reducing the eddy viscosity (Figure 5-11). The observation reveals that the time-averaging process can be misleading and not suitable as the only indicator for performance evaluation, which is similar to the previous study by Wu et al. (2003b).

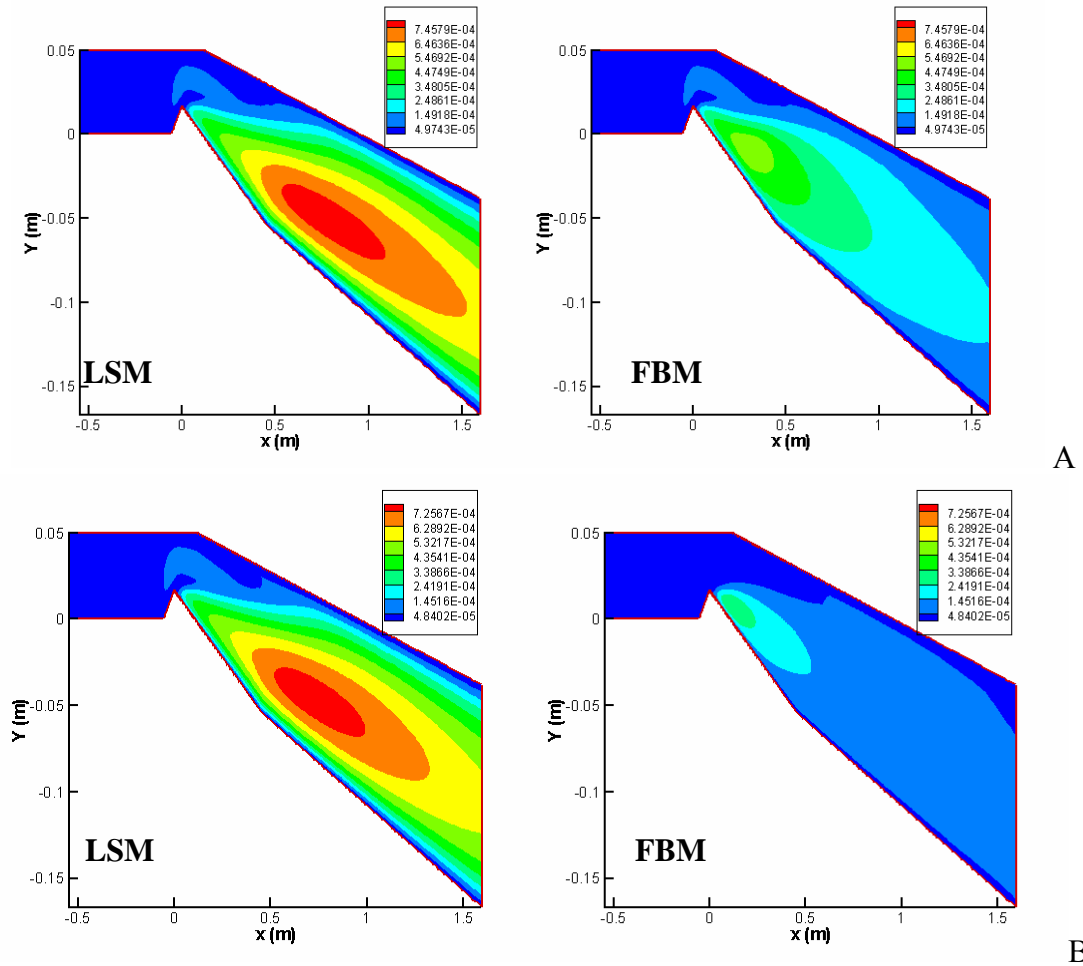


Figure 5-11. Time-averaged eddy viscosity contours of different grids, original IDM with SoS-2, $\sigma = 1.98$. A) Coarse grid with $\Delta = 0.50L_{cav}$. B) Fine grid with $\Delta = 0.25L_{cav}$

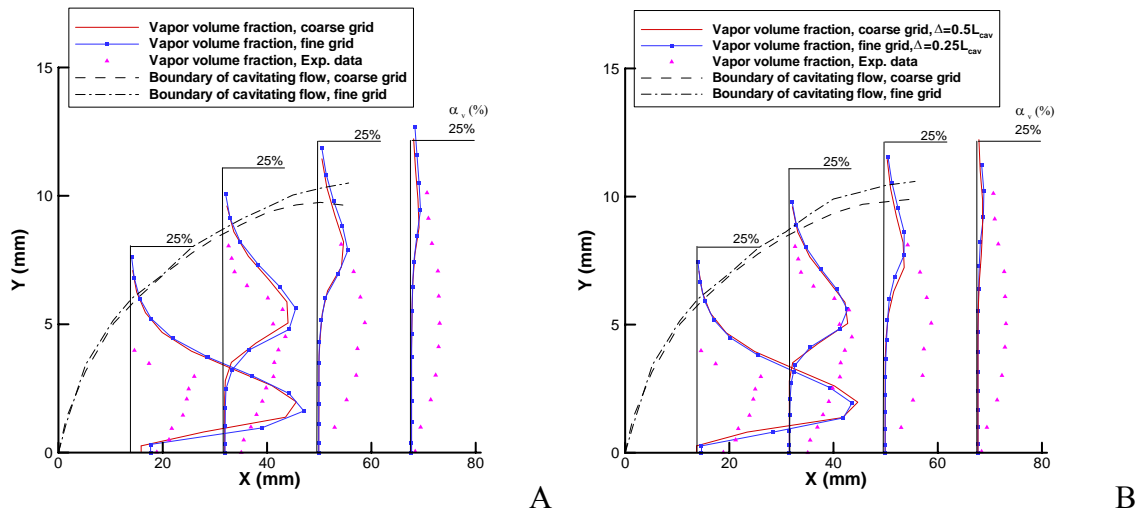


Figure 5-12. Time-averaged vapor volume fraction comparisons of different grids, original IDM with SoS-2, $\sigma = 1.98$. The vertical scale is the distance from the wall. Experimental data are from Stutz and Reboud (1997&2000). A) LSM. B) FBM

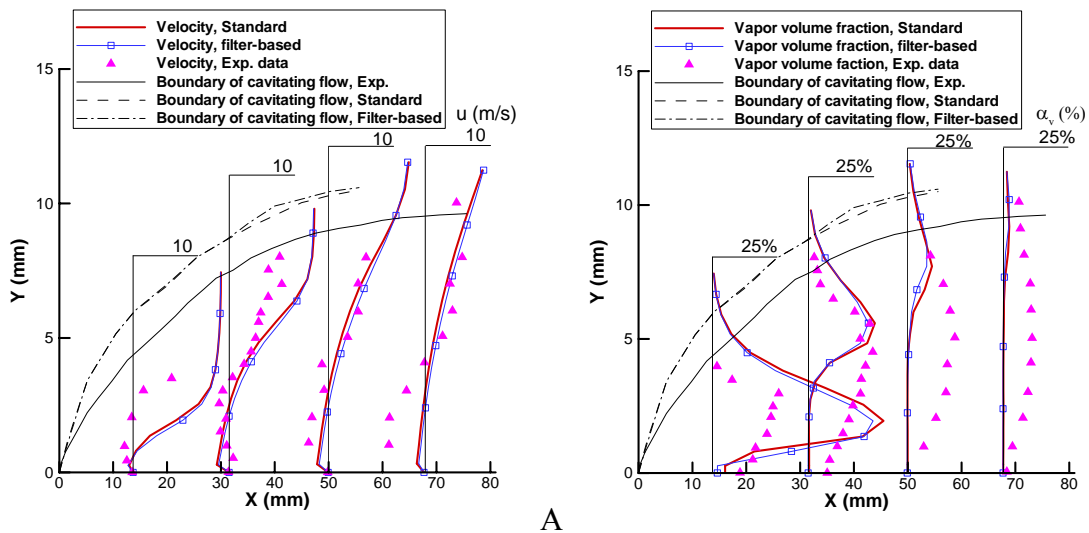


Figure 5-13. Time-averaged comparisons of different turbulence models on fine grid with $\Delta = 0.25L_{cav}$, original IDM with SoS-2, $\sigma = 1.98$. The vertical scale is the distance from the wall. Experimental data are from Stutz and Reboud (1997&2000). A) U-velocity. B) Vapor volume fraction

An illustration that the FBM can induce noticeably stronger flow oscillations is presented in Figure 5-15. It is observed that time-averaged pressure contours and streamlines are similar at the cavity zone, although a recirculation region produced by the FBM exists at downstream near the lower wall (Figure 5-15A). However, the

instantaneous pressure contours and velocity field produced by the two turbulence models are distinctly different. The FBM yields wavy flow structures, which induce the auto-oscillation of the flow fields in Figure 5-15(B, C). The experimental measurements (Figure 5-14) are confined in the throat region, which have missed the large scale unsteadiness of the flow field.

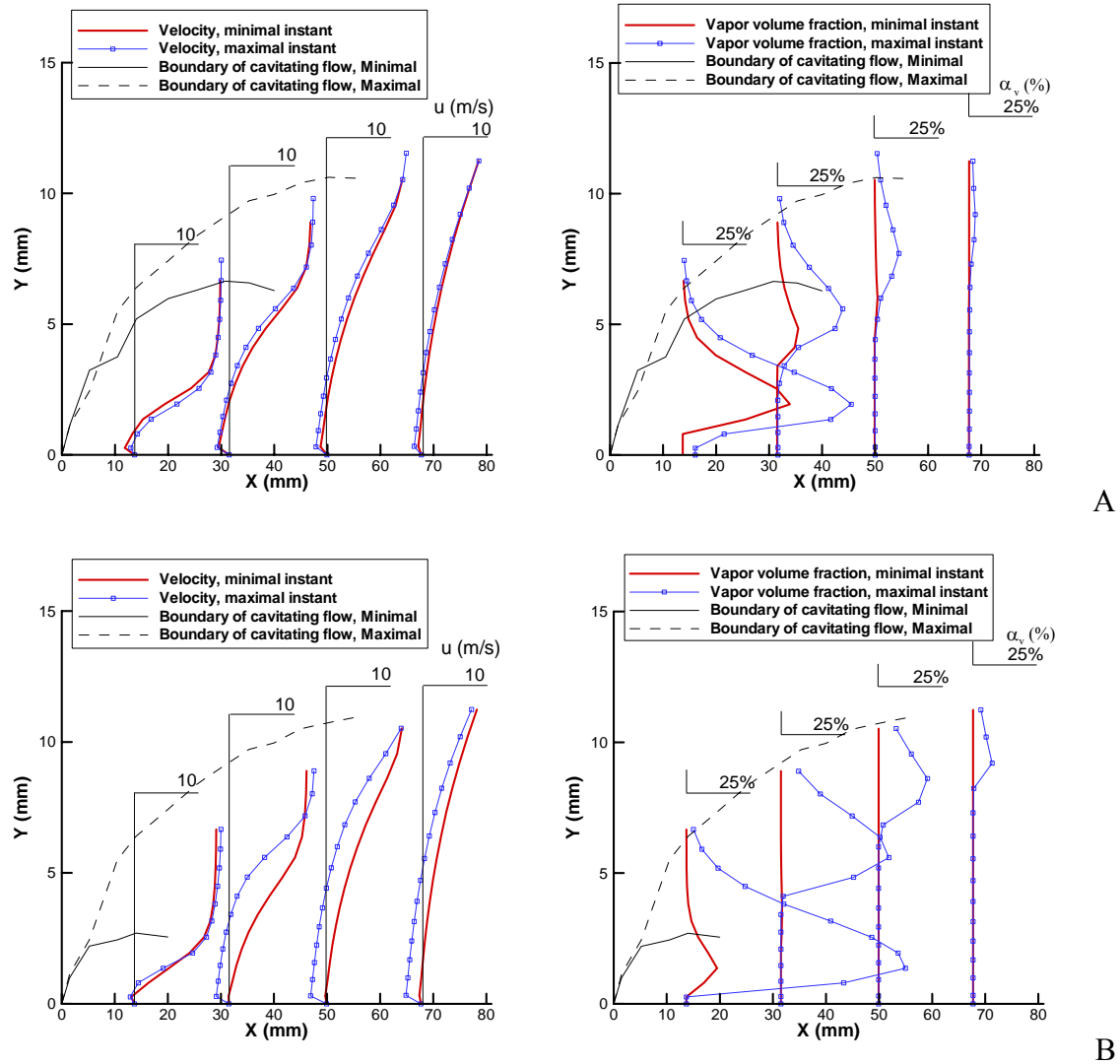


Figure 5-14. Instantaneous profiles on fine grid with $\Delta = 0.25L_{cav}$, original IDM with SoS-2, $\sigma = 1.98$. The vertical scale is the distance from the wall. A) LSM: u-velocity and vapor volume fraction. B) FBM: u-velocity and vapor volume fraction

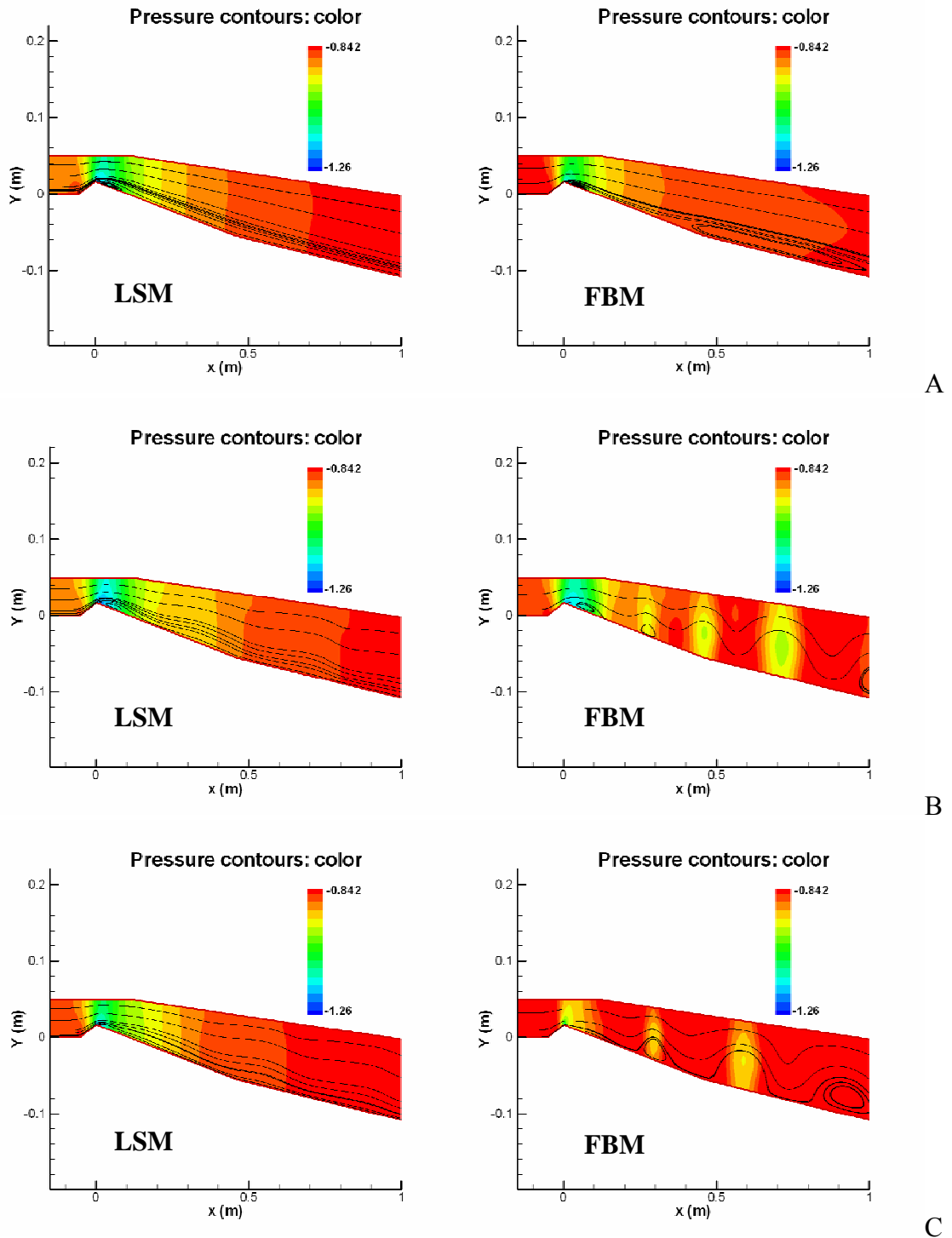


Figure 5-15. Pressure contours and streamlines comparison of two turbulence models on fine grid, original IDM with SoS-2, $\sigma = 1.98$. A) Time-averaged. B) At maximal-volume fraction instant. C) At minimal-volume fraction instant

Obviously, both turbulence and cavitation models directly affect the cavity dynamics such as the shedding pattern and frequency. Hence in this section, we further investigate the implication of the cavitation model in the context of the interfacial velocity estimated, as discussed in Section 3.3 which is called the modified interfacial dynamics-based cavitation model. The speed-of-sound (SoS) is based on the SoS-2A, formulated in Section 4.3. The turbulence closure is employed the original Launder-Spalding model (LSM) described in Section 2.2. The detailed results are presented below.

Figure 5-16 gives the time history of the pressure at a reference point near the inlet. The pressure of the original IDM, which adopts an empirical factor to assign the interfacial velocity based on the local fluid velocity in Section 3.3 Eq. (3.9), exhibits much smaller variation than that computed with the modified IDM. As given in table 5-3, although both IDMs under-predict the Strouhal number, the dynamically adjusted interfacial velocity embodied by the modified IDM yields better agreement compared with the experimental measurement.

Selected time evolutions of the cavity shape and the associated flow structures are presented in Figure 5-17 with the available experimental observation. The original IDM demonstrates an attached periodic cavity, while the modified IDM produces cavity break-up and detachment, in manners qualitatively consistent with the experimental observations. The cavity break-up and collapse of the modified IDM also helps to explain the C_p behavior shown Figure 5-16. Furthermore, because of the shedding of the cavity, the modified IDM better predicts the vapor volume fraction profiles than the original IDM, with less difference in the velocity profiles between these two cavitation models (Figure 5-18).

Table 5-3. Comparisons of Strouhal number of original and modified IDM with SoS-2A

Original IDM, SoS-2A	Modified IDM, SoS-2A	Experiment
0.07	0.13	0.30

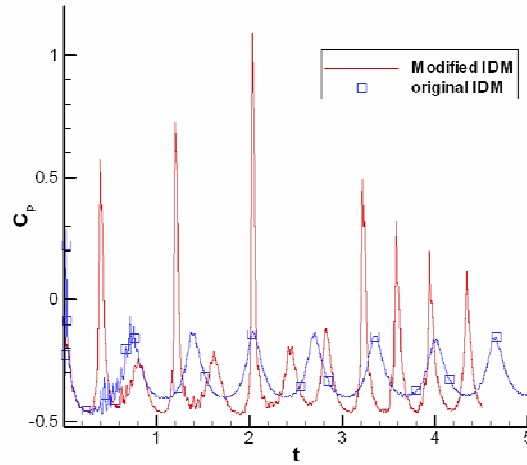


Figure 5-16. Pressure evolutions of original and modified IDM with SoS-2A at a reference point

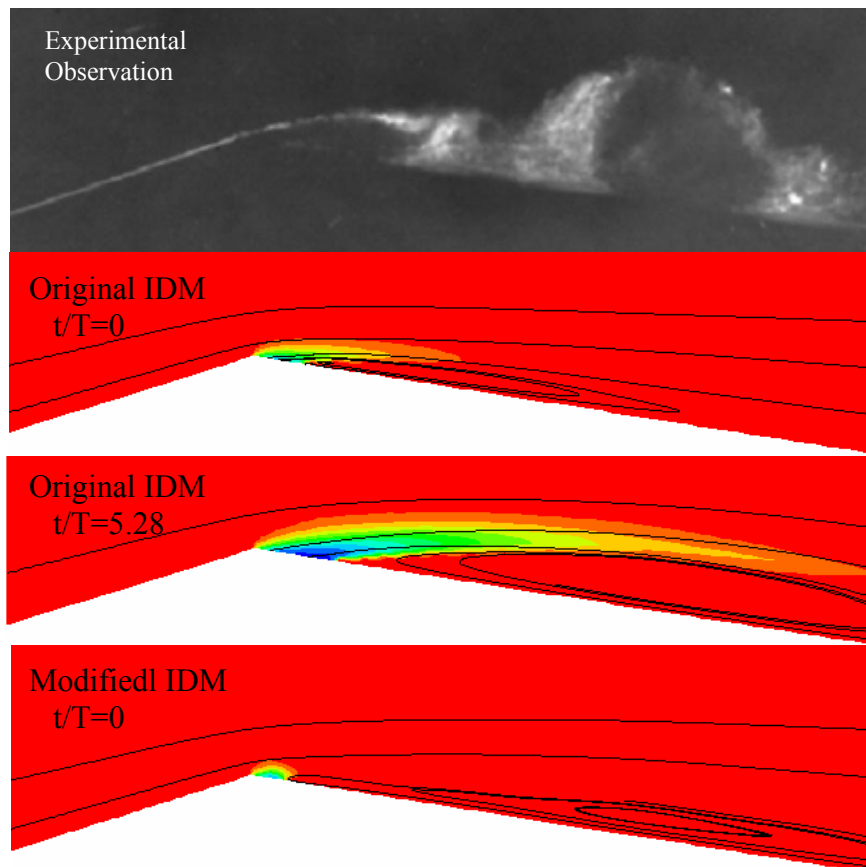


Figure 5-17. Cavity shape and recirculation zone during cycling of original and modified IDM. The experimental observation is adopted from Stutz and Rebound (1997, 2000)

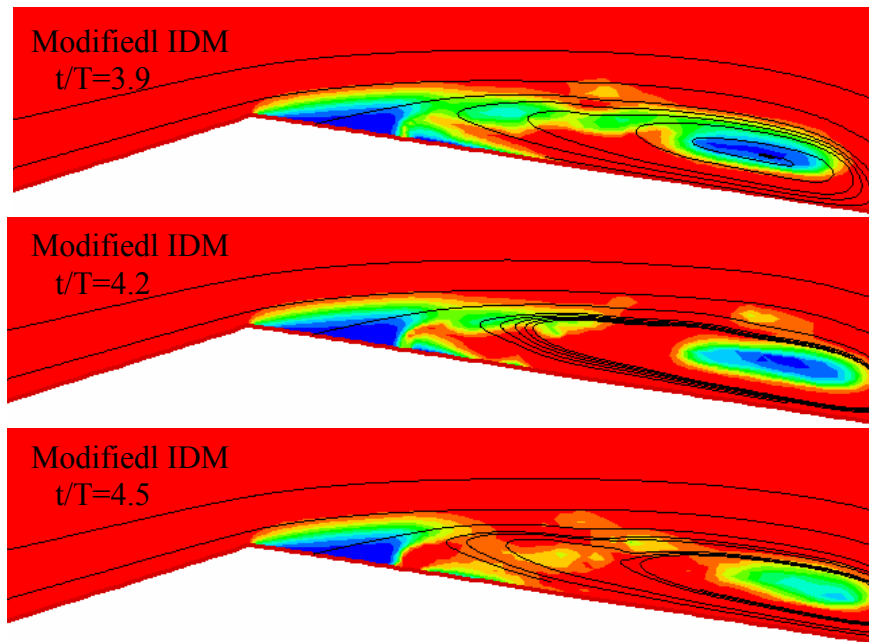


Figure 5-17. Continued

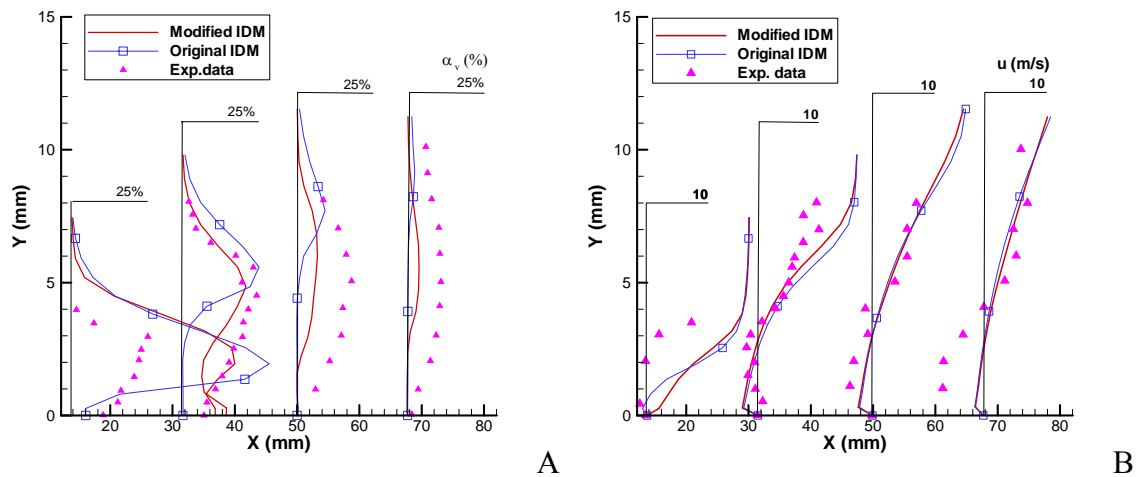


Figure 5-18. Time-averaged volume fraction and velocity comparisons of original and modified IDM. The vertical scale is the distance from the wall. Experimental data are from Stutz and Reboud (1997, 2000). A) Vapor volume fraction. B) u-velocity

5.3 Turbulent Cavitating Flow over a Clark-Y Hydrofoil

The capability of the modified IDM (Section 3.3) and turbulence models are further investigated in unsteady cavitating flows over a Clark-Y hydrofoil, assessed by experimental data from Wang et al. (2001). To facilitate the performance evaluation, the

generalized treatments of the SoS-2, including SoS-2, SoS-2A described in Section 4.3, are coupled.

For the computational set-up (Figure 5-19A), the computational domain and boundary conditions are given according to the experimental set-up. The Clark-Y hydrofoil is located at the water tunnel center. Two angles-of-attack (AoA) considered are 5° and 8° . The hydrofoil chord length is c and the hydrofoil leading edge is $3c$ away from the inlet. The two important parameters are the Reynolds number and the cavitation number, which is based on inlet pressure P_∞ and vapor pressure P_v with inlet velocity U_∞ .

$$\text{Re} = \frac{U_\infty c}{\nu} = 7 \times 10^5 \quad (5.2)$$

$$\sigma = \frac{P_\infty - P_v}{\rho U_\infty^2 / 2} \quad (5.3)$$

The filter size in the present study is chosen to be larger than the largest grid scale employed in the computation, and is set to be $\Delta = 0.08c$.

Computations have been done for two AoA and several cavitation numbers. Specifically, for AoA= 5° under four flow regimes: no-cavitation ($\sigma = 2.02$), inception ($\sigma = 1.12$), sheet cavitation ($\sigma = 0.92$), and cloud cavitation ($\sigma = 0.55$), and AoA= 8° under three cavitation numbers: no-cavitation ($\sigma = 2.50$), sheet cavitation ($\sigma = 1.40$), cloud cavitation ($\sigma = 0.80$). All cases above are at the same Reynolds number $\text{Re} = 7 \times 10^5$.

Two different turbulence models, LSM and FBM, have been employed to help probe the characteristics of cavitation and turbulence modeling interactions, coupled with

different SoS numerical models. The outlet pressure is fixed and adjustment of the vapor pressure is needed to be consistent with the prescribed cavitation number in each case.

Grid sensitivity analysis. To investigate the grid dependency, two grids are adopted in the computation: coarse grid and fine grid. The grid blocks and numbers of the coarse grid are shown in Figure 5-19B. The fine grid has 60% more number of nodes than that of the coarse grid in the vertical direction while maintaining the same distribution in the horizontal direction. Two different cavitation numbers, $\sigma = 2.02$ and $\sigma = 0.55$, both at $\text{AoA}=5^\circ$ have been investigated. Overall, the solutions on both grids are in good agreement. The time-averaged u-velocity and v-velocity profiles with $\sigma = 2.02$ and $\sigma = 0.55$ using the LSM are shown in Figure 5-20. The results based on the FBM are of similar nature and will not be repeated.

Hereafter, to reduce the cost of time-dependent computations, we use the coarse grid in the computations.

Visualization of cavity and flow field. First, we focus on the LSM results to analyze the performance of the IDM. Figure 5-21 and Figure 5-22 show the time-averaged flow structure and cavity shape under varied cavitation numbers. With no cavitation, the flow field is attached without separation for both $\text{AoA}=5^\circ$ and $\text{AoA}=8^\circ$ (Figure 5-21A left column and Figure 5-22A left column). This is consistent with the experimental observation. When cavitation appears, the density will change by a factor of 1000 between liquid and vapor phases. Consequently, there is a drastic reduction in the amount of mass inside the cavity, and a contraction of the fluid flow behind the cavity. With the reduction of the cavitation number, the cavity and recirculation zone become bigger. At cloud cavitation regime, the cavity experiences shedding, causing multiple

recirculating flows (Figure 5-21D left column and Figure 5-22C left column). Compared to the experimental data for both AoAs (Table 5-4 and Table 5-5), the predicted cavity sizes demonstrate qualitatively consistent rendering, albeit generally over-predicted. For incipient cavitation, the experiment observed the recurring formation of hair-pin type cavitating vortex structures, which are not attached to the solid surface (Wang et al. 2001). This type of flow structure is not captured in the computation. The time-averaged flow structures associated with sheet and cloud cavitation, on the other hand, seem to be reasonably captured computationally. Furthermore, the time-averaged outcome of employing both LSM and FBM seems compatible.

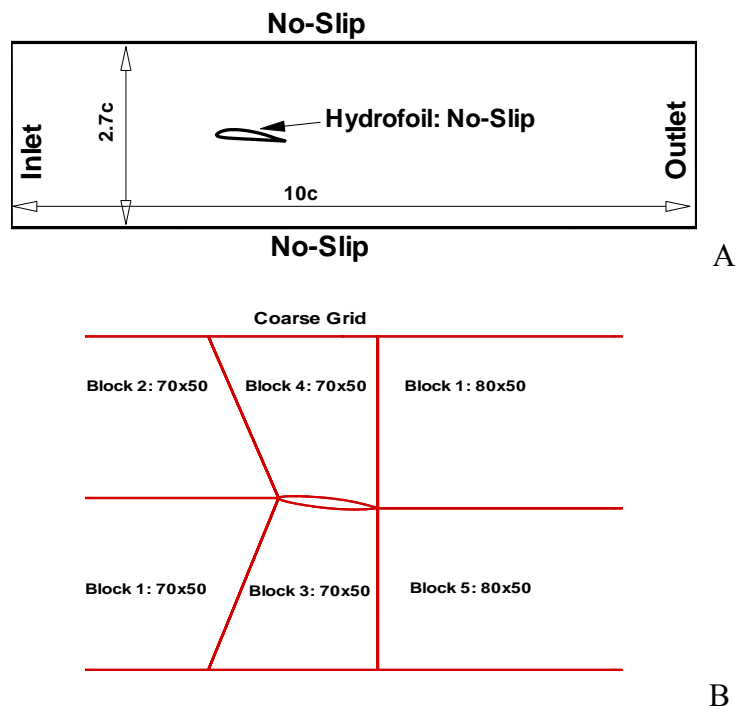


Figure 5-19. Clark-Y geometry sketch and Grid blocks. A) Geometry configuration and boundary conditions, c is the hydrofoil chord. B) Grid blocks and coarse grid numbers

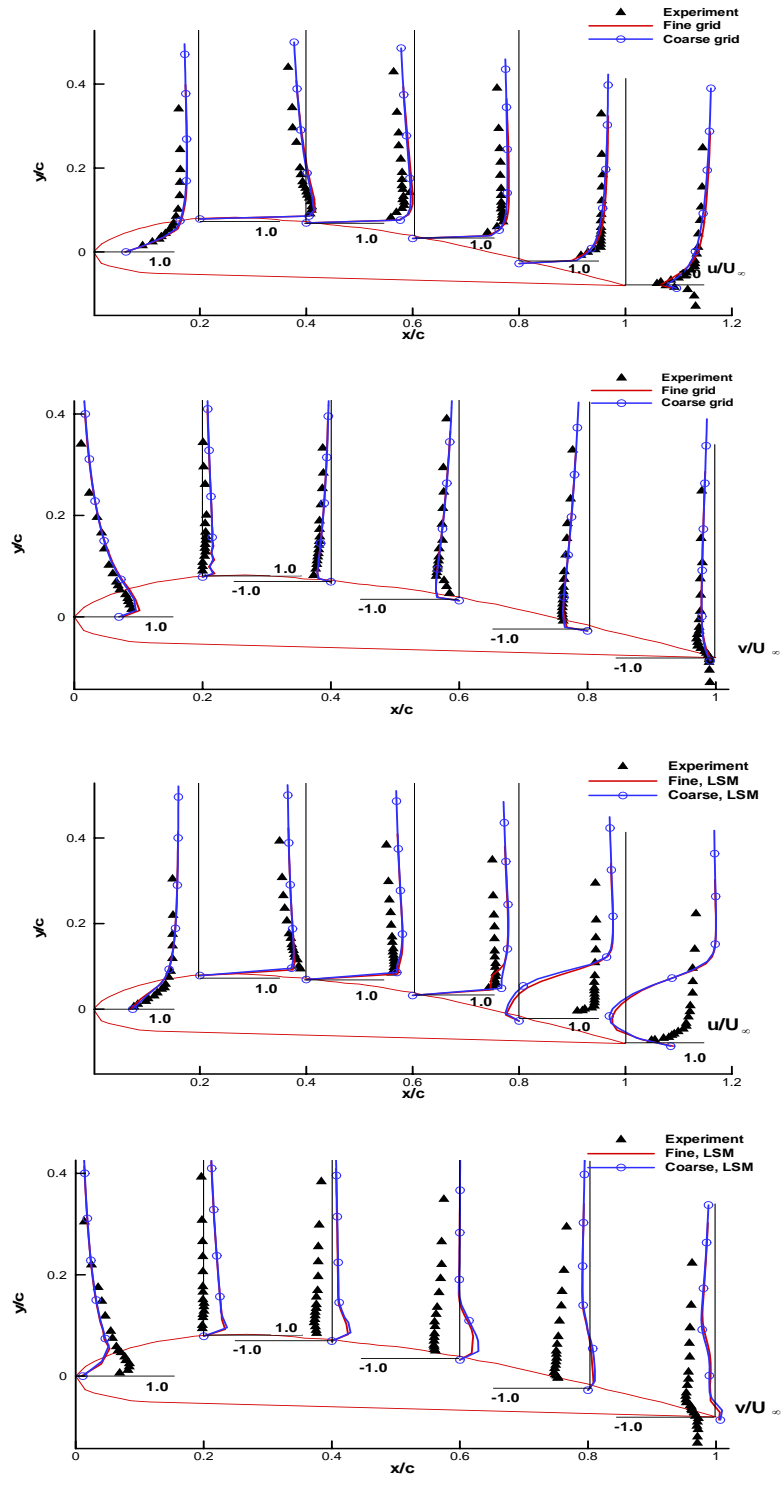


Figure 5-20. Grid sensitivity of the time-averaged u - and v -velocity, LSM, $AoA=5^\circ$. Experimental data are from Wang et al. (2001). A) No-cavitation. B) Cloud cavitation $\sigma = 0.55$

Table 5-4. Time-averaged cavity leading and trailing positions of different turbulence models (Taking $\alpha_l = 0.95$ as cavity boundary), modified IDM with SoS-2A, AOA=5 degrees

Position	Inception $\sigma = 1.12$			Sheet cavitation $\sigma = 0.92$			Cloud cavitation $\sigma = 0.55$		
	LSM	FBM	Exp.	LSM	FBM	Exp.	LSM	FBM	Exp.
Leading	0.13	0.13	-	0.13	0.13	0.23	0.16	0.17	0.22
Trailing	0.62	0.57	-	0.64	0.64	0.68	1.01	1.04	0.90

Table 5-5. Time-averaged cavity leading and trailing positions of different turbulence models (Taking $\alpha_l = 0.95$ as cavity boundary), modified IDM with SoS-2A, AoA=8 degrees.

Position	Sheet cavitation $\sigma = 1.40$			Cloud cavitation $\sigma = 0.80$		
	LSM	FBM	Exp.	LSM	FBM	Exp.
Leading	0.094	0.098	0.15	0.12	0.13	0.15
Trailing	0.53	0.52	0.56	1.07	1.10	0.84

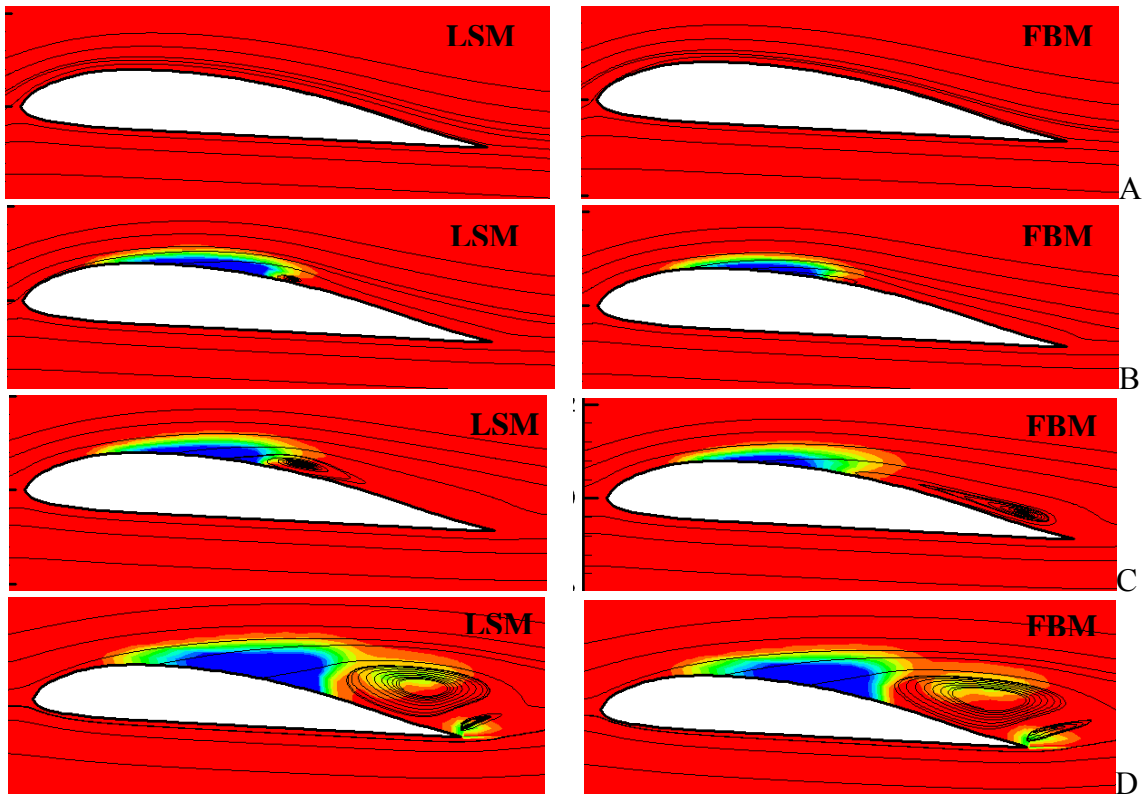


Figure 5-21. Time-averaged volume fraction contours and streamlines of different turbulence models, AoA=5°. A) No-cavitation. B) Incipient cavitation. C) Sheet Cavitation $\sigma = 0.92$. D) Cloud cavitation $\sigma = 0.55$

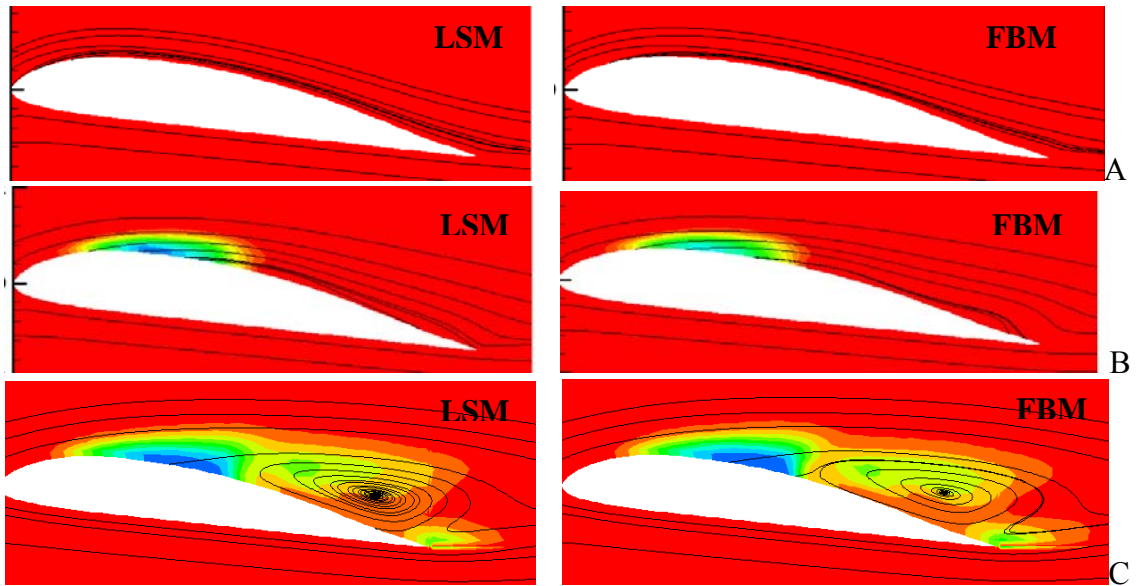


Figure 5-22. Time-averaged volume fraction contours and streamlines of different turbulence models, $\text{AoA}=8^\circ$. A) No-cavitation. B) Sheet cavitation $\sigma = 1.40$. C) Cloud cavitation $\sigma = 0.80$

The temporal evolution of the computed and experimentally observed flow structures with cloud cavitation, under two AoAs, are shown in Figure 5-23 and Figure 5-24. Figure 5-23A left column shows the time sequences of flow structures predicted by LSM at $\text{AoA}=5^\circ$. The corresponding flow predicted by the FBM is shown in the right column. The experimental visual image is shown in Figure 5-23B. The flow structures at $\text{AoA}=8^\circ$ are shown in Figure 5-24. Both the computations and the experiment indicate that as the AoA increases, the cavity exhibits a more pronounced recurrence of the size variation. The FBM predicts stronger time-dependency than the LSM. We will further investigate this aspect in the following discussion. To help elucidate the main features of the cavity dynamics from both numerical and experimental studies, we show in Figure 5-25 three stages of the cavity sizes, for cloud cavitation $\sigma = 0.55$ at $\text{AoA}=8^\circ$. The figure demonstrates that the numerical simulation is capable of capturing the initiation of the cavity, growth toward trailing edge, and subsequent shedding, in accordance with the qualitative features observed experimentally.

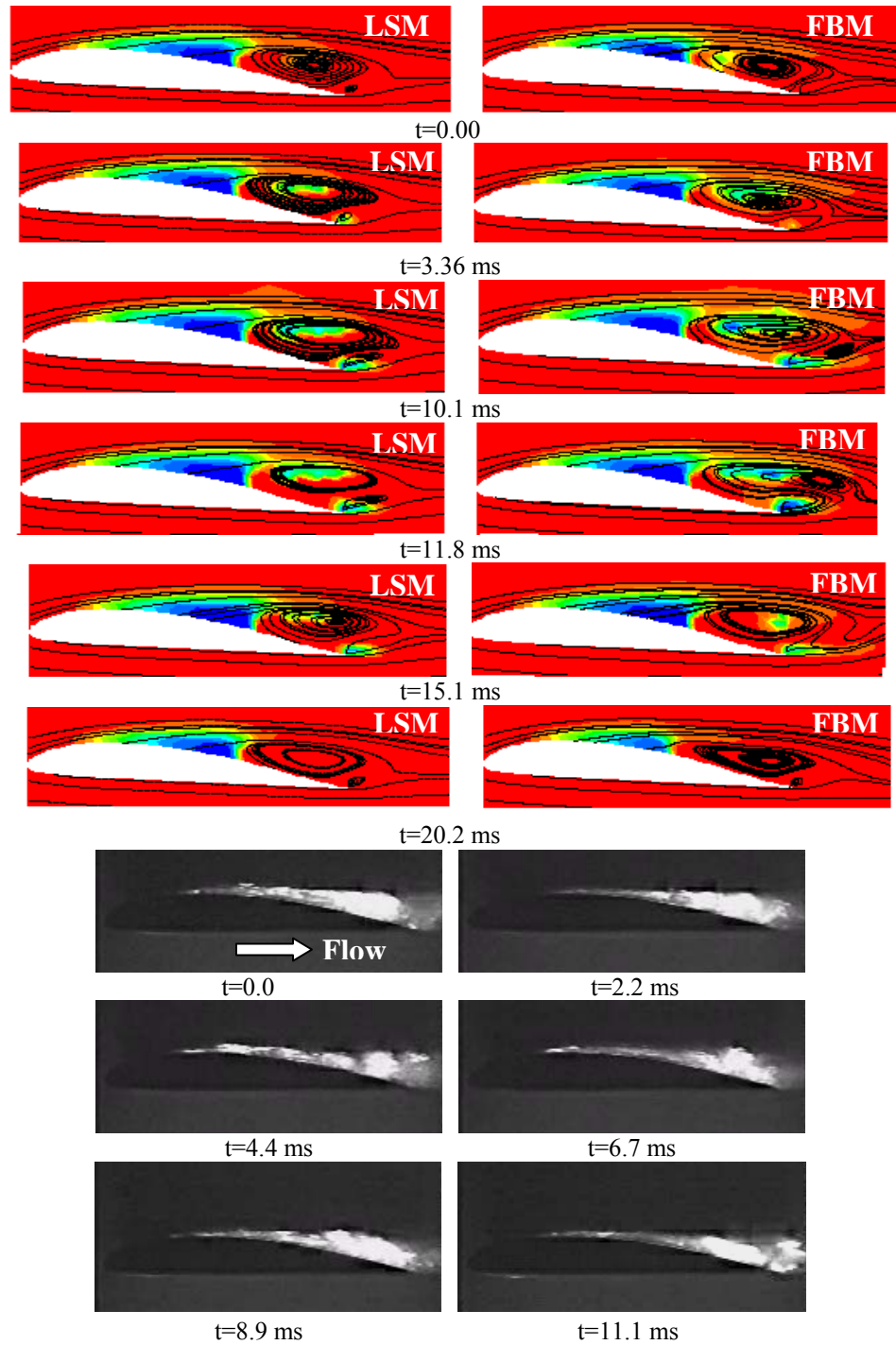


Figure 5-23. Time evolutions of cloud cavitation $\sigma = 0.55$, $AoA=5^\circ$. A) Numerical results of different turbulence models. B) Side views of the experimental visuals from Wang et al. (2001)

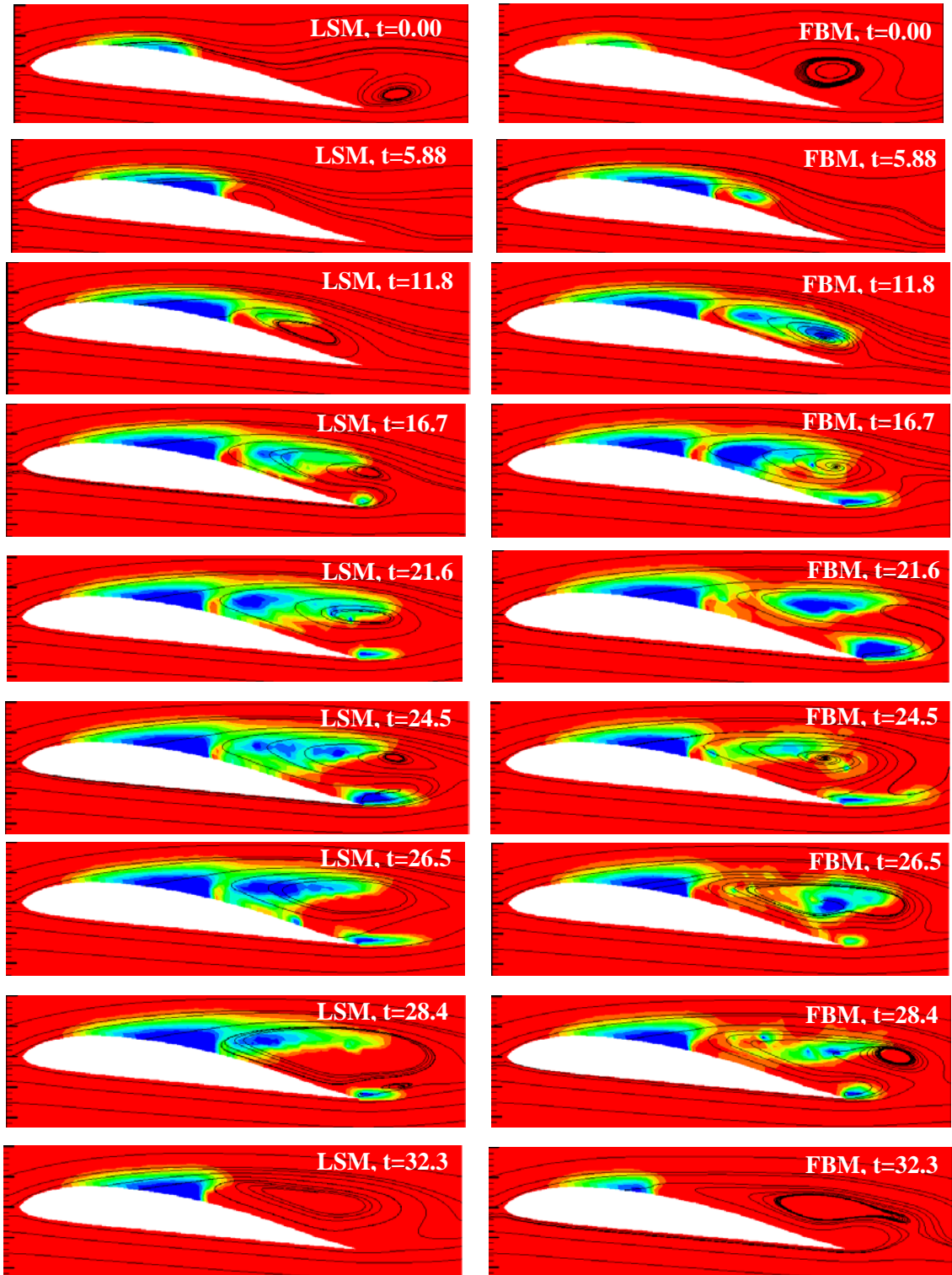


Figure 5-24. Time evolutions of cloud cavitation $\sigma = 0.80$, $\text{AoA} = 8^\circ$. A) Numerical results of different turbulence models. B) Side views of the experiment visuals from Wang et al. (2001)

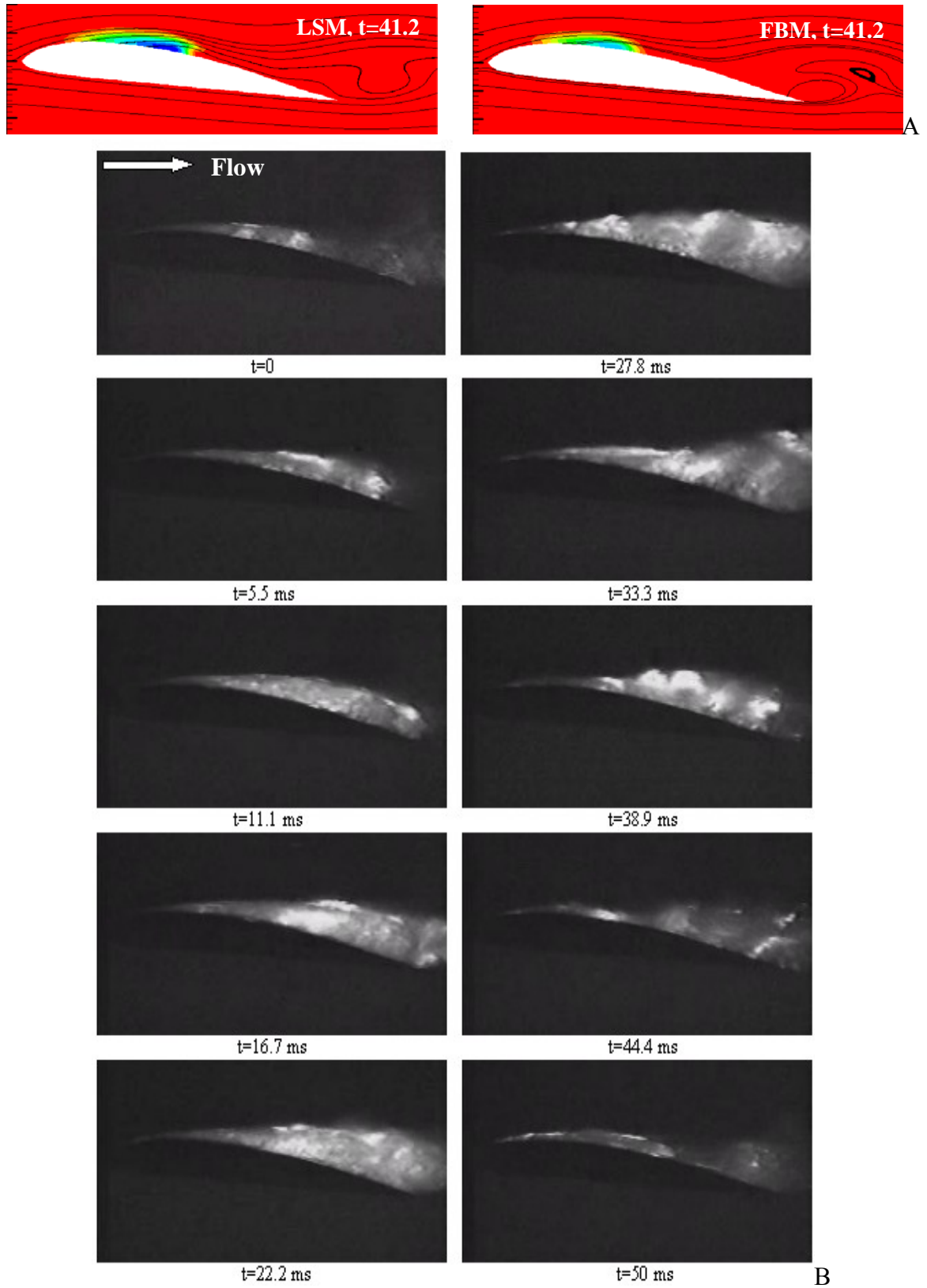


Figure 5-24. Continued

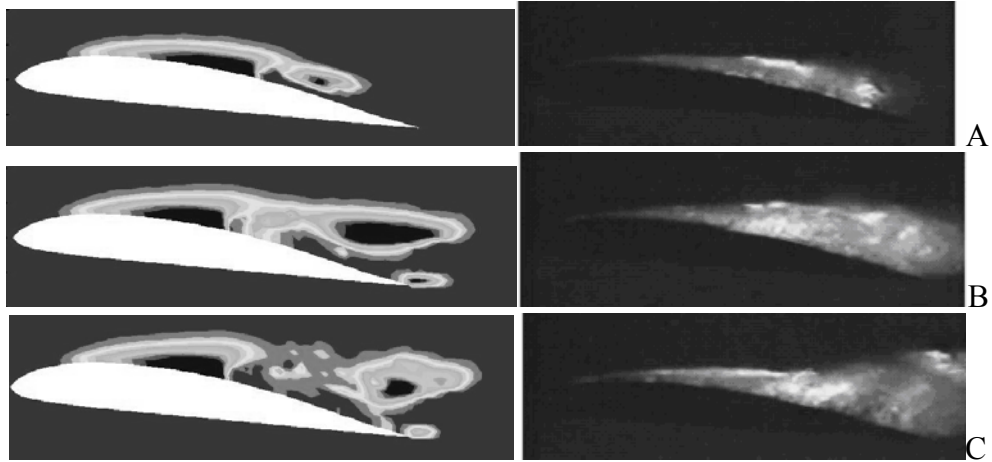
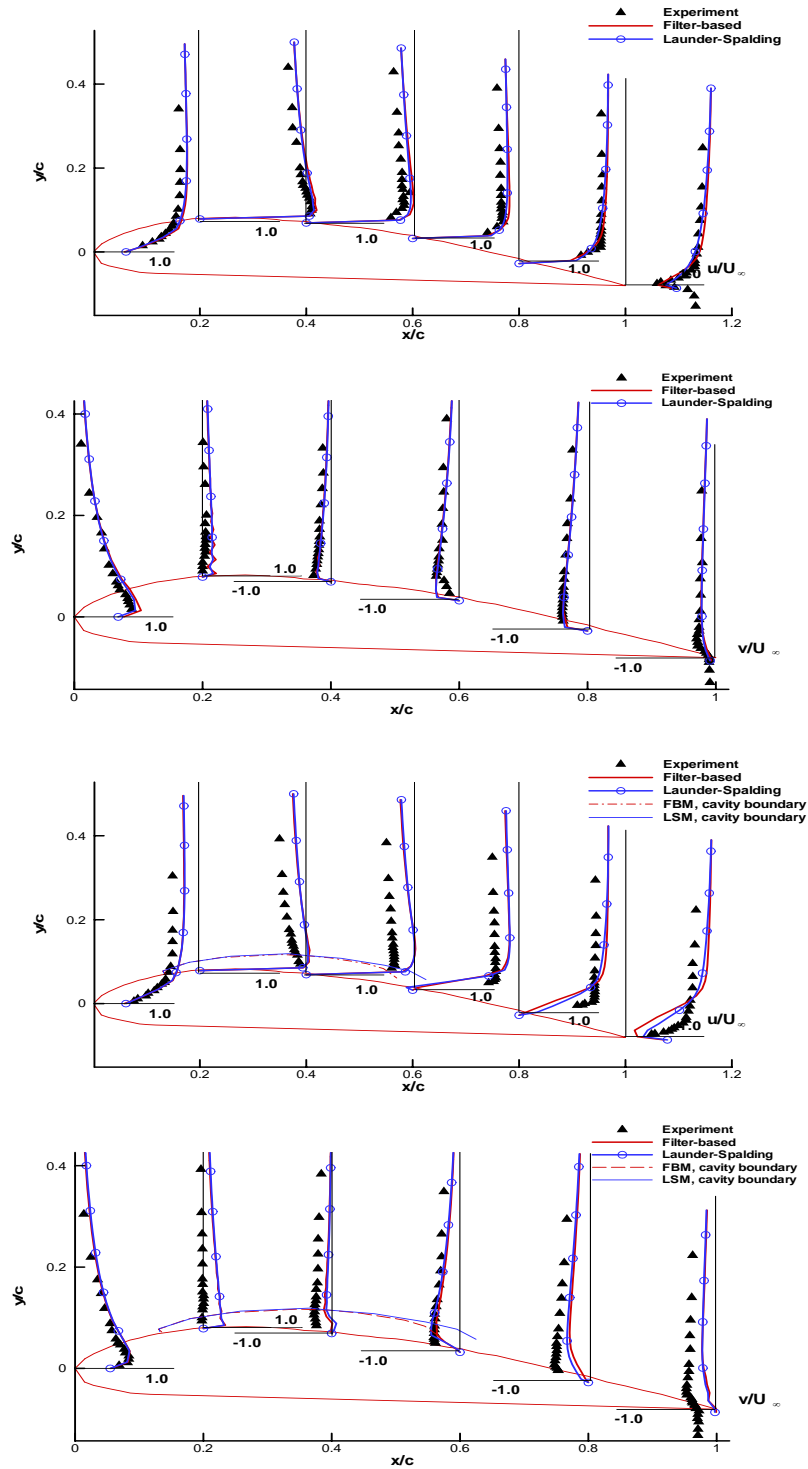


Figure 5-25 Cavity stage comparisons, cloud cavitation $\sigma = 0.80$, $\text{AoA}=8^\circ$: FBM (Left) and Experiment (Right)^o. Experimental visuals are from Wang et al. (2001). A) Early stage: cavity formation. B) Second stage: cavity growth toward trailing edge. C) Third stage: cavity break-up and shedding

Velocity profiles and lift/drag coefficients. The mean horizontal u -velocity and vertical v -velocity of the flow field are illustrated in Figure 5-26 ($\text{AoA}=5^\circ$) to Figure 5-27 ($\text{AoA}=8^\circ$). The time-averaged velocity profiles are documented at 6 chordwise locations, 0%, 20%, 40%, 60%, 80%, and 100% of the leading edge, under different cavitation numbers. With no cavitation, the numerical results agree well with the experiment, and the results of the two turbulence models are virtually identical (Figure 5-26A and Figure 5-27A). With the cavitation number decreasing, the differences between prediction and measurement become more substantial, especially at the cavity closure region. In fact, recirculation breaks up the cavity and tilts the rear portion of the cavity more upward, which makes the cavity thicker in comparison to the experiment. With the reduction in cavitation number, it becomes more distinguished in Figure 5-23 and Figure 5-24. The cavity tilt-up results in over-shooting the u -velocity at the closure region (0.8c and 1.0c sections) (Figure 5-26 and Figure 5-27). Overall, considering the difficulties in experimental measurement (Wang et al. 2001) the agreement is reasonable.



A

B

Figure 5-26. Time-averaged u- and v-velocities of two turbulence models, $\text{AoA} = 5^\circ$. Experimental data are from Wang et al. (2001). A) no-cavitation. B) Inception $\sigma = 1.12$. C) Sheet cavitation $\sigma = 0.92$. D) Cloud cavitation $\sigma = 0.55$

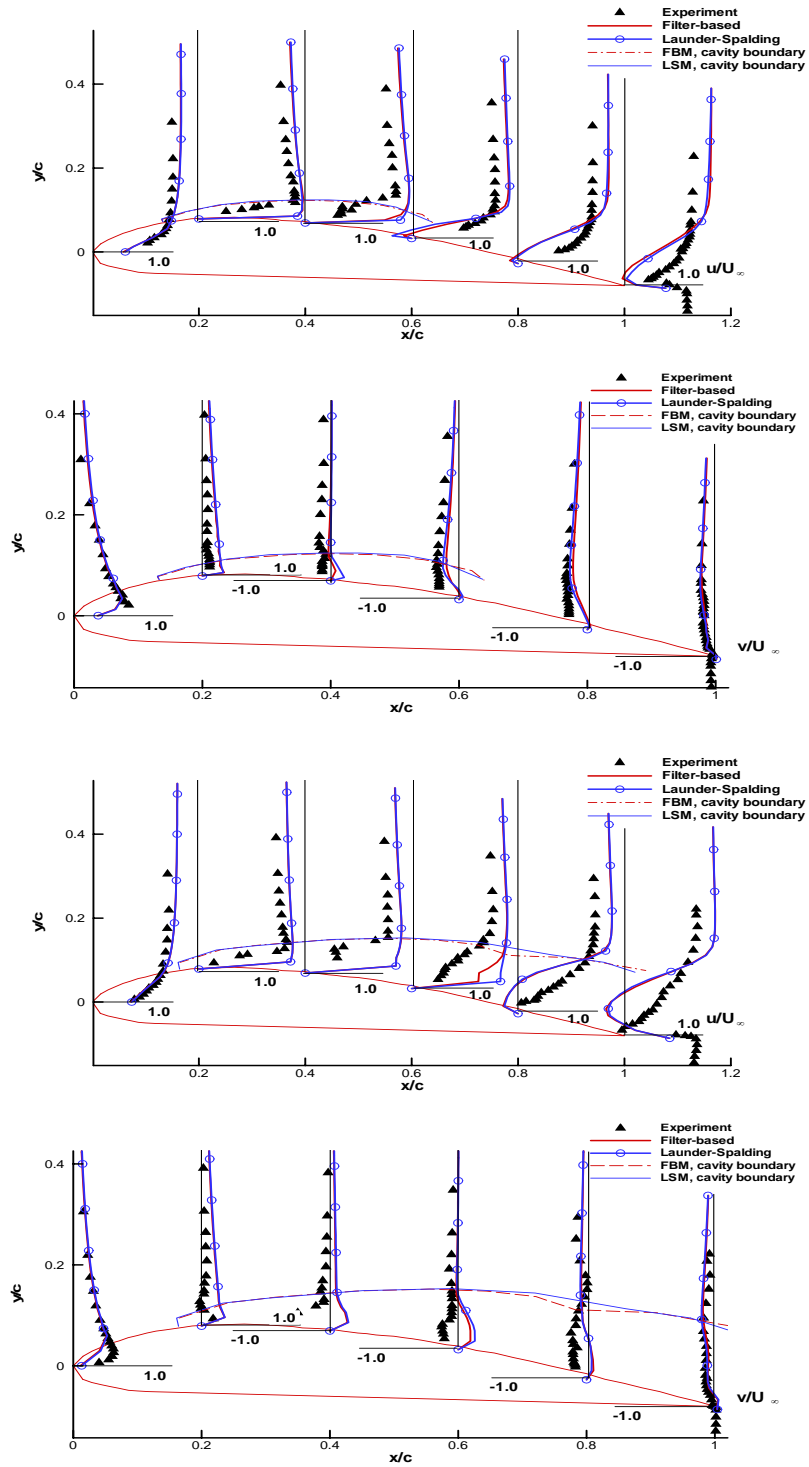


Figure 5-26. Continued

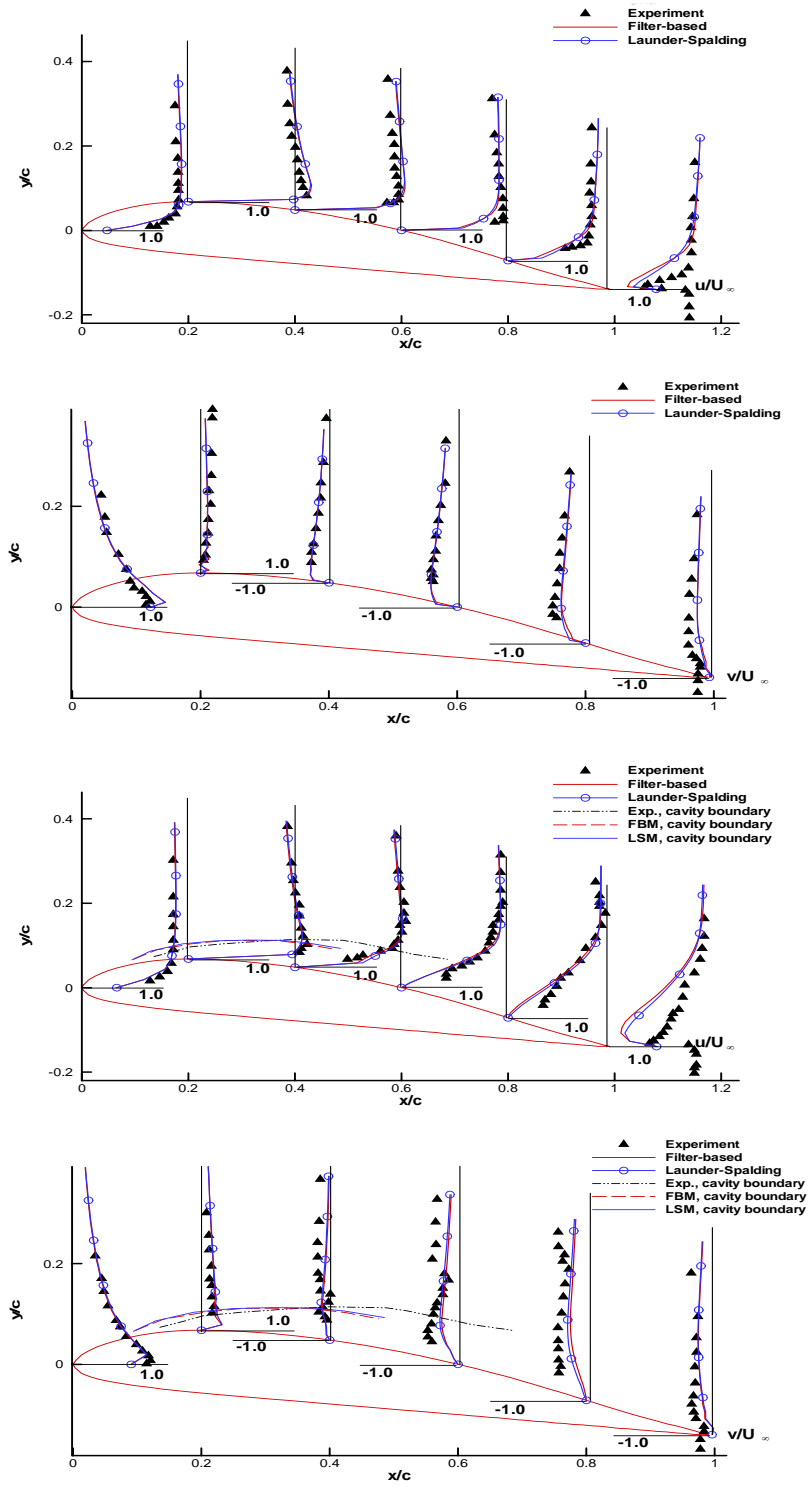


Figure 5-27. Time-averaged u - and v -velocities of two turbulence models, $AoA=8^\circ$. Experimental data are from Wang et al. (2001). A) No-cavitation. B) Sheet cavitation $\sigma=1.40$. C) Cloud cavitation $\sigma=0.80$

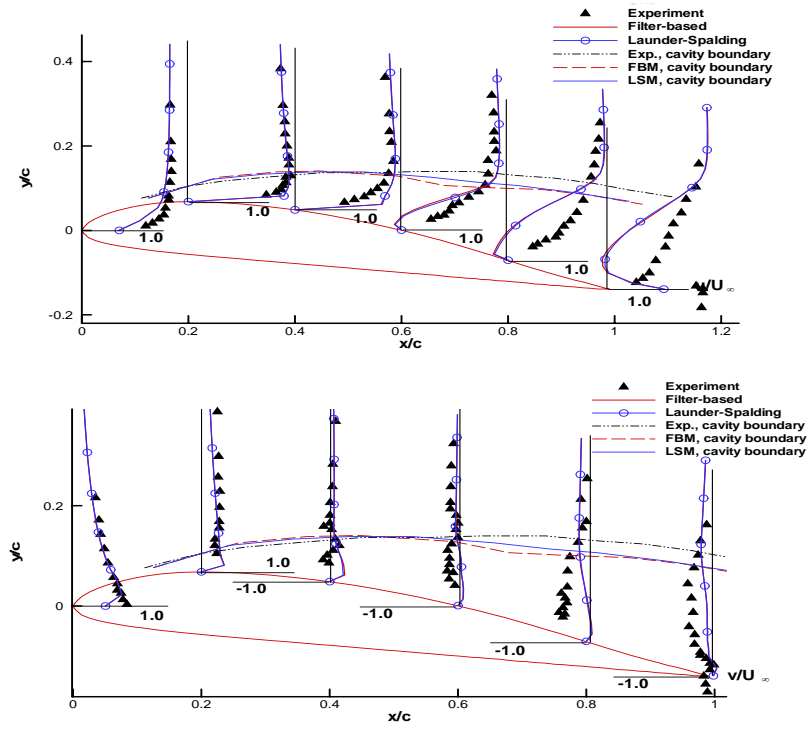


Figure 5-27. Continued

Figure 5-28 shows the time-averaged lift and drag coefficients collected from experiments and computations. The computational models estimate that as cavitation appears, lift decreases. However, experimentally, such a drop doesn't take place until the sheet cavitation regime. For sheet and cloud cavitation, both computations and experiment show consistent trends, namely, marked reduction in lift as the cavitation becomes more pronounced. From the time-averaged flow structures shown earlier, one clearly sees that the cavity changes the effective shape of the hydrofoil, causing flow to separate. Hence, the reduction in lift is expected. Regarding the drag coefficient, there is a marked increase from sheet to cloud cavitation, which is reflected by the computational models. Overall, the lift coefficient is under-predicted and the drag coefficient is over-predicted by both turbulence models, but the trends are reasonably captured in the sheet and cloud cavitation regimes.

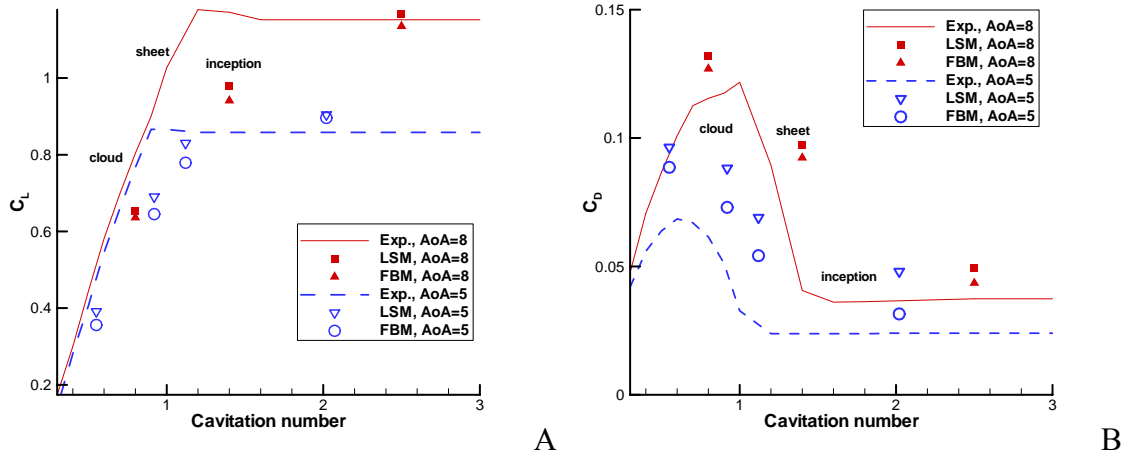


Figure 5-28. Time-averaged lift and drag coefficients comparisons. Experimental data are from Wang et al. (2001). A) Lift C_L . B) Drag C_D

Assessing modified IDM parameters. To better understand the IDM performance, we examine the condensation \dot{m}^+ and evaporation \dot{m}^- source terms. A TEM cavitation model heuristically developed by Merkle et al. (1998) and extensively applied by Ahuja et al. (2001) shows identical model equations to the source terms given as

$$\dot{m}^- = \frac{C_{dest} \rho_L \alpha_L \text{Min}(0, p - p_V)}{\rho_V (\rho_L U_\infty^2 / 2) t_\infty}$$

$$\dot{m}^+ = \frac{C_{prod} (1 - \alpha_L) \text{Max}(0, p - p_V)}{(\rho_L U_\infty^2 / 2) t_\infty}$$

In the published applications (Merkle et al. 1998) $C_{dest} = 1.0$ and $C_{prod} = 80$ are often adopted. To compare the IDM with Merkle et al.'s model, we can rearrange the source term in IDM (in Section 3.2.2) following the above equation format, and get the equivalent model parameters C'_{dest} and C'_{prod} as

$$C'_{dest} = C'_{prod} = \frac{0.5 \rho_L U_\infty^2}{(\rho_L - \rho_V) (V_{I,n}^{net})^2}$$

Using the solutions obtained at AoA=5° presented in Figure 5-21 and Figure 5-22, we have the following observations

- With the decrease of the cavitation number from no-cavitation to cloud cavitation, C'_{dest} / C_{dest} varies from O(10) to O(100), and C'_{prod} / C_{prod} varies from O(1) to O(10), exhibiting substantial variations in accordance with the cavitation regimes.
- For a given cavitating flow regime, the variation of ratios C'_{dest} / C_{dest} and C'_{prod} / C_{prod} for time-averaged results is not much along a constant volume fraction contour. Approximately, they can be considered as unchanged.
- The values of C'_{dest} and C'_{prod} experience temporal variations in each cavitation regime. The ratio of $C'_{dest_max} / C'_{dest_min}$ tends to be O(1)~O(10) at the same location inside the cavity, with C'_{dest_max} denoting the value at maximum cavity size and C'_{dest_min} at minimum cavity size. The investigation on the FBM results shows that the C'_{dest} (C'_{prod}) has larger temporal fluctuation than the LSM between the maximum and minimum cavity sizes.

Venkateswaran et al. (2002) stated that the choice of C_{dest} and C_{prod} for steady computations is not critical. However, the same apparently doesn't hold for time-dependent computations.

Comparison of turbulence models. To assess the turbulence models' performance, we compare the results of the LSM and FBM in each matching cavitation flow regime. For no-cavitation, the LSM and FBM exhibit very close time-averaged solutions. As the cavitation number is reduced, the difference becomes more noticeable. With cavitation, the FBM results give a larger wake, especially for sheet cavitation (comparing the Left and Right columns in Figure 5-21 and Figure 5-22). Nevertheless, the performance of both turbulence models is largely consistent.

The difference between the FBM and LSM can be illustrated more clearly by the time-dependent results. As already discussed, for cloud cavitation, the cavity breakup phenomenon is more noticeable using the FBM than using the LSM in the cavity time evolutions, and FBM has a larger secondary cavity at the hydrofoil tailing tip which may

induce the re-entrance effect (Figure 5-23 and Figure 5-24). In Figure 5-29, we further compare the time-averaged eddy viscosity distributions yielded by both turbulence models, with different cavitation numbers at $\text{AoA}=5^\circ$. With both turbulence models, we observe that the eddy viscosity decreases as the cavitation becomes more pronounced and fluctuating in time. Furthermore, the eddy viscosity increases in the recirculation region. It is also clear that the LSM yields consistently higher eddy viscosity, resulting in reduced unsteadiness of the computed flow field.

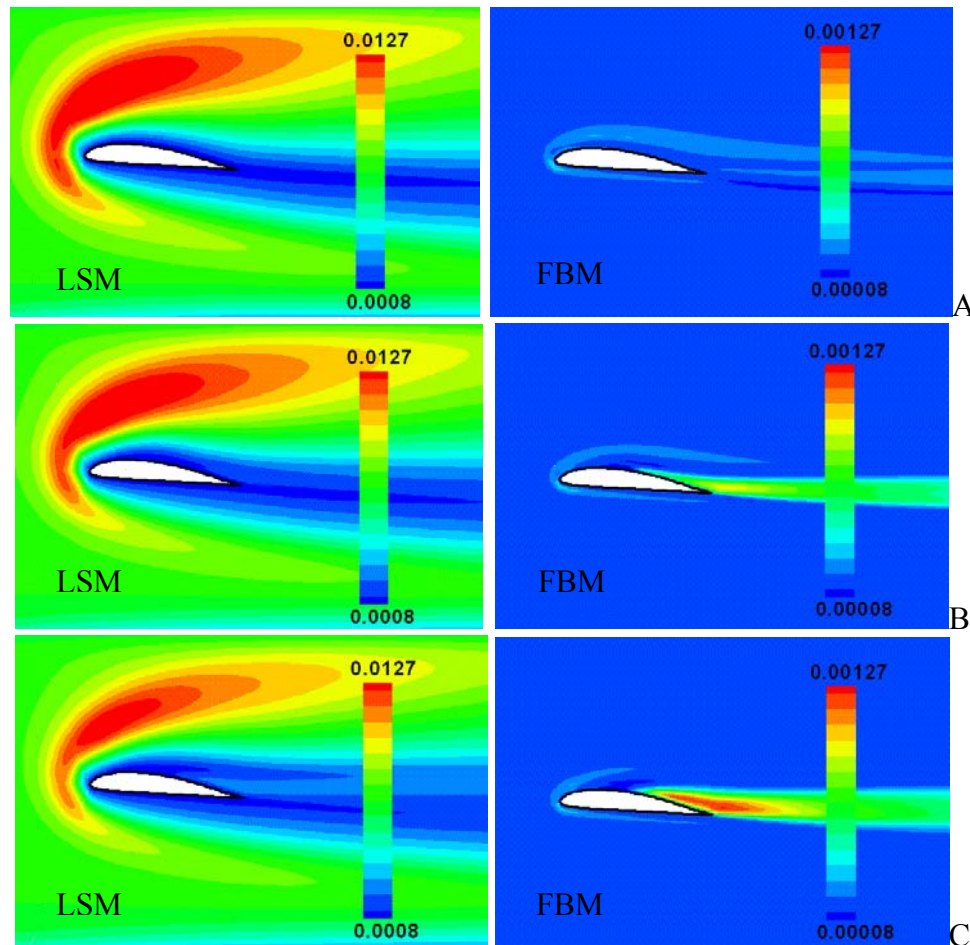


Figure 5-29. Time-averaged viscosity contours, $\text{AoA}=5^\circ$. A) No-cavitation. B) Inception $\sigma = 1.12$. C) Sheet cavitation $\sigma = 0.92$. D) Cloud cavitation $\sigma = 0.55$

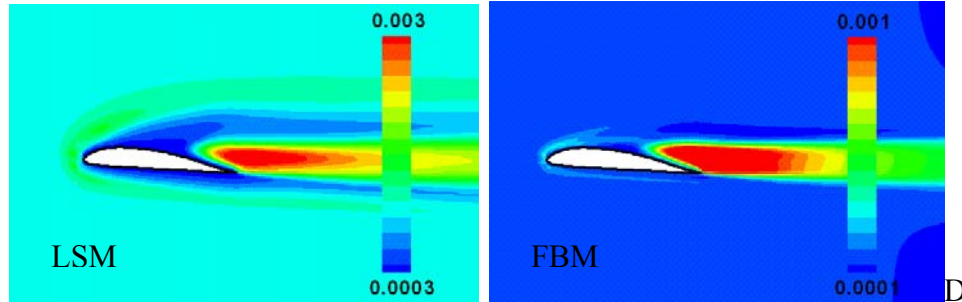


Figure 5-29. Continued

Comparison of Speed-of-Sound models. The time-averaged C_L and C_D predicted with different speed-of-sound treatments, including SoS-2 and SoS-2A (Section 4.3), are summarized in Table 5-6. It seems that the SoS-2A can marginally improve the aerodynamic predictions for two different cavitation models, the modified and heuristic cavitation models (HM) (Section 3.3). The time-average u-velocity profiles by SoS-2 and SoS-2A using modified IDM are shown in Figure 5-30 with little difference.

Table 5-6 Comparison of mean C_L and C_D , LSM, Cloud cavitation $\sigma = 0.80$, AoA=8 degrees (Taking $\alpha_L = 0.95$ as cavity boundary)

Cavitation model	IDM, LSM		HM, LSM		Exp.
	SoS-2	SoS-2A	SoS-2	SoS-2A	
C_L	0.643	0.665	0.682	0.681	0.804
C_D	0.130	0.128	0.132	0.131	0.116

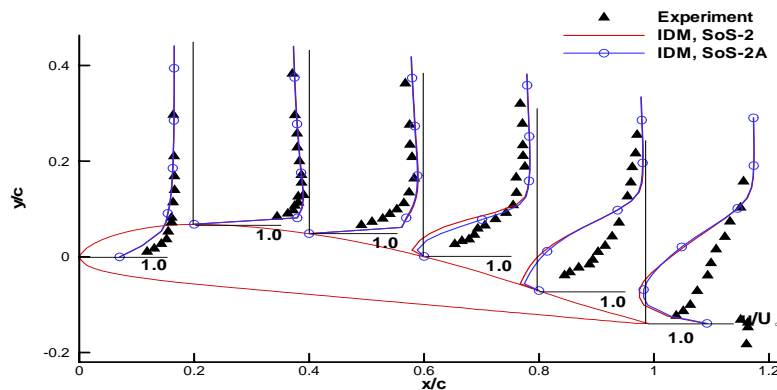


Figure 5-30. Time-averaged u-velocity of different SoS treatments, cloud cavitation $\sigma = 0.80$, AoA=8°. Experimental data are from Wang et al. (2001)

CHAPTER 6 CONCLUSIONS AND FUTURE RESEACH

6.1 Conclusions of Present Research

The Favre-averaged Navier-Stokes equations, along with the turbulence closure and transport equation-based cavitation model, are employed in turbulent cavitating flow computations. To ensure stability and convergence with good efficiency and accuracy, the pressure-based PISO algorithm is presented for time-dependent computations. The cavitation and turbulence models are assessed by both steady and unsteady simulations in various configurations, including cylinder, hydrofoils, convergent-divergent nozzle, and hollow-jet valve.

In the context of turbulence modeling strategy, a filter-based model (FBM) for turbulence closure is presented for time-dependent computations. Based on an imposed filter, conditional averaging is adopted for the Navier-Stokes equation to introduce one more parameter into the definition of the eddy viscosity. The filter can be decoupled from the grid, making it possible to obtain grid-independent solutions with a given filter scale. The FBM is implemented in the time-dependent single-phase flow over a square cylinder. It can effectively modulate the eddy viscosity, and produces much better resolution in capturing the unsteady features than the original Launder-Spalding model (LSM). The results agree well with experimental data except for an over-predicted Strouhal number. Also, the FBM shows compatibility with the LSM by changing the filter size. Subsequently, the FBM is applied to cavitating flows. It can significantly reduce the eddy

viscosity and generate much stronger time-dependency other than the LSM, which can damp out the oscillation and shedding.

In the context of the cavitation modeling strategy, the various recently developed transport equation-based cavitation models demonstrate comparable pressure distributions in steady-state computations. However, they exhibit substantial variations for time-dependent computations. To gain more insight into the compressibility of the mixture regarding the local Mach number, the two different approximations of speed-of-sound (SoS), namely, SoS-1 and SoS-2, are further investigated in the time-dependent cavitating flows over a hollow-jet valve. The different treatments have significant impact on the unsteady dynamics. Both are similar at the region close to the pure liquid phase and theoretically agree with rational analysis. But the linear approximation of the SoS-1 deviates from the theoretical analysis at the region close to the gas phase. The analysis reveals that the SoS-1 is weak in pressure-density correlation, and the SoS-2 demonstrates a stronger pressure-density correlation in the cavitation vicinity. Therefore, SoS-2 is better than SoS-1 from this point of view. Furthermore, the generalization in terms of SoS-2 is introduced by averaging the local surrounding nodes. Generally, the SoS-2A predicts comparable result with SoS-2.

In the recently developed interfacial dynamics-based cavitation model (IDM), an empirical factor is used to construct the interfacial velocity in time-dependent computations, which links the interfacial velocity between phases to the local flow field velocity. This approach lacks generality because the interfacial velocity is a function of the phase change process. An enhanced approximation based on the net transformation between liquid- and vapor-phase is presented to reconstruct the interfacial velocity. The

modification can capture the cavity break-up phenomena, which is qualitatively similar to the experimental observations. By assessing lift and drag coefficients, pressure and velocity distributions covering a wide regime from inception to cloud cavitation, the new approximation can predict the major flow feature and reasonably agree with the experimental measurements.

Meanwhile, we observe that the time-averaged surface pressures give a reasonable estimate of mean lift and drag coefficients under various flow conditions. While, since the average effect can smooth out some important instantaneous feature, the time-averaged results alone are insufficient to assess turbulence model performance, with respect to flow physics such as wave propagation in particular.

6.2 Future Research Directions

The present research can be further extended in the following directions

- Investigating the FBM in 3-D for single phase computations over the cylinder to further investigate the effects on the Strouhal number.
- Adopting flexible filter function f for the filter-based model to handle the steep variation in grid spacing, to avoid the weak filtered effect at the fine grid regions since the model currently uses a constant filter size with the criterion of $\Delta \geq \max(\sqrt{\Delta x \cdot \Delta y})$ in the computations.
- Developing a more accurate estimate of the interfacial velocity for IDM.
- Combining the technique developed in the present study with suitable cryogenic modeling and numerical techniques, as developed in parallel by Utturkar et al. (2005), to handle issues arising from liquid rocket propulsion.

LIST OF REFERENCES

- Ahuja, V., Hosangadi, A. and Arunajatesan, S., 2001, "Simulations of Cavitating Flows Using Hybrid Unstructured Meshes," *J. Fluids Eng.*, vol. 123, pp. 331-340.
- Ahuja, V., Hosangadi, A. and Ungewitter, R.J., 2003, "Simulations of Cavitating Flows in Turbopumps," AIAA-2003-1261.
- Athavale, M.M and Singhal, A.K, 2001, "Numerical Analysis of Cavitating Flows in Rocket Turbopump Elements," AIAA-2001-3400.
- Baldwin, B.S. and Lomax, H., 1978, "Thin-Layer Approximation and Algebraic Model for Separated Turbulent Flow," AIAA 1978-257.
- Batchelor, G.K., 1967, *An Introduction to Fluid Dynamics*, Cambridge University Press, New York.
- Batten, P, Goldberg, U. and Chakravarthy, S., 2002, "LNS - an Approach towards Embedded LES," AIAA-2002-0427.
- Bosch, G. and Rodi, W., 1996, "Simulation of Vortex Shedding past a Square Cylinder near a Wall," *Int. J. Heat and Fluid Flow*, Vol. 17(3), pp. 267-275.
- Bosch, G. and Rodi, W., 1998, "Simulation of Vortex Shedding past a Square Cylinder with Different Turbulence Models," *Int. J. Numer. Meth. Fl.*, Vol. 28, pp. 601-616.
- Bradshaw, P., Ferriss, D.H. and Atwell, N.P., 1967, "Calculation of Boundary Layer Development Using the Turbulent Energy Equations, *J. Fluid Mech.*, Vol. 28(3), pp. 593-616.
- Bressloff, N.W., 2001, "A Parallel Pressure Implicit Splitting of Operator Algorithm Applied to Flows at All Speed," *Int. J. Numer. Meth. Fl.*, Vol. 36(5), pp. 497-518.
- Breuer, M., Jovicic N. and Mazaev K., 2003, "Comparison of DES, RANS and LES for the Separated Flow around a Flat Plate at High Incidence," *Int. J. Numer. Meth. Fl.*, Vol. 41, pp. 357-388.
- Coutier-Delgosha, O., Fortes-Patella, R. and Reboud, J.L., 2003, "Evaluation of the Turbulence Model Influence on the Numerical Simulations of Unsteady Cavitation," *J. Fluids Eng.*, Vol. 125, pp. 33-45.

- Coutier-Delgosha, O., Fortes-Patella, R., Reboud, J.L., Hakimi, N. and Hirsch, C., 2005, "Numerical Simulation of Cavitating Flow in 2D and 3D Inducer Geometries," *Int. J. Numer. Meth. Fl.*, Vol. 48, pp. 135-167.
- Delannoy, Y. and Kueny, J.L, 1990, "Two Phase Flow Approach in Unsteady Cavitation Modeling," *ASME Cavitation and Multiphase Forum*, Vol. 98, pp. 153-158.
- Duttweiler, M.E. and Brennen, C.E., 2002, "Surge Instability on a Cavitating Propeller," *J. Fluid Mech.*, Vol. 458, pp. 133-152.
- Favre, A., 1965, "Equations des Gaz Turbulents Compressibles," *J. de Mecanique*, Vol. 4, No. 3, pp. 361-390.
- Franc, J.P., Avellan, F., Belahadji, B., Billard, J.Y., Briancon, L., Marjollet, Frechou, D., Fruman, D. H., Karimi, A., Kueny, J.L. and Michel, J. M., 1995, *La Cavitation: Mecanismes Physiques et Aspects Industriels*, Presses Universitaires de Grenoble, Grenoble, France.
- Frank, R. and Rodi, W., 1993, "Calculation of Vortex Shedding past a Square Cylinder with Various Turbulence Models," *Turbulent Shear Flows 8*, (Durst et al., eds.), Springer, New York, pp. 189-204.
- Friedrichs, J. and Kosyna, G., 2002, "Rotating Cavitation in a Centrifugal Pump Impeller of Low Specific Speed," *J. Fluids Eng.*, Vol. 124, pp.356-362
- Gopalan, S. and Katz, J., 2000, "Flow Structure and Modeling Issues in the Closure Region of Attached Cavitation," *Physics of Fluids*, Vol. 12, pp. 895-911.
- Hanjalic, K., Launder, B.E. and Schiestel, R., 1980, "Multiple-Time-Scale Concepts in Turbulent Transport Modeling," *Proc. of Turbulent Shear Flows 2*, Springer, Berlin, pp. 36-49.
- Hosangadi, A., Ahuja, V. and Ungewitter, R.J., 2004, "Simulations of Cavitating Flows in Turbopumps," *J. Propulsion and Power*, Vol. 20 (4), pp. 604-611.
- Iaccarino, G., Ooi A., Durbin, P.A. and Behnia, M., 2003, "Reynolds averaged simulation of unsteady separated flow," *Int. J. of Heat and Fluid Flow*, Vol. 24, pp. 147-156.
- Issa, R.I., 1985, "Solution of the Implicitly Discretised Fluid Flow Equations by Operator-Splitting," *J. Comp. Physics*, Vol. 62, pp. 40-65.
- Johansen, S.T., Wu, J. and Shyy, W., 2004, "Filter-based unsteady RANS computations," *Int. J. Heat and Fluid Flow*, Vol. 25 (1), pp. 10-21.
- Kato, M. and Launder, B.E., 1993, "The Modeling of Turbulent Flow around Stationary and Vibrating Square Cylinders," *Proc. 9th Symposium on Turbulent Shear Flows*, Kyoto, Japan.

- Kawanami, Y., Kato, H., Tanimura, M. and Tagaya, Y., 1997, "Mechanism and Control of Cloud Cavitation," *J. Fluid Eng.*, Vol. 119, pp. 788-794.
- Kirschner, I.N., 2001, "Results of Selected Experiments Involving Supercavitating Flows," VKI Lecture Series on Supercavitating Flows, VKI Press, Brussels, Belgium.
- Knapp, R.T., Daily, J.W. and Hammit, F.G., 1970, *Cavitation*, McGraw-Hill, New York.
- Koutmos, P. and Mavridis, C., 1997, "A Computational Investigation of Unsteady Separated Flows," *Int. J. Heat and Fluid Flow*, Vol. 18, pp.297-306.
- Kosovic, B., 1997, "Subgrid-Scale Modeling for the Large-Eddy Simulation of High-Reynolds-Number Boundary Layers," *J. Fluid Mech.*, Vol. 336, pp. 151-182.
- Kunz, R.F., Boger, D.A., Stinebring, D.R., Chyczewski, T.S., Lindau, J.W., Gibeling, H.J., Venkateswaran, S. and Govindan, T.R., 2000, "A Pre-conditioned Navier-Stokes Method for Two-Phase Flows with Application to Cavitation Prediction," *Computers & Fluids*, vol. 29, pp. 849-875.
- Kunz, R.F., Lindau, J.W., Kaday, T.A. and Peltier, L.J., 2003, "Unsteady RANS and Detached Eddy Simulations of Cavitating Flow over a Hydrofoil," 5th Int. Symposium on Cavitation, Osaka, Japan, Cav03-OS-1-12.
- Lauder, B.E., Reece, G.J. and Rodi, W., 1975, "Progress in the Development of a Reynolds-Stress Turbulence Closure," *J. Fluid Mech.*, Vol. 68(3), pp. 537-566.
- Lauder, B.E. and Spalding, D.B., 1974, "The Numerical Computation of Turbulent Flows," *Comp. Meth. Appl. Mech Eng.*, Vol. 3, pp269-289
- Lecoffre, Y., 1999, *Cavitation Bubble Trackers*, A.A. Balkema, Brookfield, VT.
- Lee, S., Jung, K.H., Kim, K.H. and Bae, I.S, 2001a, "Analysis of Cavitation and Design of High-Pressure Pump Inducer," Proceedings of ASME FEDSM'01, ASME 2001 Fluids Engineering Division Summer Meeting, FEDSM2001-18161.
- Lee, S., Jung, K.H, Kim, J.H. and Kang, S.H., 2001b, "Cavitation Mode Analysis of Pump Inducer," In Press.
- Lyn, D.A., Einav, S., Rodi, W. and Park, J.H., 1995, "A Laser Doppler Velocimetry Study of Ensemble-Averaged Characteristic of the Turbulent Flow near Wake of a Square Cylinder," *J. Fluid Mech.*, Vol. 304, pp. 285-319.
- Lyn, D.A. and Rodi, W., 1994, "The Flapping Shear Layer Formed by Flow Separation from the forward Corner of a Square Cylinder," *J. Fluid Mech.*, Vol. 267, pp. 353-376.

- Mavridis, C., Bakrozis, A., Koutmos, P. and Papailiou, D., 1998, "Isothermal and Non-premixed Turbulent Reacting Wake Flows past a Two-Dimensional Square Cylinder," *Exp. Thermal and Fluid Sci.*, Vol. 17, pp. 90-99.
- Medvitz, R.B., Kunz, R.F., Boger, D.A., Lindau, J.W., Yocum, A.M. and Pauley, L.L., 2002, "Performance Analysis of Avitating Flow in Centrifugal Pumps Using Multiphase CFD," *J. Fluids Eng.*, Vol.124, pp. 377-383.
- Merkle, C.L, Feng, J. and Buelow, P.E.O., 1998, "Computational Modeling of the Dynamics of Sheet Cavitation," 3rd International Symposium on Cavitation, Grenoble, France.
- Moin, P., 2002, "Advances in Large Eddy Simulation Methodology for Complex Flows," *Int. J. Heat and Fluid Flow*, Vol. 23, pp. 710–720.
- Nagano, Y., Kondoh, M. and Shimada, M., 1997, "Multiple Time-Scale Turbulence Model for Wall and Homogeneous Shear Flows Based on Direct Numerical Simulations," *Int. J. Heat and Fluid Flow*, Vol. 18(4), pp. 347-359.
- Nakayama, A. and Vengadesan, S.N., 2002, "On the Influence of Numerical Schemes and Subgrid-Stress Models on Large Eddy Simulation of Turbulent Flow past a Square Cylinder," *Int. J. Numer. Meth. Fl.*, Vol. 38, pp. 227-253.
- Nelson, C.C. and Nichols, R.H., 2003, "Evaluation of Hybrid RANS/LES Turbulence Models Using an LES Code," AIAA-2003-3552.
- Nichols, R.H. and Nelson, C.C., 2003, "Application of Hybrid RANS/LES Turbulence Models," AIAA-2003-0083.
- Nishiyama, T., 1977, "Linearized Theory of Supercavitating Hydrofoils in Subsonic Liquid Flow," *J. Fluids Eng.*, Vol. 99(2), pp.311-318
- Oba, R., Ito, Y. and Miyakura, H., 1985, "Cavitation Observation in a Jet-Flow Gate-Valve," *JSME Int. J., Series B*, Vol. 28, pp. 1036-1043.
- Oliveira, P.J. and Issa, R.I., 2001, "An Improved PISO Algorithm for the Computation of Buoyancy-Driven Flows," *Numerical Heat Transfer Part B*, Vol. 40, pp. 473-493.
- Patankar, S.V., 1980, *Numerical Heat Transfer and Fluid Flow*, Hemisphere, Washington, D.C.
- Piomelli, U., 1999, "Large-eddy Simulation: Achievements and Challenges," *Progress in Aerospace Sciences*, Vol. 35(4), pp. 335-362.
- Rhie, C. and Chow, W., 1983, "Numerical Study of the Turbulent Flow Past an Isolated Airfoil with Trailing Edge Separation," *AIAA J.*, Vol. 21, pp. 1522-1532.

- Rodi, W., 1997, "Comparison of LES and RANS Calculations of the Flow around Bluff Bodies," J. Wind Eng. Ind. Aerodyn., Vol. 69-70, pp.55-75.
- Rogallo, R.S. and Moin, P., 1984, "Numerical Simulation of Turbulent Flows," Annual Review of Fluid Mechanics, Vol. 16, pp. 99-137.
- Roy, C.J., Dechaht, L.J., Payne, J.L. and Blottner, F.G., 2003, "Bluff-Body Flow Simulations Using Hybrid RANS/LES," AIAA 2003-3889.
- Ruggeri, R.S. and Moore, R.D, 1969, "Method for Prediction of Pump Cavitation Performance for Various Liquids, Liquid Temperatures and Rotation Speeds," NASA Technical Note, NASA TN D-5292.
- Saffman, P.G., 1970, "A Model for Inhomogeneous Turbulent Flow," Proc. Roy. Soc. Lond., Vol. A317, pp. 417-433.
- Sagaut, P., 2003, *Large Eddy Simulation for Incompressible Flows*, Springer: Berlin, Germany.
- Sandham, N.D., Alam, M. and Morin, S., 2001, "Embedded Direct Numerical Simulation for Aeronautical CFD," Aeronautical Journal, Vol. 105, pp. 193-198.
- Saurel, R. and Coochi, J.P., 1999, "Numerical Study of Cavitation in the Wake of a Hypervelocity Underwater Projectile," J. Propulsion and Power, Vol. 15(4), pp. 513-522.
- Saurel, R. and Lemetayer, O., 2001, "A Multiphase Model for Compressible Flows with Interfaces, Shocks, Detonation Waves and Cavitation," J. Fluid Mech., Vol. 431, pp.239-271.
- Schumann, U., 1975, "Subgrid Scale Models for Finite Difference Simulations of Turbulent Flows in Plane Channel and Annuli," J. Comput. Phys., Vol. 18, pp. 376-404.
- Senocak, I., 2002, *Computational Methodology for the Simulation of Turbulent Cavitating Flows*, Ph.D. Dissertation, University of Florida, Gainesville, USA.
- Senocak, I. and Shyy, W., 2002a, "A Pressure-Based Method for Turbulent Cavitating Flow Computations," J. Comp. Physics, Vol. 176, pp. 363-383.
- Senocak, I. and Shyy, W., 2002b, "Evaluation of Cavitation Models for Navier-Stokes Computations," Proc. of 2002 ASME Fluids Engineering Division Summer Meeting, Montreal, CA, FEDSM2002-31011.
- Senocak, I. and Shyy, W., 2003, "Computations of Unsteady Cavitation with a Pressure-based Method," 4th ASME_JSME Joint Fluids Eng. Conference, Honolulu, Hawaii, FEDSM2003-45009.

- Senocak, I., and Shyy, W., 2004a, "Interfacial Dynamics-Based Modeling of Turbulent Cavitating Flows, Part-1: Model Development and Steady-State Computations," *Int. J. Numer. Meth. Fl.*, Vol. 44, pp. 975-995.
- Senocak, I., and Shyy, W., 2004b, "Interfacial Dynamics-Based Modeling of Turbulent Cavitating Flows, Part-2: Time-Dependant Computations," *Int. J. Numer. Meth. Fl.*, Vol. 44, pp. 997-1016.
- Shyy, W., 1994, *Computational Modeling for Fluid Flow and Interfacial Transport*, Elsevier, Amsterdam, The Netherlands (Revised print 1997).
- Shyy, W., Thakur, S.S., Ouyang, H., Liu, J. and Blosch, E., 1997, *Computational Techniques for Complex Transport Phenomena*, Cambridge University Press, New York.
- Shyy, W., Wu, J., Utturkar Y. and Tai, C.F., 2004, "Interfacial dynamics-based model and multiphase flow computation," *Proceedings of the ECCOMAS 2004 Congress*, Jyväskylä, Finland.
- Singhal, A.K., Vaidya, N. and Leonard, A.D., 1997, "Multi-Dimensional Simulation of Cavitating Flows Using a PDF Model for Phase Change," *Proc. of 1997 ASME fluids Engineering Division Summer Meeting*, ASME paper FEDSM97-3272.
- Singhal, A.K., Li, H., Athavale, M.M. and Jiang, Y., 2002, "Mathematical Basis and Validation of the Full Cavitation Model," *J. Fluids Eng.*, Vol. 124(3), pp. 617-624.
- Smagorinsky, J., 1963, "General Circulation Experiments with the Primitive Equations. I: The Basic Experiment," *Mon. Weather Rev.*, Vol. 91, pp. 99-164.
- Smith, L.M. and Woodruff, S.L., 1998, "Renormalization-group Analyzes of Turbulence," *Annual Reviews of Fluid Mechanics*, Vol. 30, pp. 275-310.
- Sohankar, A., Norberg, C. and Davidson, L., 1999, "Numerical Simulation of Flow past a Square Cylinder," *ASME-JSME Fluid Engineering Division Summer Meeting*, Paper FEDSM99-7172.
- Spalart, P.R., Jou, W.-H., Strelets, M. and Allmaras, S.R., 1997, "Comments on the Feasibility of LES for Wings, and on a Hybrid RANS/LES Approach," *Proc. of 1st AFOSR Int. Conf. on DNS/LES*, Greyden Press, Columbus, OH.
- Stutz, B. and Reboud, J.L., 1997, "Experiments on Unsteady Cavitation," *Exp. Fluids*, Vol. 22, pp. 191-198.
- Stutz, B. and Reboud, J.L., 2000, "Measurements within Unsteady Cavitation," *Exp. Fluids*, Vol. 29, pp. 545-552.

- Tani, K., Ito, Y., Oba, R. and Iwasaki, M., 1991a, "Flow Visualization in the High Shear Flow on Cavitation Erosion around a Butterfly Valve, *Trans. JSME*, Vol. 57, pp. 1525-1529.
- Tani, K., Ito, Y., Oba, R., Yamada, M. and Onishi, Y., 1991b, "High-Speed Stereo-Flow Observations around a Butterfly Valve," *Mem. Inst. Fluid Sci., Tohoku Univ.*, Vol. 2, pp. 101-112.
- Thakur, S.S. and Wright, J., 2002, "An Operator-Splitting Algorithm for Unsteady Flows at All Speed in Complex Geometries, In Press.
- Thakur, S.S, Wright, J. and Shyy, W., 2004, *STREAM: A Computational Fluid Dynamics and Heat Transfer Navier-Stokes Solver. Theory and Applications*, Streamline Numerics, Inc., and Computational Thermo-Fluids Laboratory, Department of Mechanical and Aerospace Engineering Technical Report, Gainesville, Florida.
- Utturkar, Y., Thakur, S. and Shyy, W., 2005, "Computational Modeling of Thermodynamic Effects in Cryogenic Cavitation," AIAA-2005-1286.
- Vaidyanathan, R., Senocak I., Wu, J. and Shyy, W., 2003, "Sensitivity evaluation of a transport-based turbulent cavitation model," *J. Fluid Eng.*, Vol. 125, pp. 447-458.
- Venkateswaran, S., Lindau, J.W., Kunz, R.F. and Merkle, C.L., 2002, "Computation of Multiphase Mixture Flows with Compressibility Effects," *J. Comp. Physics*, Vol. 180(1), pp. 54-77.
- Wallis, G.B., 1969, *One-dimensional Two-Phase Flow*, McGraw Hill, New York City, NY.
- Wang, G., 1999, *A Study on Safety Assessment of a Hollow-Jet Valve Accompanied with Cavitation*, PhD Dissertation, Tohoku University, Sendai, Japan.
- Wang, G., Senocak, I., Shyy, W., Ikohagi, T. and Cao, S., 2001, "Dynamics of Attached Turbulent Cavitating Flows," *Progress in Aerospace Sciences*, Vol. 37, pp. 551-581.
- Wilcox, D.C., 1998, *Turbulence Modeling for CFD*, DCW Industries, INC., La Canada, CA.
- Wu J., Utturkar Y., Senocak I., Shyy W. and Arakere N., 2003a, "Impact of turbulence and compressibility modeling on three-dimensional cavitating flow computations," AIAA-2003-4264.
- Wu, J., Utturkar, Y. and Shyy, W., 2003b, "Assessment of Modeling Strategies for Cavitating Flow around a Hydrofoil," 5th Int. Symposium on Cavitation, Osaka, Japan, Cav03-OS-1-12.

- Yoshizawa, A., 1993, "Bridging between Eddy-Viscosity-Type and Second-Order Models Using a Two-Scale DIA," 9th Int. Symp. on Turbulent Shear Flow, Vol.3, pp.23.1.1-23.1.6.
- Yu, B., Tao, W., Wei, J. Kawaguchi, Y., Tagawa, T. and Ozoe, H., 2002, "Discussion on Momentum Interpolation Method for Collocated Grids of Incompressible Flow," Numerical Heat Transfer part B, Vol. 42, pp. 141-166.
- Yu, D. and Kareem, A., 1997, "Numerical Simulation of Flow around Rectangular Prisms," J. Wind Eng. Ind. Aerodyn., Vol. 67-68, pp. 195-208.

BIOGRAPHICAL SKETCH

Jiongyang Wu was born in a small village in Jieyang county, Guangdong province, P.R. China. He received both his B.S. and M.S. degrees from the Hydraulic Engineering Department at Tsinghua University, in 1997 and 2000, respectively. In August 2000, he joined the Computational Thermo-Fluids group at the Department of Mechanical and Aerospace Engineering, University of Florida for his Ph.D study. His research interests include turbulence and cavitation modeling, multi-phase flows, fluid machinery flows.

Jiongyang met his wife, Weishu Bu, during his study in University of Florida. They married in March 2003. And then their son, Andy Wu, was born and became a new family member.